東海大学大学院　令和5年度 博士論文

Earthquake–Tsunami Multihazard Analysis Considering Foundation Uplift of Structure

（構造物基礎の浮き上がりを考慮した

地震と津波の複合災害の解析）

指 導　三神　厚　教 授

東海大学 大学院 総合理工学研究科

総合理工学専攻

Thanisorn Srikulruangroj

Earthquake–Tsunami Multihazard Analysis Considering Foundation Uplift of Structure

Thanisorn Srikulruangroj

ABSTRACT

Structures in coastal areas may suffer multiple damage due to massive tsunamis generated by largely intensive earthquakes, such as the 2004 Sumatra-Andaman Earthquake and the 2011 Great East Japan Earthquake. Thus, it is imperative to establish an evaluation methodology that comprehensively addresses the impact of complex earthquake–tsunami disasters. Few studies on earthquake–tsunami multihazard scenarios have adequately considered soil-structure interaction, especially nonlinear aspects such as foundation uplift. This phenomenon has influence to structural response and may be directly linked to the loss of human life. For example, numerous buildings were overturned and washed away due to the complex disaster resulting from the earthquake and following tsunami in 2011. Consequently, this study aims to enhance the earthquake-tsunami interaction diagram that Carey et al. (2019) proposed by incorporating foundation uplift. However, before generating the diagrams, the effect of seismic isolation due to foundation uplift on building structures during earthquake ground motion is also investigated to understand the physical foundation uplift behavior.

This dissertation starts with discussing a comparison of two numerical models considering foundation uplift in Chapter 2. The primary objective of this chapter is not to devalue the assumptions of each model. The comparison aims to discuss the impact of soil nonlinearity or geometrical nonlinearity on foundation uplift behavior, particularly emphasizing scenarios with a low ground contact ratio. Low-rise and medium-rise buildings with shallow foundations on stiff soil are prepared. Five different frequency characteristic ground motions are employed for thorough time history analysis. The computational results underscore the similarity in structural responses between the two numerical models for structures situated on stiff soil and rock, even in cases where there is a notable difference in the ground contact ratio for both models. This similarity is particularly evident when the ground contact ratio is less than 40%. Additionally, the observations reveal that plastic deformation of the soil may reduce the degree of foundation uplift. Moreover, the comparison results present that the level of uplifting of the foundation will depend on various different factors, such as structural characteristics, seismic input motions, and soil conditions.

Subsequently, the effects of seismic isolation due to foundation uplift are investigated in Chapter 3 by considering three scenarios: a fixed base case, a case with foundation considering linear soil-structure interaction (SSI), and a case considering nonlinear SSI accompanied by foundation uplift. Chapter 3 attempts to discuss the effects of seismic isolation due to foundation uplift, considering both structure nonlinearity and soil nonlinearity by using

the energy concept. For this purpose, taking up low-rise and medium-rise buildings with shallow foundations on stiff soil as analytical models and fifteen ground motions recorded during major earthquakes are applied by varying their magnitude to discuss the impact of intensity of the seismic motions. The computation results demonstrate that foundation uplift has advantageous effects on the structural response. Foundation uplift works for cutting off seismic motion, consequently leading to reduced structural acceleration responses. Furthermore, foundation uplift may reduce the formation of a hysteretic loop or the accumulation of nonlinear deformation in the superstructure. However, in some scenarios where the structure is subjected to high-intensity and low-frequency ground motion, foundation uplift may have an adverse impact on structural responses. Excessive foundation uplift can render the structure unstable, which has to avoid.

In Chapter 4, earthquake–tsunami interaction diagrams considering foundation uplift are generated. Additionally, this chapter also simultaneously considers two different limit states: structural damage (inter-layer drift deformation angle) and foundation uplift (ground contact ratio). This simultaneous consideration was necessary, as determining whether the building or the foundation reaches a critical state first depends on the characteristics of ground motions. To generate the earthquake–tsunami interaction diagram considering foundation uplift, a three-story building with a mat foundation on stiff soil is prepared. Thirty recorded ground motions in the coastal area of Japan during the 2011 Tohoku earthquake and the hydrodynamic force are applied as earthquake loading and tsunami loading, respectively. In addition to generating the diagrams considering the two different limit states simultaneously, six ground motions with diverse frequency characteristics are selected. The earthquake–tsunami interaction diagrams illustrate that the damage resulting from the earthquake could reduce the required intensity of the tsunami via the hydrodynamic force (F_D) to reach the corresponding limit states. It can be concluded that the resistance of the structure to a subsequent tsunami can be reduced due to the residual effects or damage caused by earthquakes. Furthermore, the diagrams also show the dependence of the dominant limit state on the characteristics of the input ground motion.

Finally, the authors believe that this study is necessary and useful to determine and prevent the human damage caused by the complex disaster of earthquake and tsunami and this dissertation will provide valuable information for the effective reinforcement of buildings against not only earthquakes or tsunamis but also earthquake–tsunamis multihazard in the future.

TABLE OF CONTENTS

LIST OF TABLES

LIST OF FIGURES

LIST OF PUBLICATIONS

This dissertation is based on the following publications:

1. Srikulruangroj, T., and Mikami, A. : Effect of soil improvement on the dynamic behavior of structure supported by shallow foundation, *The 14th National Symposium on Ground Improvement*, 2020.

2. Srikulruangroj, T., and Mikami, A. : Earthquake–tsunami interaction diagram considering foundation uplift, *Journal of Japan Society of Civil Engineers, Ser. A1 (Structural Engineering & Earthquake Engineering (SE/EE))*, Vol. 78, 2022.

3. Srikulruangroj, T., and Mikami, A. : Earthquake–tsunami interaction diagram considering two different limit state, *Journal of Japan Society of Civil Engineers, Special Issue (Ocean Engineering)*, Vol. 11, No. 2, 2023.

1. INTRODUCTION

In this opening chapter, Section 1.1 presents the study background, Section 1.2 reviews the research on multihazard problems; Section 1.3 provides an overview of foundation uplift; Section 1.4 describes the purpose of this work; and Section 1.5 presents the organization of this thesis.

1.1 Background

The extensive tsunami generated by the Great East Japan Earthquake damaged the east coastal areas of Japan on March 11, 2011 [1]. Many buildings suffered severe damage, with some structures overturned by the 2011 Tohoku Earthquake and Tsunami events [2,3]. Previous studies investigated factors that caused buildings to overturn. Yeh et al. [4] presented that buildings are overturned because of hydrodynamic and buoyancy forces and soil instability. Latcharote et al. [5] suggested that the buoyancy force has a greater effect on building overturning than the hydrodynamic force. Nevertheless, the decisive factors leading to an overturned building must be investigated. Mimura et al. [6] and Gokon and Koshimura [7] stated that the coastal areas of Japan affected by the 2011 Great East Japan Earthquake and Tsunami events suffered from multiple damages due to sequential earthquake and tsunami hazards. The damages were accumulated due to the successively occurring major earthquakes, which included the 2016 Kumamoto Earthquake [8]. Extremely large earthquakes generate giant tsunamis that cause considerable damage to coastal structures; hence, an evaluation method for describing the effects of an earthquake–tsunami combined disaster is necessary.

1.2 Literature Review

Studies on multihazard problems have gained significant attention in recent years. Ishibashi et al. [9] developed a probabilistic approach for assessing the reliability of structures under continuous earthquake and tsunami hazards while accounting for various uncertainty sources. Their methodology offers a comprehensive framework for evaluating the structural responses to these hazards and can be used to inform decision-making regarding risk mitigation and management. Goda et al. [10] presented a new multihazard catastrophe model for coastal area buildings that can produce beneficial information for more advanced analysis in earthquake–tsunami engineering. Their results indicated that the contribution of a tsunami to the total multihazard losses associated with an earthquake substantially increases with the earthquake magnitude. Carey et al. [11] suggested a framework for demonstrating the effects

of a earthquake–tsunami event on the soil–foundation–bridge system. Meanwhile, Scott and Mason [12] developed constant-ductility response spectra to consider the hydrodynamic tsunami loads following the seismic loads, leading to the strength demand estimation. They concluded that the amplification response considering the sequential earthquake and tsunami loading over considering only one earthquake case is crucial for structures with long natural periods and a high ductility capacity. In a subsequent work, Carey et al. [13] suggested a diagram illustrating the effects of an earthquake and a tsunami on a bridge structure and found that the impact of an earthquake on a structure decreases its ability to resist subsequent tsunamis. An earthquake–tsunami interaction diagram is highly beneficent because the diagrams can indicate the residual effects of the earthquake loading impact on the reduction strength of the structure to resist subsequent tsunami loading [13]. Although some studies on the earthquake–tsunami multihazard considered the effect of the soil–structure interaction, most studies did not consider the nonlinear soil–structure interaction with the foundation uplift, which has significant positive and negative effects on structural responses [14]. As described above, many buildings fell and were washed away due to the multihazard caused by the Tohoku Earthquake and the subsequent tsunami events in 2011. Therefore, any study on the responses of the soil–structure interaction systems should consider the effect of the foundation uplift phenomenon.

The foundation uplift is not recommended in current seismic designs, and most conventional seismic design standards [15] assume that a structure's foundation is fixed at the base. However, a structure supported by a shallow foundation may be separated from the soil when subjected to a relatively strong earthquake ground motion, as illustrated in Figure 1.1. This phenomenon is known as the foundation uplift, which is classified as a nonlinear soil–

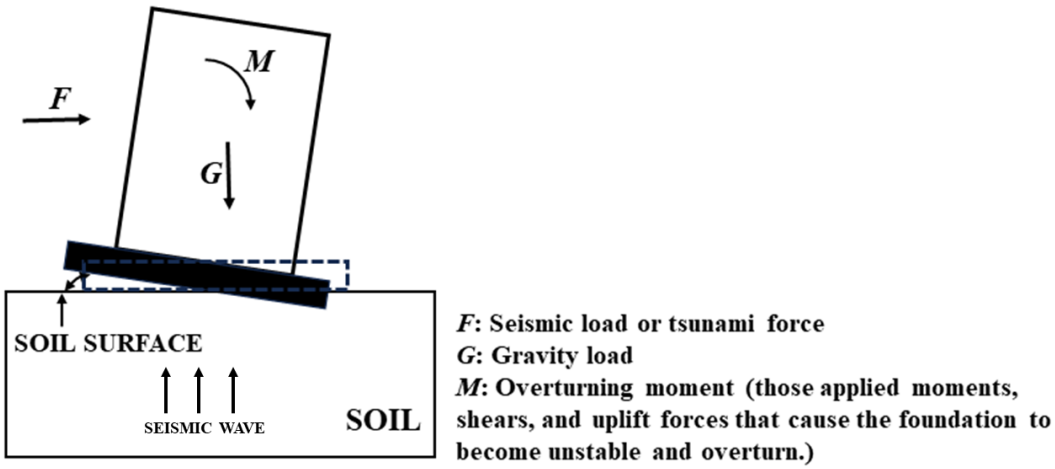

Figure 1.1 Illustration of the foundation uplift

structure interaction. Numerous examples of the foundation uplift can be observed in many earthquake events. For example, several tall and slender petroleum cracking towers experienced stretched anchor bolts and swayed back and forth on their foundations during the 1952 Arvin–Tehachapi Earthquake in California [16]. Hanson [17] reported that ice was discovered under some oil tanks after the March 1964 Alaska Earthquake, indicating that uplift occurred during the event. The foundation uplift occurred in Veterans Hospital Building 41 during the San Fernando Earthquake [18] and in high-rise buildings during the 1995 Kobe Earthquake [19]. Sometimes, the foundation uplift becomes excessive, such as some buildings overturned by the 2011 Tohoku earthquake and tsunami were found [5], as shown in Figure 1.2. It is generally considered as an unstable phenomenon; hence, the behavior of structures must be studied beyond design to ensure safety during extreme events, such as earthquakes and other natural disasters. Considering the long-term effects of the foundation uplift on the structural integrity of a building is also essential because the repeated cycles of uplift and settlement can lead to significant damage over time.

Numerous studies examined structural responses considering the foundation uplift. In fact, the phenomenon was studied in the early 1960s by Housner [16]. His research was inspired by the observation that some elevated water tanks with a peculiar design comprising 11 golf-ball-on-a-tee-shaped structures survived the ground motion during the 1960 Chilean earthquakes, whereas other seemingly more stable reinforced concrete elevated water tanks were severely damaged. To understand this phenomenon, he conducted an analysis and derived an equation expressing the period of a rocking block as a function of its amplitude. He also

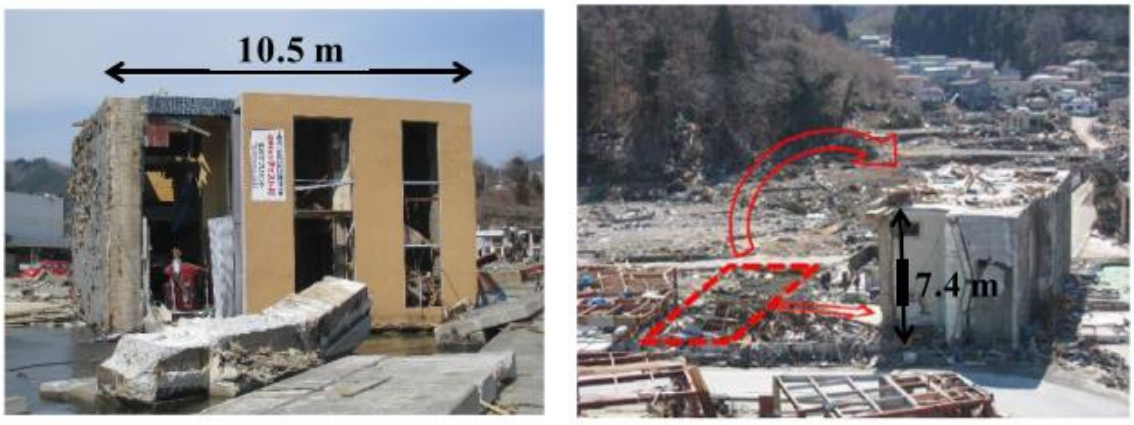

(a) A three-story overturned building (b) A two-story overturned building

Figure 1.2 Photo of example overturned buildings owing to the 2011 Tohoku Earthquake and Tsunami in the town of Onagawa (referred to Latcharote et al. [5]). Note that the photos were taken by the survey team of International Research Institute of Disaster Science, Tohoku University [5]

developed a formula for estimating the energy dissipation that occurs during the rocking motion. His results formed the basis of FEMA-356 [20]. Yim and Chopra [21] studied a single degree-of-freedom (SDOF) system supported on a rigid foundation, prevented and permitted the uplift, and concluded that the foundation uplift reduced the base shear of the structure. Hayashi [20], Hayashi and Takahashi [22], and Hayashi et al. [23] investigated the building structure damage during the 1995 Hyogo-ken Nanbu Earthquake using joint elements with a two-dimensional (2D) finite element method. Consequently, the uplifting effect may be the reason why slender buildings did not suffer from any structural damage during the 1995 Hyogo-ken Nanbu Earthquake. The reduction effect caused by the basemat uplift, however, may have been dependent on the ground motion intensity and the structure strength. Apostolou et al. [24] analyzed how slender structures respond to overturning and rocking considering the possibility of the foundation uplift. They found that the size and the slenderness of the structure affect the overturning response. Gazetas and Apostolou [25] studied the effect of the foundation uplift and soil yielding by modeling a rigid block sustained on soil. They found that the foundation uplift has a beneficial effect on the superstructure, provided that certain conditions related to the dynamic characteristics of both the structure and the ground motion are met. Iwashita and Taniguchi [26] investigated the effect of uplift on earthquake response by using a model of a one-span, 11-story frame and a frame with a shear wall. They concluded that the foundation uplift reduces the base shear of structures. Asari et al. [27] investigated the reduction effect of the foundation uplift on a building structure from the energy response perspective by treating an analytical model as an equivalent single-degree-of-freedom system. Similarly, Inoue and Mikami [28-30] discussed the reduction effect of the foundation uplift on a bridge structure using the energy concept by using the macroelement model proposed by Nakatani et al. [31]. They found that the effect of the foundation uplift leads to a significant input energy reduction to structures and strain energy. They [27-30] also assumed the linear behavior of structures. On the contrary, some other studies demonstrated that the foundation uplift can affect the nonlinear behavior of structures. Khoshnoudian and Hashemi [32] examined the nonlinear behavior of a 2D frame under the foundation uplift effect using a bilinear model to account for the structural nonlinearities. They found that the foundation uplift leads to the axial force decrease. Qin et al. [33] investigated the foundation uplift effect and the plastic behavior of both the structure and the soil on the structural response by performing shake table simulations. Their results indicated that the foundation uplift can reduce the plastic hinge development. Pecker and Chatzigogos [34] studied the effect of foundation compliance on the structural responses of a bridge structure and concluded that the nonlinear soil–structure interaction (SSI) has a positive

impact on the reduction of the superstructure's ductility demand. Sarrafzadeh et al. [35] performed ‘shake table tests’ to investigate the reduction effect of the foundation uplift on induced energies. Their results demonstrated that the kinetic and damping energies of the structure were reduced by the effects of the foundation uplift and soil nonlinearity. Ghannad and Jafarie [36] modeled an equivalent bilinear SDOF model on a rigid foundation sustained on a spring–damper soil element to examine the effect of the foundation uplift. They concluded that the ductility demand decreased due to the foundation uplift, whereas the displacement ratios increased for both linear and nonlinear structures. Dolatshahi et al. [37] obtained a similar conclusion by investigating the effect of material deterioration, p-delta, and foundation uplift on the response of SSI systems.

1.3 Study Objective

Few studies on earthquake–tsunami multihazard were conducted by considering the soil–structure interaction, especially the foundation uplift. The present study aims to further develop the earthquake–tsunami interaction diagrams proposed by Carey et al. [13] by considering the foundation uplift. Their proposed diagrams [13] are essentially useful because they can illustrate that the residual effects of earthquake loading significantly affect the reduction strength of a structure to withstand subsequent tsunami loading. The effect of the nonlinear soil–structure interaction considering the foundation uplift cannot be neglected in earthquake engineering. However, before generating earthquake–tsunami interaction diagrams considering the foundation uplift, the foundation uplift behavior must first be investigated, and the foundation uplift effect must be discussed because the foundation uplift effects must repeatedly be considered to ensure an accurate estimation of the structural response and the damage potential during seismic motion.

This work attempts to further discuss the effect of the foundation uplift on building structures and extend the study on earthquake–tsunami multihazard considering the foundation uplift as follows:

(1) The seismic isolation effect caused by the foundation uplift is discussed from the structural response and energy flow perspective.

(2) Earthquake–tsunami interaction diagrams are further developed by considering the foundation uplift.

(3) Earthquake–tsunami interaction diagrams are further improved by simultaneously considering the foundation uplift and the inter-layer deformation.

1.4 Study Organization

This article comprises five chapters outlined below.

Chapter 1: This chapter describes the foundation uplift overview, reviews research on the foundation uplift, and presents the objectives and organization of this research.

Chapter 2: This chapter briefly describes the fundamentals of the soil–structure interaction and the foundation uplift behavior, introduces two numerical models for calculating the structural responses considering the foundation uplift, including mass, stiffness, damping, and soil–foundation properties, presents the analytical models and recorded ground motions used in this work, and compares and discusses the seismic responses considering the foundation uplift of a linear structure system on a mat foundation based on two different numerical models.

Chapter 3: This chapter further discusses the seismic responses considering the foundation uplift with a nonlinear structure system and considering that the structure system assumption in Chapter 2 is based on a linear behavior. This chapter also briefly describes the trilinear model following Masing's rule considering the nonlinear stiffness characteristics and discusses the effect of the foundation uplift from the structural response and energy perspective considering that when the foundation is separated from the soil, the energy from the soil transmitted to the structure will not be high.

Chapter 4: After understanding the physics of the foundation uplift problem through the discussions in Chapters 2 and 3, Chapter 4 generates and discusses the earthquake–tsunami interaction diagrams considering the foundation uplift. The 2011 Tohoku Earthquake and Tsunami events overturned buildings, and some publications reported on the multiplicative damage in the coastal areas negatively affected by the sequential 2011 earthquake and tsunami. The authors believe this chapter will be vital in determining severe damages, such as overturned buildings, that may have been caused by the complex earthquake and tsunami disasters.

Chapter 5: This chapter provides a summary of the results obtained in Chapters 2 to 4.

References

[1] Kazama, M. and Noda, T.: Damage statistics (Summary of the 2011 off the Pacific coast of Tohoku earthquake damage), *Soils and Foundations*, 52, 5, 780-792, 2012.

[2] Nishiyama, I., Okawa, I., Fukuyama, H. and Okuda, Y.: Building damage by the 2011 off the Pacific coast of Tohoku earthquake and coping activities by NILIM and BRI collaborated with the administration, UJNR, 2011.

[3] Suppasri, A., Shuto, N., Imamura, F., Koshimura, S., Mas, E. and Yalciner, A. C.: Lessons learned from the 2011 Great East Japan tsunami: performance of tsunami countermeasures, coastal buildings, and tsunami evacuation in Japan, *Pure and Applied Geophysics*, 170, 993-1018, 2013.

[4] Yeh, H., Sato, S. and Tajima, Y.: The 11 March 2011 East Japan earthquake and tsunami: tsunami effects on coastal infrastructure and buildings, *Pure and Applied Geophysics*, 170, 1019-1031, 2013.

[5] Latcharote, P., Suppasri, A., Yamashita, A., Adriano, B., Koshimura, S., Kai, Y. and Imamura, F.: Possible failure mechanism of buildings overturned during the 2011 great east Japan tsunami in the town of Onagawa, *Frontiers in Built Environment. Earthquake Engineering*, 3, 2017.

[6] Mimura, N., Yasuhara, K., Kawagoe, S., Yokoki, H. and Kazama, S.: Damage from the great east Japan earthquake and tsunami — a quick report, *Mitigation and Adaptation Strategies for Global Change*, 16, 803-818, 2011.

[7] Gokon, H. and Koshimura, S.: Mapping of building damage of the 2011 Tohoku earthquake tsunami in Miyagi Prefecture, *Coastal Engineering Journal*, 54, 1, 1250006-1250001, 2012.

[8] Goda, K., Campbell, G., Hulme, L., Ismael, B., Ke, L., Marsh, R., Sammonds, P., So, E., Okumura, Y., Kishi, N., Koyama, M., Yotsui, S., Kiyono, J., Wu, S. and Wilkinson, S.: The 2016 Kumamoto earthquake: cascading geological hazards and compounding risks, *Frontiers in Built Environment. Earthquake Engineering*, 2, 2016.

[9] Ishibashi, H., Kojima, T., Akiyama M. and Koshimura S.: Proposal of reliability evaluation method for bridge and embankment structures considering continuity of strong ground motions and tsunami hazard and case study assuming Nankai trough earthquake, *Proceeding of JSCE A1 (Structural and Earthquake Engineering)*, 76, 1, 41-60, 2020. (in Japanese)

[10] Goda, K., De RiSi, R., De Luca, F., Muhammad, A., Yasuda, T. and Mori, N.: Multi-hazard earthquake tsunami loss estimation of Kuroshio Town, Kochi Prefecture, Japan considering the Nankai-Tonankai megathrust, *International Journal of Disaster Risk Reduction*,

54, 102050, 2021.
[11] Carey, T., Mason, H. B., Barbosa, A. R. and Scott, M. H.: Modeling framework for soil-bridge system response during sequential earthquake and tsunami loading, *Proceedings of the 10th National Conference in Earthquake Engineering*, 2014.
[12] Scott, M. H. and Mason, H. B.: Constant-ductility response spectra for sequential earthquake and tsunami loading, *Earthquake Engineering and Structure Dynamics*, 46, 1549-1554, 2017.
[13] Carey, T. J., Mason, H. B., Barbosa, A. R. and Scott, M. H.: Multihazard earthquake and tsunami effects on soil-foundation-bridge systems, *Journal of Bridge Engineering*, 24, 4, 2019.
[14] Oliveto, G., Caliò, I. and Greco, A.: A large displacement behaviour of a structural model with foundation uplift under impulsive and earthquake excitations, *Earthquake Engineering and Structural Dynamics*, 32, 369-393, 2003.
[15] American Society of Civil Engineers: Minimum design loads and associated criteria for buildings and other structures, *ASCE/SEI 7-16*, 2016.
[16] Housner, G. W.: The behavior of inverted pendulum structures during earthquakes, *Bulletin of the Seismological Society of America*, 53, 2, 403-417, 1963.
[17] Hanson, R. D.: Behavior of liquid-storage tanks, *The Great Alaska Earthquake of 1964, Engineering*, National Academy of Sciences, Washington, D.C., p. 334, 1973.
[18] Rutenberg, A., Jennings, P. C. and Housner, G. W.: The response of veterans hospital building 41 in the San Fernando earthquake, *Report No. EERL 80-03*, Earthquake Engineering Research Laboratory, California Institute of Technology, Pasadena, California, May 1980.
[19] Hayashi, Y.: Damage reduction effect due to basemat uplift of buildings, *Journal of Structural and Construction Engineering*, 485, 53-62, 1996. (in Japanese)
[20] FEMA: *Pre-standard and Commentary for The Seismic Rehabilitation of Buildings*, FEMA-356, Washington, D.C., 2000.
[21] Yim, C. and Chopra, A. K.: Earthquake response of structures with partial uplift on Winkler foundation, *Earthquake Engineering and Structural Dynamics*, 12, 263-281, 1984.
[22] Hayashi, Y. and Takahashi, I.: Soil-structure interaction effects on building response in recent earthquake, *Proceedings of the 3rd UJNR Workshop on Soil–Structure Interaction*, Menlo Park, California, 2004.
[23] Hayashi, Y., Tamura, K., Mori, M. and Takahashi, I.: Simulation analyses of buildings damaged in the 1995 Kobe, Japan earthquake considering soil-structure interaction, *Earthquake Engineering and Structural Dynamics*, 28, 371–391, 1999.
[24] Apostolou, M., Gazetas and G., Garini, E.: Seismic response of slender rigid structures

with foundation uplifting, *Soil Dynamics and Earthquake Engineering*, 27, 642–654, 2007.
[25] Gazetas, G. and Apostolou, M.: Nonlinear soil–structure interaction: foundation uplifting and soil yielding, *Proceedings of the 3rd UJNR Workshop on Soil–Structure Interaction*, Menlo Park, California, 2004.
[26] Iwashita, K. and Taniguchi, H.: Effect of uplift on earthquake response of building, *Proceedings of the 12th World Conference on Earthquake Engineering (WCEE)*, 1328, 2000.
[27] Asari, T., Fujita, Y. and Midorikawa, M.: Energy response of building structures with foundation uplift subjected to earthquake motions, *Proceedings of the 14th World Conference on Earthquake Engineering (WCEE)*, 2008.
[28] Inoue, T. and Mikami, A.: Investigation of stress reduction effect on structures due to basemat uplift using energy concept, *International Journal of GEOMATE*, 6, 749-756, 2014.
[29] Inoue, T. and Mikami, A.: Investigation of stress reduction effect of bridge pier due to non-linear dynamic interaction using energy concept, *Proceeding of JSCE A1 (Structural and Earthquake Engineering)*, 76, 41-60, 2014. (in Japanese)
[30] Inoue, T. and Mikami, A.: Study on stress reduction effect of bridge pier due to basemat uplift and soil yielding, *Japanese Geotechnical Journal*, 10, 1-16, 2014. (in Japanese)
[31] Nakatani S., Shirato, M. and Kouno, T.: Development of a numerical analysis model to predict seismic behavior of shallow foundations, *Public Works Research Institute Report*, ISSN 0386-5878, No.4101, 2008. (in Japanese)
[32] Khoshnoudian, F. and Hashemi, M.A.: Nonlinear behavior of building with foundation uplift under earthquake excitations, *Proceedings of the 13th World Conference on Earthquake Engineering (WCEE)*, 2004.
[33] Qin, X., Chen, Y. and Chouw, N.: Effect of uplift and soil nonlinearity on plastic hinge development and induced vibrations in structures, *Advances in Structural Engineering*, 16, 135-147, 2013.
[34] Pecker, A. and Chatzigogos, C. T.: Nonlinear soil structure interaction: impact on the seismic response of structures, *Earthquake Engineering in Europe, Geotechnical, Geological, and Earthquake Engineering*, 17:79-103, 2010.
[35] Sarrafzadeh, E., Lim, E., Qin, X. and Chouw, N.: Effect of plastic hinge, soil nonlinearity and uplift on earthquake energy in structure, *Proceedings of the 2014 New Zealand Society for Earthquake Engineering (NZSEE) Conference*, 2014.
[36] Ghannad, M. A. and Jafarieh, A. H.: Inelastic displacement ratios for soil–structure systems allowed to uplift, *Earthquake Engineering and Structural Dynamics*, 43, 1401-1421, 2014.

[37] Dolatshahi, KM., Vafaei, A., Kildashti, K. and Hamidia, M.: Displacement ratios for structures with material degradation and foundation uplift, *Bulletin of Earthquake Engineering*, 17, 5133-5157, 2019.

2. SEISMIC RESPONSE OF LINEAR STRUCTURE SYSTEMS CONSIDERING FOUNDATION UPLIFT

As mentioned in Chapter 1, the authors attempt to investigate the foundation uplift behavior and discuss the foundation uplift effect before generating the earthquake–tsunami interaction diagrams considering the foundation uplift. Chapter 2 opens with the study's background and purpose in Section 2.1. Section 2.2 then presents a brief explanation of the soil–structure interaction. Section 2.3 describes the foundation uplift behavior and two numerical models for calculating the seismic responses considering the foundation uplift, which are the macroelement and the SR model considering foundation uplift by referring to Nakatani et al. [1] and Tanaka et al. [2], respectively. Section 2.4 clarifies the numerical evaluation method, including the mass, stiffness, damping, and soil–foundation properties. Sections 2.5 and 2.6 explain the analytical models and the recorded ground motion used in this study, respectively. Section 2.7 discusses the foundation uplift phenomenon by comparing the structural responses considering the foundation uplift of the two numerical models. Finally, Section 2.8 summarizes this chapter.

2.1 Background and Purpose

A structure on a shallow foundation subjected to a relatively intensive seismic motion may be separated from the soil. This phenomenon is called the foundation uplift, which is categorized as a nonlinear soil–structure interaction. The foundation uplift significantly affects structural responses [3], even though structures are subjected to a weak or medium ground motion [4]. Accordingly, the foundation uplift behavior must be considered to ensure structural safety during earthquakes. Many numerical models calculate seismic responses considering the foundation uplift. For example, Hayashi [5] modeled the foundation and the soil using joint elements with a two-dimensional finite element method. This analysis type considers numerous degrees of freedom and requires a prolonged calculation time. Hence, to avoid a considerable amount of simulation work, some studies proposed simplified models for calculating the seismic response considering the foundation uplift. For example, Tanaka et al. [2] and Momma et al. [6] developed the SR model considering foundation uplift. According to Tanaka et al. [2] and Momma et al. [6], the SR model considering foundation uplift was called the horizontal-vertical interactive SR model; hence, hereinafter referred to as the horizontal–vertical interactive SR model in this study. Nakamura et al. [7] compared structural responses considering the foundation uplift by the model proposed by Tanaka et al. [2] and Momma et

al. [6] with the finite-element model and Green's function method. Their results presented that the horizontal maximum acceleration responses had almost the same values. The ground contact ratio of the SR models was comparatively different from the finite-element model and Green's function method. Nakamura et al. [7] compared and discussed the structural responses and ground contact ratios by considering that the structure was founded on comparatively hard soil (shear wave velocities (V_s): 1000 and 2000 m/s), of which nonlinearity may not need consideration. Some studies investigated and discussed the effect of soil nonlinearity and foundation uplift on the structural response. For example, Qin et al. [8] conducted shake table simulations to examine the foundation uplift effects and the nonlinear behavior of the structure and the soil on the structure response. They found that soil nonlinearity reduces both the structural response and the vertical displacement of the foundation. Inoue and Mikami [9,10] also studied the effects of the foundation uplift and the soil nonlinearity on the reduction effects of the section force by using the macroelement model of Nakatani et al. [1]. Their results illustrated that the section force was notably reduced by the foundation uplift and soil nonlinearity. The present study also investigates seismic responses considering the foundation uplift by comparing the horizontal–vertical interaction SR and macroelement models proposed by Nakatani et al. [1], which enabled the consideration of soil nonlinearity based on the plastic theory and the foundation uplift.

Note that this chapter aims not to evaluate or devalue the rules or assumptions of the models considering the foundation uplift, but to rather discuss the effect of soil nonlinearity or geometrical nonlinearity on the foundation uplift behavior, especially in the case of a low ground contact ratio. For this purpose, low- and medium-rise buildings with shallow foundations on stiff soil considering the foundation are prepared. The seismic response is calculated, and various results are discussed by performing five ground motions with different frequency characteristics recorded from major earthquakes for the time history analysis. This chapter considers structure based on the linear assumption.

2.2 Basic Soil–Structure Interaction

Ground motions unaffected by the presence of structures are referred to as free-field motions. A structure sustained on a solid rock is commonly considered as a fixed-base structure when subjected to an earthquake due to the high rock stiffness that constrains the rock motion very close to the free-field motion during the earthquake. Rock-sustained structures are known as fixed-base structures generally described in a Structural Dynamics textbook [11]. In contrast, if a heavy structure is supported on soft soil, the mass or stiffness of that structure differs from

that of the soil, making the ground and structure motions different. The soil response influences the structure motion and vice versa. This is referred to as the soil–structure interaction. The SSI effect can be neglected when light structures are founded on comparatively stiff soil or a rock. In contrast, it is significantly notable for heavy structures resting on soft soils.

2.2.1 Two basic components of the soil–structure interaction

The extent of soil–structure interaction will depend not only on the soil stiffness but also on the mass and stiffness of the structure. The soil–structure interaction is influenced by two phenomena: kinematic and inertial interactions.

2.2.1.1 Kinematic interaction

In the free-field motion, an earthquake motion results in soil deformations. By contrast, if a foundation is sustained on stiff soil, its inability will not match the free-field motion, consequently deviating the motion of the structure base from the free-field motion. The motion becomes result of the kinematic interaction. The deformation mode (e.g., torsion and rocking motion) can be induced by the kinematic interaction, which is not present in the free-field motion.

2.2.1.2 Inertial interaction

A structure subjected to a seismic motion generates inertia force by the structure mass. The inertia force transmitted to the surrounding soil will then produce foundation movement, which does not occur if structure is based on the fixed-base assumption. The dynamic responses of the structure–foundation system, which cause soil deformation, are called the inertial interaction. The amount of inertial interaction depends on the difference in stiffness between the structure and soil. Therefore, the influence of the inertial interaction significantly increases when a heavy structure is founded on soft soil.

2.2.2 Analytical methods considering the soil–structure interaction

The methods for analyzing the SSI effect on the seismic response are primarily categorized as direct or substructure methods.

2.2.2.1 Direct method

The structure and the soil are considered within a complete system, as shown in Figure 2.1. Finite element or finite differential methods are mostly employed in this approach. The direct method, however, requires considerable calculation time.

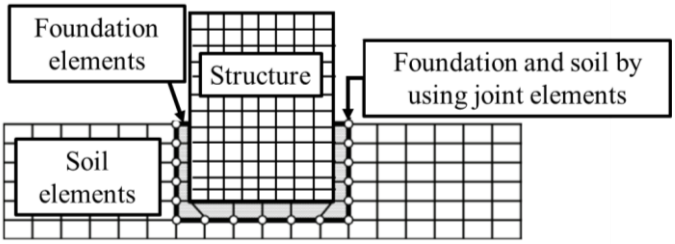

Figure 2.1 Illustration of a direct method for soil–structure interaction

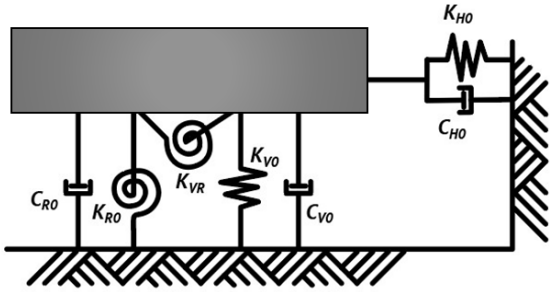

Figure 2.2 Illustration of a substructure method for soil–structure interaction

2.2.2.2 Substructure method

The substructure method considers the soil and the structure as a separate structural system. The soil and foundation are treated as a rigid foundation supported by springs and a dashpot, as illustrated in Figure 2.2. The stiffness and damping characteristics of the soil–foundation system are represented by the springs and the dashpot, respectively.

The soil and foundation nonlinearity should be considered while considering foundation compliance. This results in a non-conservative oversimplification, mainly in strong geometric nonlinearities. The structure and soil can be modeled as linear systems, but nonlinear behavior, such as sliding and foundation uplifting in the soil–structure system, is observed at the contact surface, which must be considered.

2.3 Foundation Uplift Behavior

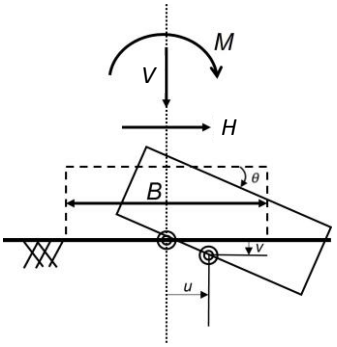

Figure 2.3 Foundation uplift behavior

Figure 2.3 depicts the foundation behavior, where H, V, and M are the horizontal and vertical forces and the overturning moment at the foundation center, respectively. The displacement response in the horizontal, vertical, and rotational directions at the base center of the foundation is denoted by u, v, and θ, respectively. B denotes the foundation width. The foundation uplift can easily occur when a structure is subjected to a strong earthquake. This results in the contact area reduction between the foundation and the soil, which can lead to a nonlinear relationship between the moment and the rotation of the foundation. Figure 2.4 illustrates the relationship between the rotation displacement and the overturning moment, with M_0 and θ_0 representing the overturning moment and the rotation deformation at the starting point of the foundation uplift, respectively. These values are computed using Equations (2.1) and (2.2), respectively, where W is the building weight, and K_{R0} represents the rotational spring constant of the soil–foundation system. Figure 2.4 shows that the relationship between the overturning moment and the rotation deformation becomes a nonlinear behavior when the overturning moment (M) is more than the overturning moment at the uplift initiation (M_0). The overturning moment (M) is calculated by Equation (2.3).

$$M_o = \frac{WB}{6} \tag{2.1}$$

$$\theta_o = \frac{M_0}{K_{R0}} \tag{2.2}$$

$$M = M_0\left(3 - 2\sqrt{\frac{\theta_0}{\theta}}\right) \tag{2.3}$$

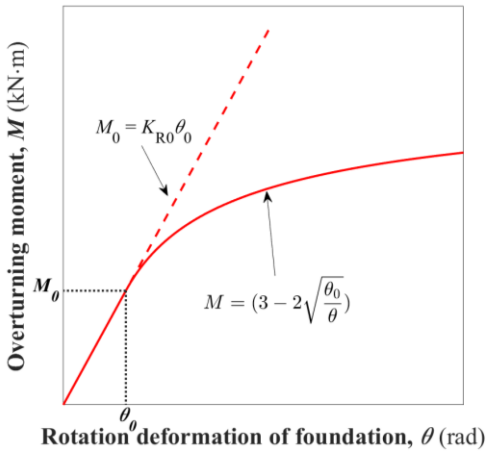

Figure 2.4 Overturning moment and rotation deformation relationship of the shallow foundation considering the foundation uplift

This chapter presents two representative models for calculating the seismic response considering the foundation uplift: the macroelement and horizontal–vertical interactive sway-rocking models. Both numerical models are basically sway-rocking models that consider the nonlinear relationship between the overturning moment and the rotation. The theory of both models is described in subsequent sections.

2.3.1 Macroelement model

The current study uses the macroelement model developed by Nakatani et al. [1] because it considers the soil nonlinearity and the foundation uplift phenomenon. Referring to Nakatani et al. [1] and Shirato et al. [17], the macroelement model and the elasto-uplift-plastic macroelement proposed by Nakatani et al. [1] will be summarized in this section.

The macroelement theory was invented by Nova and Montrasio [12]. A macroelement treats the foundation and soil system as a rigid foundation supported by springs for the nonlinear soil–structure interaction. This macroelement expresses the behavior inside the content of the work-hardening plasticity of the soil–foundation system. Many studies developed the macroelement model [13,14]. For example, Paolucci [15] was the first to develop the elasto-plastic macroelement application to seismic problems. Cremer [16] suggested that springs exhibit nonlinear characteristics based on the plasticity theory and uplift characteristics. Nakatani et al. [10] developed the macroelement model that revised the assumption of the elastic–uplift–plastic behavior. The displacement is given in an incremental form and comprises elastic and plastic displacements. Compliance connects the incremental displacement and load. Plastic and uplifting compliances are required. In these evaluations, the yield surface, hardening law, and flow law are given based on the plasticity theory.

The total incremental displacement of the foundation vector ($\{du\}$) for the elasto-uplift-plastic macroelement model proposed by Nakatani et al. [1], consists of the elastic ($\{du^{el}\}$), uplift ($\{du^{up}\}$), and plastic ($\{du^{pl}\}$) components, as expressed in Equation (2.4). The relationship between the incremental force vector ($\{dF\}$) and the displacement (du) is presented in Equation (2.5), where $[D^{el}]$, $[D^{up}]$, and $[D^{pl}]$ are the elastic, uplift, and plastic compliances matrices, respectively. The elasto-plastic macroelement is referred to as the inverse of $D^{el} + D^{up} + D^{pl}$.

$$\{du\} = \{du^{el}\} + \{du^{up}\} + \{du^{pl}\} \tag{2.4}$$

$$\{dF\} = \left([D^{el}] + [D^{up}] + [D^{pl}] \right)^{-1} \{du\} \tag{2.5}$$

2.3.1.1 Elastic compliance

The elastic compliance matrix ($[D^{el}]$) is expressed as Equation (2.6), where K_{H0}, K_{V0}, and K_{R0} are the initial spring coefficients of the soil–foundation system described in the soil–foundation system properties (Section 2.4.5).

$$\left[D^{el}\right]=\begin{bmatrix} 1/K_{H0} & 0 & 0 \\ 0 & 1/K_{V0} & 0 \\ 0 & 0 & 1/K_{R0} \end{bmatrix} \tag{2.6}$$

2.3.1.2 Uplift compliance

Figure 2.4 indicates that the uplift compliance is determined based on the relationship between the rotation displacement and the overturning moment of the foundation. The rotation and vertical displacements of the foundation in the uplift component are expressed as Equations (2.7) and (2.8), respectively, where M_α is the mobilized overturning moment influenced when soil becomes plastic. When the overturning moment (M) is less than the overturning moment at the foundation uplift initiation (M_0), the vertical and rotation displacements of the foundation in uplift component (v^{up} and θ^{up}, respectively) will be zero.

$$\theta^{up}=\left\{\frac{4}{(3-M/M_\alpha)^2}-\frac{M}{M_\alpha}\right\}\theta_0 \tag{2.7}$$

$$v^{up}=-\frac{B}{2}\left\{\frac{4}{(3-M/M_\alpha)^2}-\frac{4}{(3-M/M_\alpha)}+1\right\} \tag{2.8}$$

A weight function is applied to the uplift compliance because the uplift component will be predominant when the dead load decreases. Therefore, the uplift compliance matrix ($[D^{up}]$) is written as Equation (2.9), where V_0 is the dead load, and V_m is the ultimate bearing capacity in terms of the vertical loading.

$$\left[D^{up}\right]=\begin{bmatrix} 0 & 0 & 0 \\ 0 & 0 & \left(1-\dfrac{V_0}{V_m}\right)\left(\dfrac{\partial v^{up}}{\partial M}\right) \\ 0 & 0 & \left(1-\dfrac{V_0}{V_m}\right)\left(\dfrac{\partial \theta^{up}}{\partial M}\right) \end{bmatrix} \tag{2.9}$$

2.3.1.3 Plastic compliance

The bearing capacity surface is necessary to describe the plastic component. Nova and Montrasio [12] expressed the bearing capacity surface in Equation (2.10), where $h = H/(\mu V_m)$; $m = M/(\psi B V_m)$; and $\xi = V/(V_m)$. The foundation's bearing capacity is estimated as a rugby ball

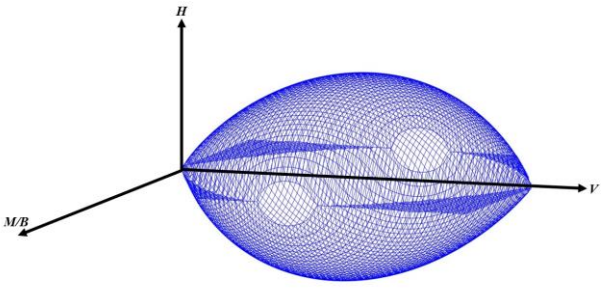

Figure 2.5 Diagrammatic bearing capacity surface

shaped in the function *H*–*V*–*M*/*B*, as presented in Figure 2.5.

$$f_{cr} = h^2 + m^2 - \xi^2(1-\xi)^{2\zeta} = 0 \tag{2.10}$$

The yield function expressed in Equation (2.11) is used to describe the plastic deformation based on Nova and Montrasio [12], where ρ_c is the hidden parameter determining the immediate capacity of the yield surface and converting the instantaneous combined loads into the magnitude of an equivalent vertical force. The yield surface is specified by parameters μ, ψ, and ζ.

$$f_y = h^2 + m^2 - \xi^2(1-\xi/\rho_c)^{2\zeta} = 0 \tag{2.11}$$

Assuming that the soil is plastic hardening, the yield surface size develops based on the hardening rule. The hardening function is approximated by an exponential function, as shown in Equation (2.12), where the geometric mean of the plastic components in the horizontal, vertical, and rotational displacements (v_c) is expressed in Equation (2.13). Parameters R_0, α_M, and γ_M prescribe the yield surface size based on the hardening rule.

$$\rho_c = 1 - \exp\left(-\frac{R_0 v_c}{V_m}\right) \tag{2.12}$$

$$v_c = \left\{\left(\alpha_M u^{pl}\right)^2 + \left(v^{pl}\right)^2 + \left(\gamma_M B\theta^{pl}\right)^2\right\}^{0.5} \tag{2.13}$$

The rating form of the hardening function is written as Equation (2.14) by using the Taylor expansion, taking the first-order term, and obtaining the incremental displacement (*du*, *dv*, and *dθ*).

$$d\rho_c = (1-\rho_c)\frac{R_0}{V_M}\left(\alpha_M\left|du^{pl}\right| + \left|dv^{pl}\right| + \gamma_M B\left|d\theta^{pl}\right|\right) \tag{2.14}$$

The incremental plastic component is expressed as Equations (2.15)–(2.17), where g is the plastic potential function computed by Equation (2.18). Parameters λ and χ are the nonlinear

soil behavior beyond the yielding point. Λ is a scalar parameter calculated by Equation (2.1.9) proposed by Nova and Montrasio [12].

$$du^{\mathrm{pl}} = \Lambda \frac{\partial g}{\partial H} \tag{2.15}$$

$$dv^{\mathrm{pl}} = \Lambda \frac{\partial g}{\partial V} \tag{2.16}$$

$$d\theta^{\mathrm{pl}} = \Lambda \frac{\partial g}{\partial M} \tag{2.17}$$

$$g = \lambda^2 h^2 + \chi^2 m^2 - \xi^2 (1 - \xi / \rho_g)^{2\zeta} = 0 \tag{2.18}$$

$$\Lambda = -\frac{\left(\frac{\partial f_y}{\partial H} dH + \frac{\partial f_y}{\partial V} dV + \frac{\partial f_y}{\partial M} dM \right)}{\frac{\partial f_y}{\partial \rho_{\mathrm{c}}} (1 - \rho_{\mathrm{c}}) \frac{R_0}{V_{\mathrm{M}}} \left(\alpha_M \left| \frac{\partial g}{\partial H} \right| + \left| \frac{\partial g}{\partial V} \right| + \gamma_M B \left| \frac{\partial g}{\partial M} \right| \right)} \tag{2.19}$$

The plastic compliance matrix is eventually expressed as Equation (2.20).

$$D^{\mathrm{pl}} = \Lambda \begin{bmatrix} \frac{\partial f_y}{\partial H}\frac{\partial g}{\partial H} & \frac{\partial f_y}{\partial H}\frac{\partial g}{\partial V} & \frac{\partial f_y}{\partial H}\frac{\partial g}{\partial M} \\ \frac{\partial f_y}{\partial V}\frac{\partial g}{\partial H} & \frac{\partial f_y}{\partial V}\frac{\partial g}{\partial V} & \frac{\partial f_y}{\partial V}\frac{\partial g}{\partial M} \\ \frac{\partial f_y}{\partial M}\frac{\partial g}{\partial H} & \frac{\partial f_y}{\partial M}\frac{\partial g}{\partial V} & \frac{\partial f_y}{\partial M}\frac{\partial g}{\partial M} \end{bmatrix} \tag{2.20}$$

Based on Nova and Montrasio [12] suggestion and referring to Nakatani et al. [1], Table 2.1 summarizes the parameters describing the nonlinear behavior of the macroelement model.

Table 2.1 Parameter setting for the nonlinear behavior of the macroelement model (referred to Nakatani et al. [1])

Parameters		Value
Yield function	μ	0.90
	ψ	0.48
	ζ	0.95
Hardening function	R_0	48946
	α_{M}	2.80
	γ_{M}	1.70
Plastic potential	λ	0.45
	χ	0.45

2.3.2 Horizontal–vertical interactive sway-rocking model

A horizontal–vertical interactive SR model is one convenient model for evaluating the seismic responses considering the foundation uplift [2,6]. According to the TDAP III manual [18] and the Nuclear Standard Committee of Japan Electric Association (JEA) [19], the foundation uplift analysis method depends on the ground contact ratio (η). η indicates the area at the base of the foundation in contact with the soil (i.e., the ground contact ratio can represent the degree of the foundation uplift). It can be calculated using Equation (2.21), where the coefficients are according to the ground reaction force distribution (α). α is 6 when the triangle distribution is considered and 4.7 when the rigid plate distribution is taken.

$$\eta = \frac{2\alpha}{\alpha - 2}\left(\frac{1}{2} - \frac{M}{WB}\right) = \left(\sqrt{\frac{\theta_0}{\theta}}\right)^{\frac{2}{\alpha-2}} \tag{2.21}$$

The seismic response analysis methods that consider the foundation uplift are classified into three categories based on the level of the foundation uplift. Based on the information provided in the TDAP III manual [18] and the Nuclear Standard Committee of JEA [19], this classification is explained below and summarized in a flow chart in Figure 2.6.

2.3.2.1 When the ground contact ratio is $\eta \geq 75\%$

A linear uplift seismic response analysis is considered acceptable when the foundation uplift is approximately less than 1/4 of the foundation width.

2.3.2.2 When the ground contact ratio is $\eta \geq 65\%$

A nonlinear SR model is used for the seismic response analysis when the ground contact

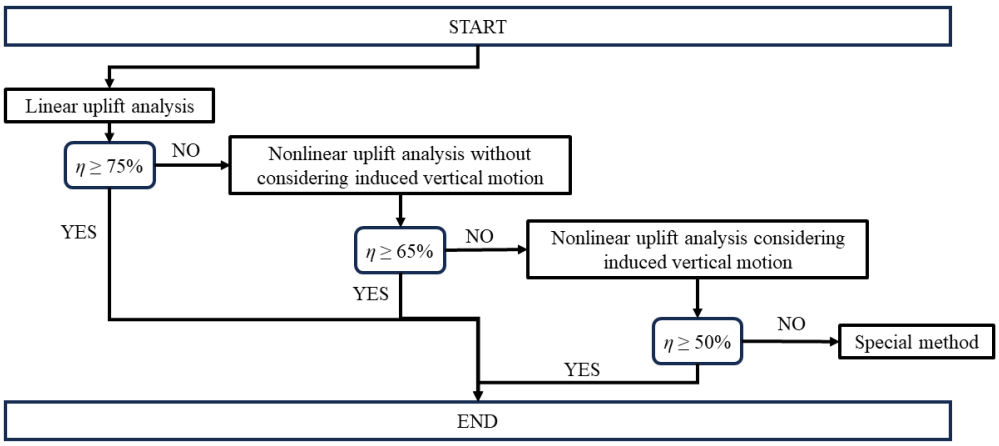

Figure 2.6 Flowchart of foundation uplift evaluation methods of the horizontal-vertical interactive SR model

ratio (η) is greater than or equal to 65%. However, in this analysis method, the induced vertical motion of the foundation is not considered because it is assumed to have a negligible impact on the structure response. This assumption is based on the observation that the vertical motion induced by the rocking motion of the foundation is typically small compared to the horizontal motion; therefore, it can be ignored for the seismic response analysis [2,6-7,20].

2.3.2.3 When the ground contact ratio is 65% > $\eta \geq$ 50%

Therefore, the nonlinear seismic response analysis for the uplift is performed using the SR model that considers the induced vertical motion. The model considers the vertical motion induced by the coupling of the rotational and vertical degrees of freedom when the foundation uplifts. The induced vertical motions caused by the uplift must be considered when the ground contact ratio (η) ranges from 50 to 65%. Neglecting this effect can lead to inaccurate results [2,6-7,20]. The SR model considers the vertical motion induced by the coupling of the rotational and vertical degrees of freedom when the foundation uplift occurs during the seismic motion.

However, a special evaluation method is required when the ground contact ratio is less than 50%. This special evaluation method indicates that the accurate evaluation method for the foundation uplift phenomenon is essentially necessary when the ground contact ratio is low.

When the foundation uplift occurs during an earthquake ground motion, the geometrical nonlinearity caused by the foundation uplift will be considered in the stiffness and damping of the soil–foundation system. The stiffness and the damping matrix of this soil–structure system are written as Equations (2.22) and (2.23), respectively. The evaluation formula for the soil stiffness and damping are Equations (2.24)–(2.28), where the parameters dealing with the vertical spring nonlinearity (β) are equal to 0.46 [2,6].

$$[K_F] = \begin{bmatrix} K_{H0} & 0 & 0 \\ 0 & K_{VV} & K_{VR} \\ 0 & K_{VR} & K_{RR} \end{bmatrix} \tag{2.22}$$

$$[C_F] = \begin{bmatrix} C_{H0} & 0 & 0 \\ 0 & C_{VV} & 0 \\ 0 & 0 & C_{RR} \end{bmatrix} \tag{2.23}$$

$$K_{VV} = \eta^{\beta} K_{V0} \tag{2.24}$$

$$K_{VR} = \frac{1-\eta}{2} B K_{VV} \tag{2.25}$$

$$K_{RR} = \frac{M - K_{VR}\nu}{\theta} \tag{2.26}$$

$$C_{VV} = \eta^{\frac{\alpha}{2}} C_{V0} \tag{2.27}$$

$$C_{RR} = \eta^{\frac{\alpha}{2}} C_{R0} \tag{2.28}$$

2.4 Numerical Evaluation Method and Structural Properties

The governing equation for this system is expressed as Equation (2.29), where [M] is the mass matrix; [C] is the damping matrix of the structure and soil–foundation system; [K_S] is the structural stiffness matrix; {$\ddot{u}$}, {$\dot{u}$}, and {u} are the acceleration, velocity, and displacement response vectors, respectively; and {P} is the external force vector. The ground reaction force vector denoted as {F_{HD}} is calculated by Equation (2.30), where [K_F] is the soil–foundation system matrix.

$$[M]\{\ddot{u}\} + [C]\{\dot{u}\} + [K_S]\{u\} + \{F_{HD}\} = \{P\} \tag{2.29}$$

$$\{F_{HD}\} = [K_F] \begin{Bmatrix} u \\ v \\ \theta \end{Bmatrix} = \begin{Bmatrix} H \\ V \\ M \end{Bmatrix} \tag{2.30}$$

2.4.1 Time-step methods

Newmark's method is used herein to calculate the structural responses considering the foundation uplift. Referring to a Structural Dynamics textbook [11], Newmark developed the calculation method for obtaining the displacement, velocity, and acceleration response at $t = t + dt$ based on the following equations, where γ and β are Newmark's parameters that correspond to 0.5 and 0.25, respectively, in this study:

$$\dot{u}_{t+dt} = \dot{u}_t + (1-\gamma) dt \ddot{u}_t + \gamma dt \ddot{u}_{t+1} \tag{2.31}$$

$$u_{t+dt} = u_t + dt\dot{u}_t + \left[\left(\frac{1}{2} - \beta \right) \left(dt^2 \right) \right] \ddot{u}_t + \left(\beta dt^2 \right) \ddot{u}_{t+1} \tag{2.32}$$

From Equations (2.31) and (2.32), the acceleration at $t + dt$ is expressed as Equation (2.33).

$$\ddot{u}_{t+dt} = \frac{1}{\beta dt^2} (u_{t+dt} - u_t) - \frac{1}{\beta dt} \dot{u}_t - \left(\frac{1}{2\beta} - 1 \right) \ddot{u}_t \tag{2.33}$$

Substituting Equation (2.33) into Equation (2.31),

$$\dot{u}_{t+dt} = \frac{\gamma}{\beta dt} (u_{t+dt} - u_t) + \left(1 - \frac{\gamma}{\beta} \right) \dot{u}_t + \left(1 - \frac{\gamma}{2\beta} \right) \ddot{u}_t \tag{2.34}$$

At time = $t + dt$, the governing equation is written as Equation (2.35).

$$[M]\{\ddot{u}_{t+dt}\}+[C]\{\dot{u}_{t+dt}\}+[K_S]\{u_{t+dt}\}+\{F_{HD_{t+dt}}\}=\{P_{t+dt}\} \tag{2.35}$$

Next, substituting Equations (2.31) and (2.33) into Equation (2.35),

$$\begin{aligned}&\left(\frac{[M]}{\beta dt^2}+\frac{\gamma[C]}{\beta dt}+[K_S]\right)\{u_{t+dt}\}+\{F_{HD_{t+dt}}\}=\{P_{t+dt}\}+\\&[M]\left\{\left(\frac{1}{2\beta}-1\right)\{\ddot{u}_t\}+\frac{1}{\beta dt}\{\dot{u}_t\}+\frac{1}{\beta dt^2}\{u_t\}\right\}\\&+[C]\left\{\left(\frac{\gamma}{2\beta}-1\right)\{\ddot{u}_t\}dt+\left(\frac{\gamma}{\beta}-1\right)\{\dot{u}_t\}+\frac{\gamma}{\beta dt}\{u_t\}\right\}\end{aligned} \tag{2.36}$$

$\{F_{HD}\}$ at $t + dt$ is computed by Equation (2.37), where the incremental displacement ($\{du\}$) is computed by Equation (2.38).

$$\{F_{HD_{t+dt}}\}=\{F_{HD_t}\}+[K_F]\{du_{F_t}\} \tag{2.37}$$

$$\{du_{F_t}\}=\{u_{F_{t+dt}}\}-\{u_{F_t}\} \tag{2.38}$$

Substituting Equations (2.37) and (2.38) in Equation (2.36), the governing equation is rewritten as Equation (2.39).

$$\begin{aligned}&\left(\frac{[M]}{\beta dt^2}+\frac{[C]}{\beta dt}+[K_S]+[K_F]\right)\{x_{t+dt}\}+\{F_{HD_t}\}-[K_F]\{u_t\}=\{P_{t+dt}\}+\\&[M]\left\{\left(\frac{1}{2\beta}-1\right)\{\ddot{u}_t\}+\frac{1}{\beta dt}\{\dot{u}_t\}+\frac{1}{\beta dt^2}\{u_t\}\right\}\\&+[C]\left\{\left(\frac{\gamma}{2\beta}-1\right)\{\ddot{u}_t\}dt+\left(\frac{\gamma}{\beta}-1\right)\{\dot{u}_t\}+\frac{\gamma}{\beta dt}\{u_t\}\right\}\end{aligned} \tag{2.39}$$

Revising Equation (2.39) into an incremental displacement term results in Equation (2.40). The incremental displacement is finally computed in Equation (2.41).

$$\begin{aligned}&\left(\frac{[M]}{\beta dt^2}+\frac{[C]}{\beta dt}+[K_S]+[K_F]\right)\{du_t\}=\{P_{t+dt}\}+[M]\left\{\left(\frac{1}{2\beta}-1\right)\{\ddot{u}_t\}+\frac{1}{\beta dt}\{\dot{u}_t\}\right\}\\&+[C]\left\{\left(\frac{\gamma}{2\beta}-1\right)\{\ddot{u}_t\}dt+\left(\frac{\gamma}{\beta}-1\right)\{\dot{u}_t\}\right\}+[K_F]\{x_t\}-\{F_{HD_t}\}\end{aligned} \tag{2.40}$$

$$\{du_t\}=\left[\hat{k}\right]^{-1}\{\hat{p}_{t+1}\}, \tag{2.41}$$

where the effective load vector $\{\hat{p}_{t+1}\}$ is the right term for Equation (2.40), as expressed in Equation (2.42).

$$\begin{aligned}\{\hat{p}_{t+1}\} &= \{P_{t+dt}\} + [M]\left\{\left(\frac{1}{2\beta}-1\right)\{\ddot{u}_t\} + \frac{1}{\beta dt}\{\dot{u}_t\}\right\} \\ &+ [C]\left\{\left(\frac{\gamma}{2\beta}-1\right)\{\ddot{u}_t\}\,dt + \left(\frac{\gamma}{\beta}-1\right)\{\dot{u}_t\}\right\} - [K_s]\{u_t\} - \{F_t\}\end{aligned} \tag{2.42}$$

The effective stiffness matrix ($\hat{k}$) is the left term in Equation (2.40), as presented in Equation (2.43).

$$\left[\hat{k}\right] = \left(\frac{[M]}{\beta dt^2} + \frac{[C]}{\beta dt} + [K_S] + [K_F]\right) \tag{2.43}$$

The mass matrix, structural stiffness matrix, structural damping matrix, and stiffness and damping matrix of the soil–foundation system are described in the subsequent section by referring to the TDAP manual [18].

2.4.2 Mass properties

This study considers analytical models comprising lumped mass and beam elements on a rigid foundation, as shown in Figure 2.7. Each lumped mass has one degree of freedom (i.e., horizontal direction). A foundation has three degrees of freedom (i.e., horizontal, vertical, and rotational directions) because it can translate in the horizontal and vertical directions and rotate. The mass matrix [*M*] is expressed as Equation (2.44), where *m* is the mass of each node, and m_f and J_f are the mass and the rotation mass inertia of the foundation, respectively.

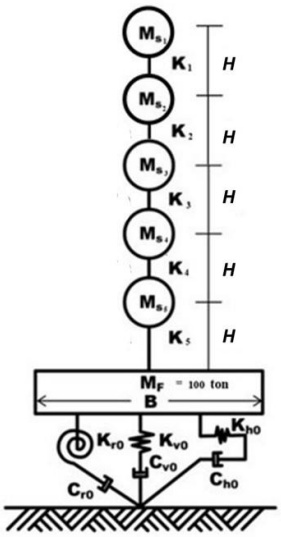

Figure 2.8 Example of an analytical model

$$[M]=\begin{bmatrix} m_1 & & & & & & \\ & m_2 & & & & & \\ & & m_3 & & & & \\ & & & \ddots & & & \\ & & & & \ddots & & \\ & & & & & m_f & \\ & & & & & & m_f \\ & & & & & & & J_f \end{bmatrix} \tag{2.44}$$

2.4.3 Stiffness properties (beam element)

This study generates a stiffness matrix using beam elements. The stiffness matrix [*K*] is expressed as Equation (2.45), where *k* is the spring constant; *N* is the node number; *E* is the Young's modulus; *I* is the moment inertia; *A* is the cross-sectional area; and *L* is the beam length.

$$[K]=\begin{bmatrix} k_1 & -k_1 & 0 & 0 & \cdots & \cdots & 0 & 0 \\ -k_1 & k_1+k_2 & -k_2 & 0 & \cdots & \cdots & 0 & 0 \\ 0 & -k_2 & k_2+k_3 & -k_3 & \cdots & \cdots & 0 & 0 \\ 0 & 0 & \vdots & \ddots & \ddots & \vdots & \vdots & \vdots \\ \vdots & \vdots & \vdots & -k_{N-2} & k_{N-2}+k_{N-1} & -k_{N-1} & 0 & -\dfrac{6EI}{L^2} \\ \vdots & \vdots & \vdots & 0 & -k_{N-1} & k_N & 0 & \dfrac{6EI}{L^2} \\ 0 & 0 & 0 & 0 & 0 & 0 & \dfrac{EA}{L} & 0 \\ 0 & 0 & 0 & 0 & -\dfrac{6EI}{L^2} & \dfrac{6EI}{L^2} & 0 & \dfrac{4EI}{L} \end{bmatrix} \tag{2.45}$$

2.4.4 Damping properties

The structural damping matrix is generated by Equation (2.46), where δ is the damping coefficient, and f_0 is the rocking frequency that is computed by Equation (2.47), where *J* is the rotation mass inertia of the foundation, and K_{R0} is the initial spring constant of the soil–foundation system corresponding to the rotational direction.

$$[C]=\frac{\delta}{\pi f_0}[K] \tag{2.46}$$

$$f_0 = \frac{1}{2\pi}\sqrt{\frac{K_{R0}}{J_f}} \tag{2.47}$$

2.4.5 Soil–foundation system properties

This study treats the soil–foundation system as a rigid foundation supported by springs and dashpots, as shown in Figure 2.7. These springs and dashpots represent the stiffness and damping characteristics of the soil–foundation system. The initial stiffness and initial damping matrices of the soil–foundation system are expressed by Equations (2.48) and (2.49), respectively, where K_{H0}, K_{V0}, and K_{R0} are the initial spring constants of the soil–foundation system corresponding to the horizontal, vertical, and rotational directions, respectively, and C_{H0}, C_{V0}, and C_{R0} are the initial damping coefficients of the soil–foundation system corresponding to the horizontal, vertical, and rotational directions, respectively. The spring constants and the damping coefficients for the soil–foundation system are calculated using Equations (2.50)–(2.56) proposed by Gazetas [21], where G is the soil shear modulus; υ is Poisson's ratio; V_s is the shear wave velocity; ρ is the soil density; A is the foundation area; and I_f is the moment inertia of the foundation. The coefficient indicating the frequency dependence of the damping vertical ($\overline{C}_v$) and rotational ($\overline{C}_r$) are 0.9 and 0.2, respectively [1].

$$[K_F] = \begin{bmatrix} K_{H0} & 0 & 0 \\ 0 & K_{V0} & 0 \\ 0 & 0 & K_{R0} \end{bmatrix} \tag{2.48}$$

$$[C_F] = \begin{bmatrix} C_{H0} & 0 & 0 \\ 0 & C_{V0} & 0 \\ 0 & 0 & C_{R0} \end{bmatrix} \tag{2.49}$$

$$K_{H0} = \frac{9G(B/2)}{2-\nu} \tag{2.50}$$

$$K_{V0} = \frac{4.5G(B/2)}{1-\nu} \tag{2.51}$$

$$K_{R0} = \frac{3.6G(B/2)^3}{1-\nu} \tag{2.52}$$

$$C_{H0} = \rho V_S A \tag{2.53}$$

$$C_{V0} = \rho V_{LA} A\overline{C_V} \tag{2.54}$$

$$C_{R0} = \rho V_{LA} I_f \overline{C_R} \tag{2.55}$$

$$V_{LA} = \frac{3.4}{\pi(1-\nu)} V_S \tag{2.56}$$

2.5 Analytical Models

Reports on the structural damage caused by the 2011 Tohoku Earthquake and Tsunami events [22] revealed that low-rise buildings on a shallow foundation were the most significantly damaged buildings during these events. However, Suppasri et al. [23] reported that five reinforced concrete buildings were overturned by the 2011 Great East Japan Tsunami in Onagawa town, and two of the five buildings were built on a shallow foundation. Nevertheless, pile foundation damage was observed in buildings with pile foundations, making the resisting moment against the overturning moment primarily rely on the building's self-weight. Therefore, this study focuses on two building types, i.e., low- and medium-rise buildings, supported by a shallow foundation sustained on three soil conditions (soft, stiff, and rocky) as the analytical models to discuss universality results.

2.5.1 Low-rise building

A low-rise building is a type of structure typically with a maximum height of approximately three or four stories. The specific height for low-rise structures varies depending on local building codes. This study assumes a three-story analytical model supported by a mat foundation demonstrated in Figure 2.8 as a low-rise building. Table 2.2 presents the parameters for this low-rise analytical model with reference to Tokimatsu et al. [24] and Latcharote et al. [25].

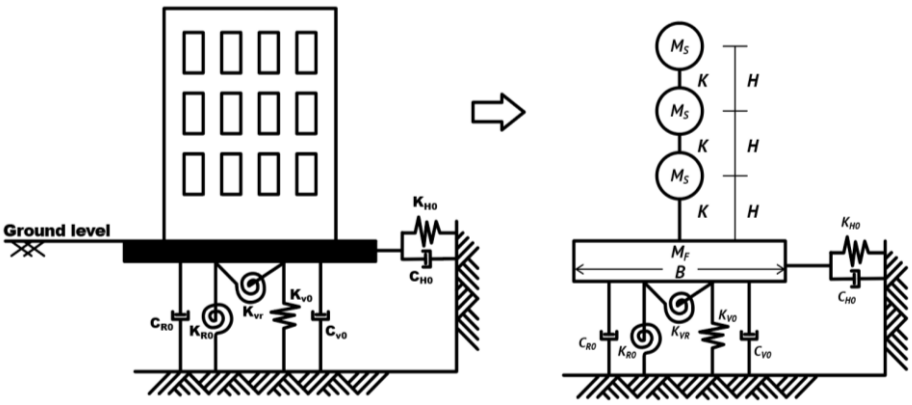

Figure 2.8 Low-rise building analytical model

Table 2.2 Parameters for the low-rise building analytical model

Parameters	Values
Lumped mass, M_S (t)	200
Foundation mass, M_F (t)	100
Rotation inertia mass of the foundation, J (t·m^2)	840
Height, H (m)	3.5
Damping coefficient of the structure, η	0.05
Young modulus, E (kN/m^2)	2×10^8
Moment of inertia, I (m^4)	0.018
Cross section area, A (m^2)	1.00
Foundation width, B (m)	10
Natural period of the structure at the first mode for the fixed-base case, T_1 (s)	0.1989
Natural period of the structure at the first mode for the soil–structure interaction system, T_1 (s)	0.2122

2.5.2 Medium-rise building

A medium-rise building typically has stories ranging between five and eight stories and a height less than 30 m. However, the classification depends on the local building codes. Referring to Osaki [26], the five-story structure model demonstrated in Figure 2.9 is considered

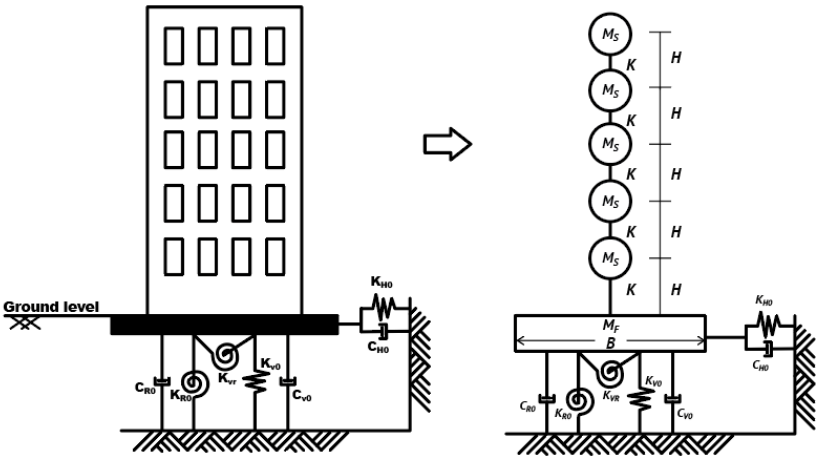

Figure 2.9 Medium-rise building analytical model

as a medium-rise building in this study. Table 2.3 presents the parameters for the medium-rise model with reference to Osaki [26].

Table 2.3 Parameters for the medium-rise building analytical model

Parameters	Values
Lumped mass, M_S (t)	50
Foundation mass, M_F (t)	100
Rotation inertia mass of foundation, J (t·m^2)	840
Height, H (m)	3.5
Damping coefficient of the structure, η	0.05
Young modulus, E (kN/m^2)	2×10^8
Moment of inertia, I (m^4)	3.4826×10^{-3}
Cross section area, A (m^2)	1.00
Foundation width, B (m)	10
Natural period of the structure at the first mode for the fixed-base case, T_1 (s)	0.3535
Natural period of the structure at the first mode for the soil–structure interaction system, T_1 (s)	0.3565

2.5.3 Soil–foundation system model

This study considers the three following soil types to examine the effect of the soil nonlinearity on the foundation uplift behavior and structural response: soft soil, stiff soil, and rock. Referring to Awlla et al. [27] and Look, B.G. [28], Table 2.4 summarizes the typical parameters for calculating the soil–foundation system. The shear modulus for different soil types is calculated using Equation (2.57). Table 2.5 summarizes the parameters of the foundation–soil system for each soil condition using Equations (2.47) and (2.50)–(2.56).

$$V_S = \sqrt{\frac{G}{\rho}} \tag{2.57}$$

Table 2.4 Shear wave velocity, density, and Poisson's ratio for different soil types

Soil types	Shear wave velocity, V_s (m/s)	Density, ρ (t/m^3)	Poisson's ratio, υ
Soft soil	150	1.6	0.40
Stiff soil	300	1.8	0.40
Rock	1000	2.0	0.25

Table 2.5 Spring constants and damping coefficients of the foundation–soil system for different soil types

Parameter	Soft soil	Stiff soil	Rock
Initial spring constants of the soil–foundation system corresponding to the horizontal direction, K_{H0} (kN/m)	1.01×10^6	4.56×10^6	5.14×10^7
Initial spring constants of the soil–foundation system corresponding to the vertical direction, K_{V0} (kN/m)	1.36×10^6	6.13×10^6	6.05×10^7
Initial spring constants of the soil–foundation system corresponding to the rotational direction, K_{R0} (kN·m/rad)	2.70×10^7	1.22×10^8	1.20×10^9
Initial damping coefficients of the soil–foundation system corresponding to the horizontal direction, C_{H0} (kN·s/m)	2.40×10^4	5.40×10^4	2.00×10^5
Initial damping coefficients of the soil–foundation system corresponding to the vertical direction, C_{V0} (kN·s/m)	3.90×10^4	8.77×10^4	2.60×10^5
Initial damping coefficients of the soil–foundation system corresponding to the rotational direction, C_{R0} (kN·s·m)	7.22×10^4	1.62×10^5	4.81×10^5
Rocking frequency, f_0 (Hz)	28.53	60.56	193.23

2.6 Earthquake Ground Motions

This study prepares two kinds of ground motions as seismic loading (i.e., inland- and subduction-type earthquakes) to discuss the effects of the frequency characteristics. Five recorded ground motions were selected from the National Research Institute for Earth Science and Disaster Resilience, Tokyo Institute of Technology, and the Pacific Earthquake Engineering Research Center. Table 2.6 provides the properties of selected ground motions, where the PGA denotes the peak ground acceleration; F_e is the predominant frequency; V_{s30} is the averaged shear-wave velocity to a depth of 30 m; and the soil type class. The details of the recorded ground motions are demonstrated in subsequent sections.

The maximum acceleration, also known as the amplitude or PGA is adjusted to discuss the effect of the ground motion intensity.

Table 2.6 Properties of the selected ground motions

Earthquake (type)	Station	PGA (cm/s^2)	F_e (Hz)	V_{s30} (m/s)	Site class
Imperial Valley (inland)	El Centro	341.695	1.477	213.44	D
Tokachi-Oki (subduction)	Hachinohe Harbor	231.030	0.378	400.00	C
Loma (inland)	Anderson Dam (L Abut)	62.917	0.562	488.77	C
Kobe (inland)	JMA	817.544	1.440	312.00	D
Chi-Chi (subduction)	CHY010	170.791	2.319	538.69	C

*Site classification: C (soft rock/dense soil), D (stiff soil)

References: [29] and [30]

NEHRP, National Earthquake Hazard Reduction Program, Recommended provisions for seismic regulations of new buildings: Part I, Provisions, FEMA 222A, Federal Emergency Management Agency, Washington, D.C., 1994.

ASCE: Minimum design loads and associated criteria for buildings and other structures, *ASCE/SEI 7-10*, 2010.

2.6.1 1940 Imperial Valley earthquake

The ground motion recorded at a site in El Centro during the Imperial Valley, California Earthquake on May 18, 1940 is presented here. This recorded ground motion was selected from the Pacific Earthquake Engineering Research Center Figure 2.10 shows the acceleration time history, spectral acceleration, and power spectrum of the ground motion recorded at a site in El Centro during this event.

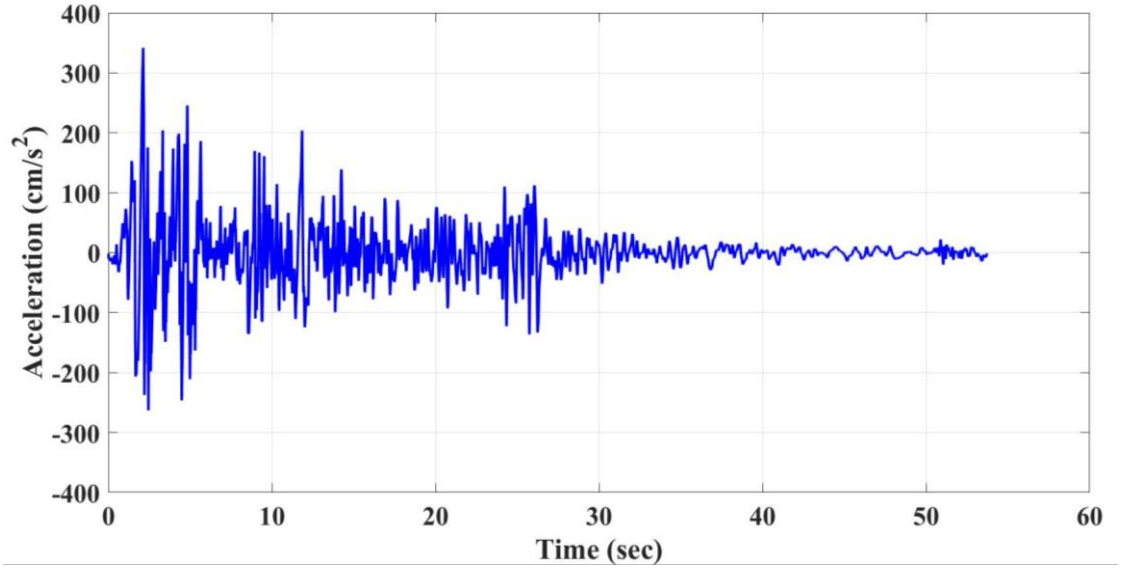

(a) Acceleration time history

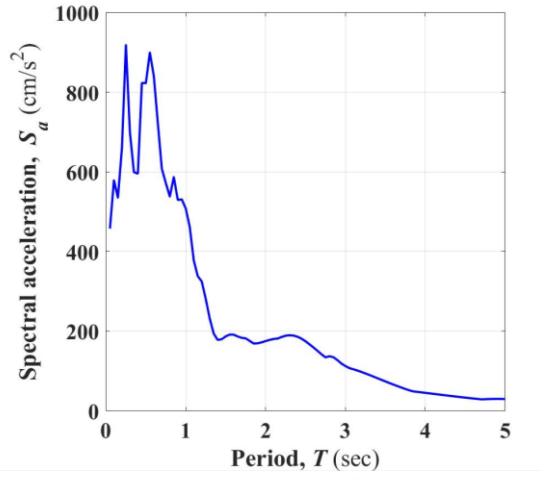

(b) Spectral acceleration

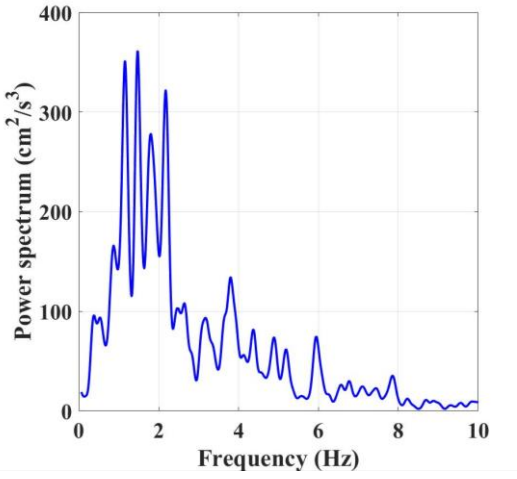

(c) Power spectrum

Figure 2.10 Recorded ground motion during the 1940 Imperial Valley Earthquake at the El Centro station

2.6.2 1968 Tokachi–Oki earthquake

The 1968 Tokachi-Oki Earthquake occurred in Japan on May 16, 1968. The ground motion recorded at Hachinohe Harbor during the 1968 Tokachi-Oki earthquake by Midorikawa and Miura, Tokyo Institute of Technology is selected in this study. Figure 2.11 presents the acceleration time history, spectral acceleration, and power spectrum of the recorded ground motion.

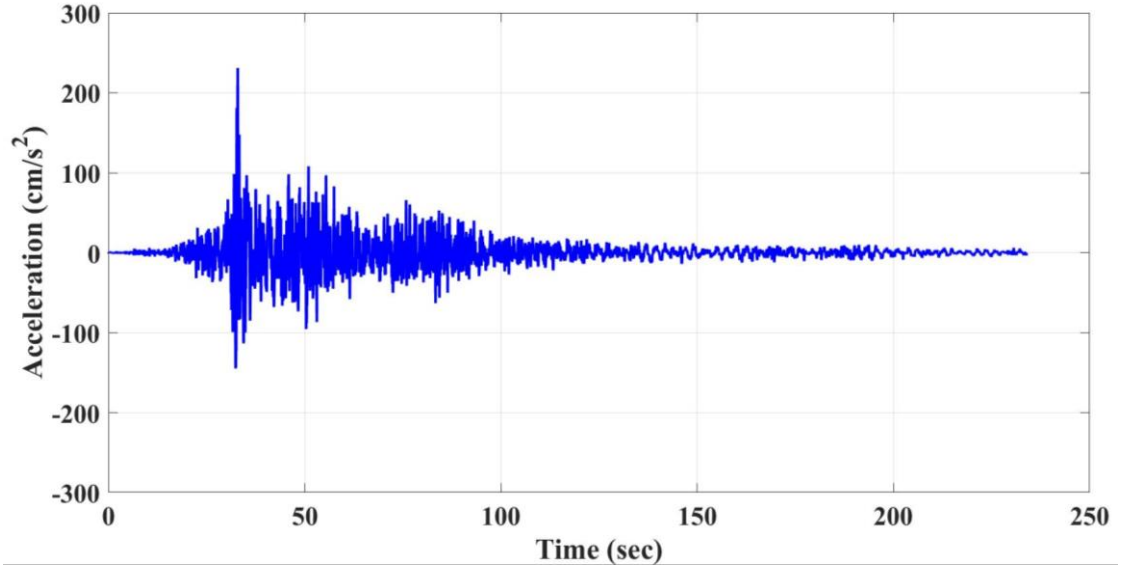

(a) Acceleration time history

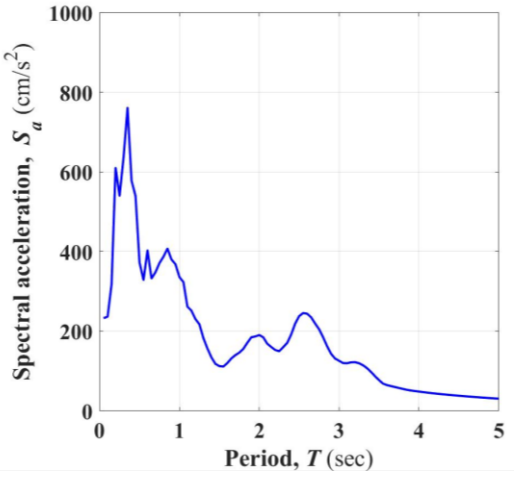

(b) Spectral acceleration

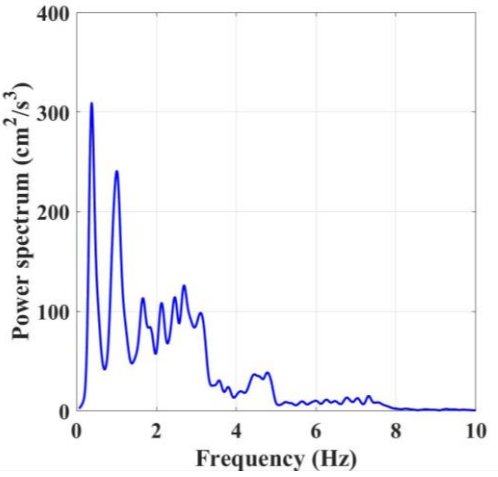

(c) Power spectrum

Figure 2.11 Recorded ground motion during the 1968 Tokachi–Oki earthquake at Hachinohe Harbor

2.6.3 1989 Loma Prieta Earthquake

The Loma Prieta Earthquake, also known as the World Series Earthquake, was a major earthquake that occurred in the San Francisco Bay Area in California on October 17, 1989. This study selects the ground motion recorded at Anderson Dam during the 1989 Loma Prieta earthquake by the Pacific Earthquake Engineering Research Center. The peak ground acceleration is 62.917 cm/s^2. The predominant frequency is approximately 0.562 Hz, as presented in Figure 2.12.

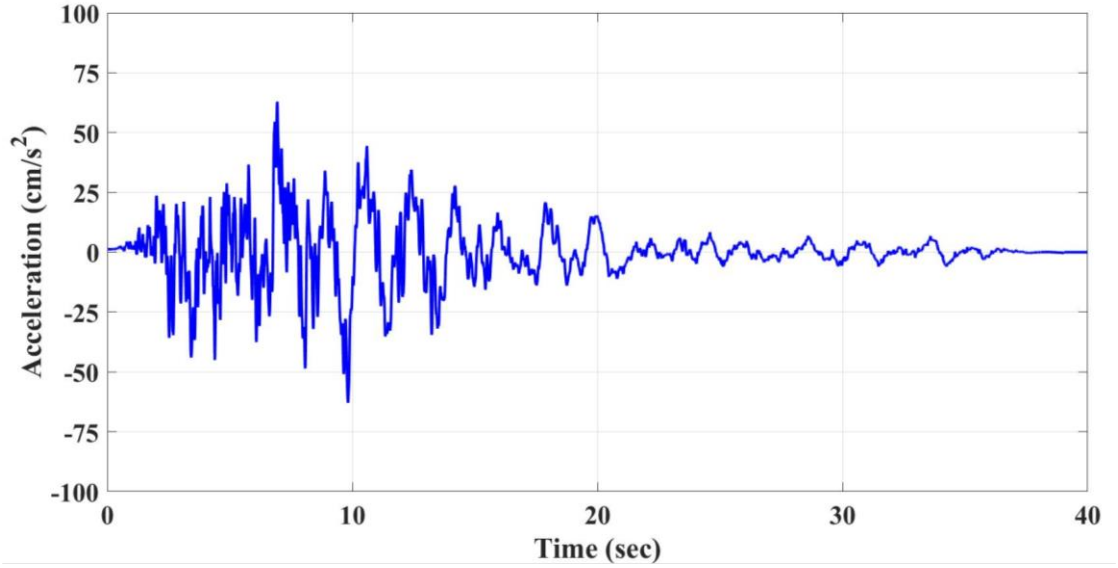

(a) Acceleration time history

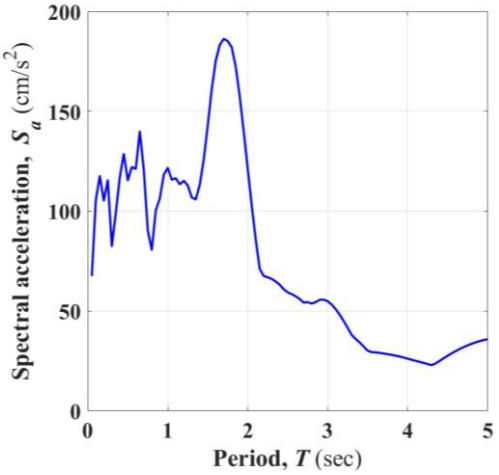

(b) Spectral acceleration

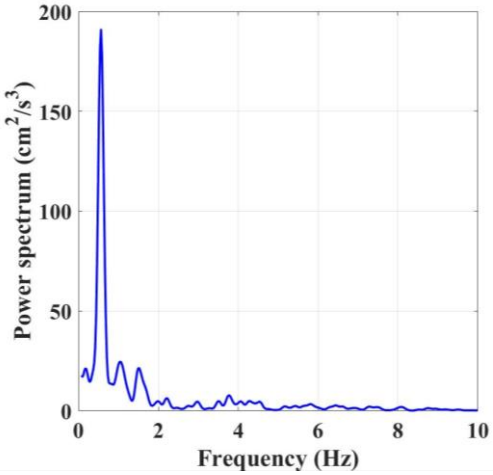

(c) Power spectrum

Figure 2.12 Recorded ground motion during the 1989 Loma Prieta Earthquake at Anderson Dam

2.6.4 1995 Kobe Earthquake

The 1995 Kobe Earthquake or the 1995 Hyogoken–Nanbu Earthquake, also known as the Great Hanshin Earthquake, was an extremely intensive earthquake that struck the city of Kobe and its surrounding areas in Japan on January 17, 1995. This study selected the ground motion recorded in Kobe (EW component) by Japan Meteorological Agency. Figure 2.13 illustrates the acceleration time history, spectral acceleration, and power spectrum of the ground motion recorded at the KJMA station during this event.

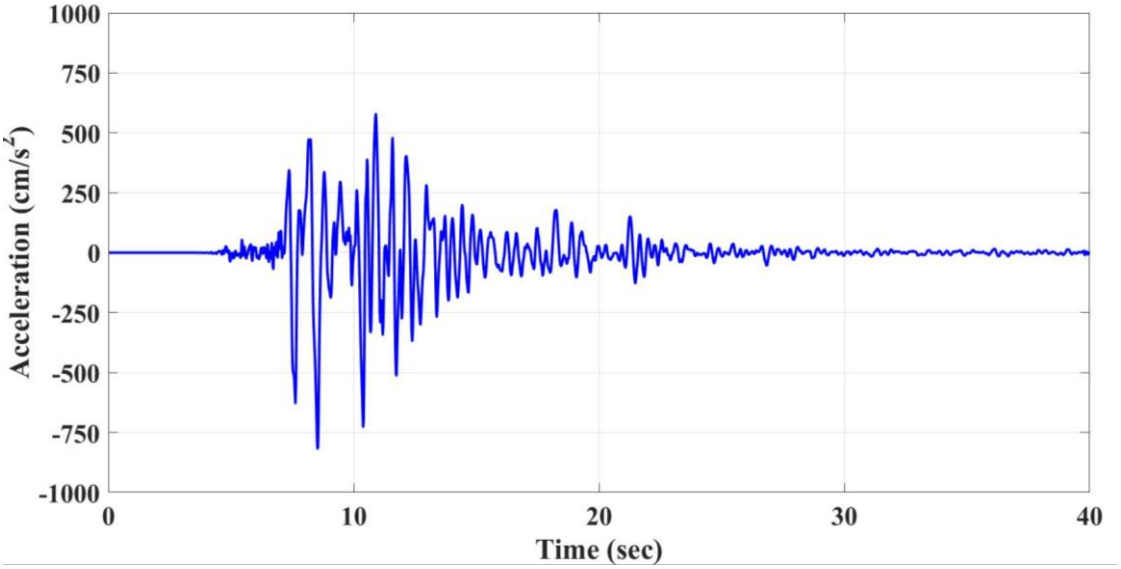

(a) Acceleration time history

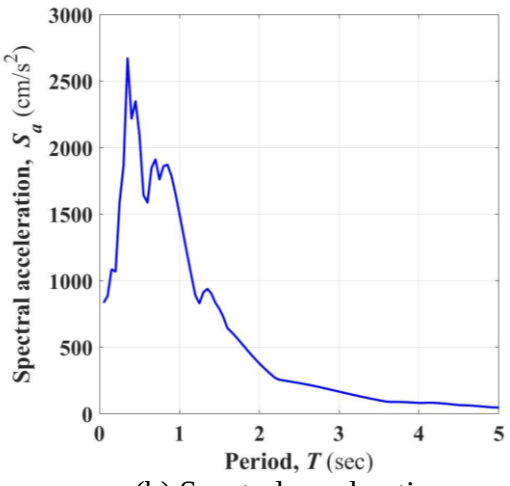

(b) Spectral acceleration

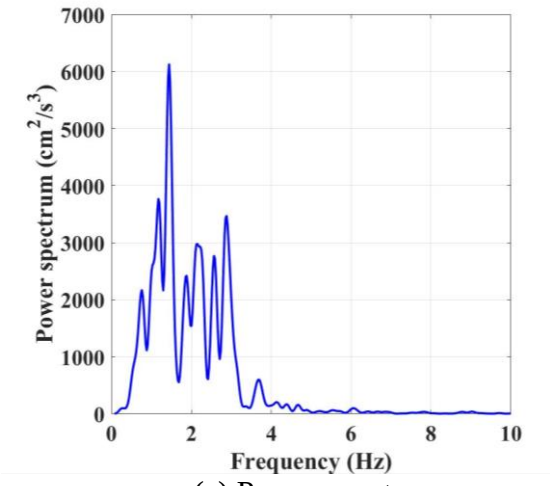

(c) Power spectrum

Figure 2.13 Recorded ground motion during the 1995 Kobe Earthquake at the JMA station

2.6.5 1999 Chi–Chi Earthquake

The Chi–Chi Earthquake that occurred at the center of Taiwan on September 21, 1999 was a large earthquake. The ground motion recorded at the CHY010 station during the 1999 Chi-Chi earthquake by Pacific Earthquake Engineering Research Center (PEER) is selected in this study as shown in Figure 2.14. According to Figure 2.14 The peak ground acceleration is 170.791 cm/s^2. The predominant frequency is approximately 2.319 Hz.

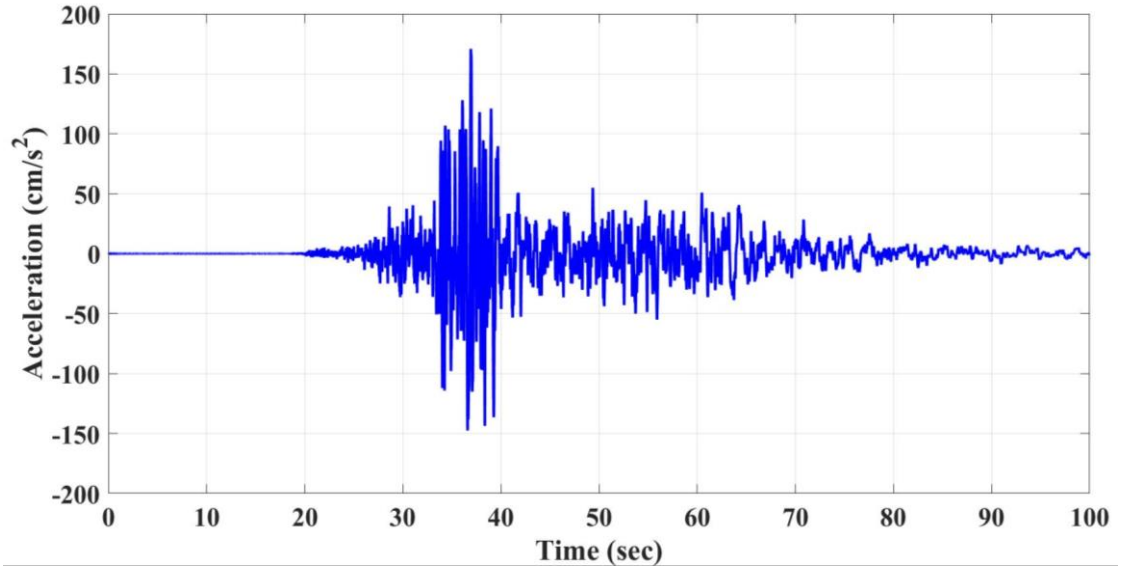

(a) Acceleration time history

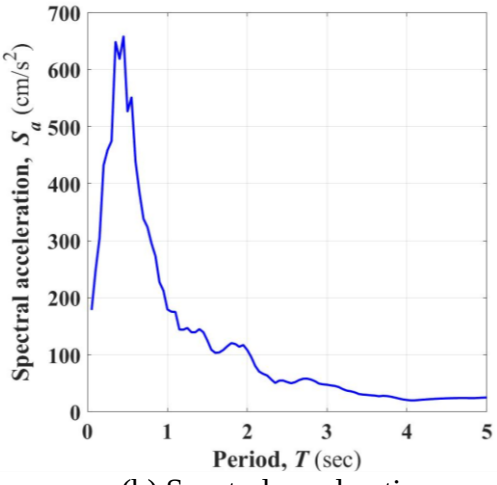

(b) Spectral acceleration

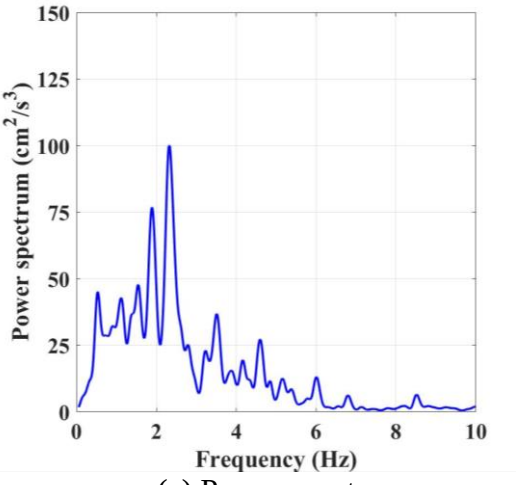

(c) Power spectrum

Figure 2.14 Recorded ground motion during the 1999 Chi–Chi Earthquake at the CHY010 station

2.7 Seismic Responses in Time History

This section compares structural responses using two numerical models considering the foundation uplift to discuss the influence of the soil and geometrical nonlinearities on the uplift behavior and examine the models' reliability and suitability. The computation results are compared and discussed from the viewpoint of the following:

(1) the structure sustained on different soil types;

(2) structural (horizontal direction) and foundation (rotational direction) responses; and

(3) foundation behavior (overturning moment and ground contact ratio)

Figure 2.15 compares the structural responses when a five-story building sustained on three different soil conditions was subjected to the recorded ground motion at El Centro during the 1940 Imperial Earthquake for the horizontal–vertical interactive SR and macroelement models. Figures 2.15(a)–(c) compare the structural responses of both numerical models for the structure founded on soft soil, stiff soil, and rock, respectively. Figure 2.15 shows that the structural responses for the macroelement model are almost equivalent to those for the horizontal–vertical interactive SR model, except when the structure is on soft soil. The structural response for the macroelement model significantly deviates for soft soil and comparatively differs from that for the horizontal–vertical interactive SR model. Soft soil exhibits a nonlinear behavior. Figures 2.16(a)–(c) illustrate the rotational displacement of the foundation of the horizontal–vertical interactive SR and macroelement models for the structure on soft soil, stiff soil, and rock, respectively. The responses for the structure founded on soft soil do not fluctuate around zero displacement, as illustrated in Figure 2.16(a). Figure 2.16(b) presents that the stiff soil responses slightly deviate, which may lightly affect the structural response and resulted in a similar structural response for the macroelement and horizontal–vertical interactive SR models, as indicated in Figure 2.15(b). The rotational displacement for the horizontal–vertical interactive SR model is almost equivalent to that for the macroelement model.

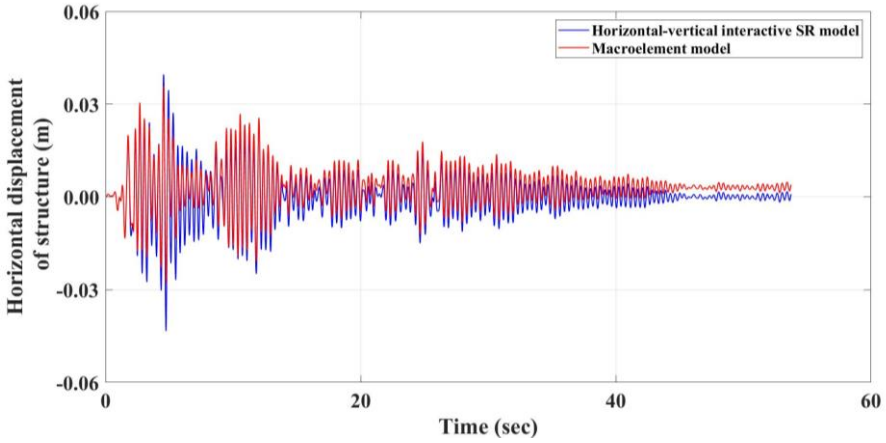

(a) When the structure is sustained on soft soil.

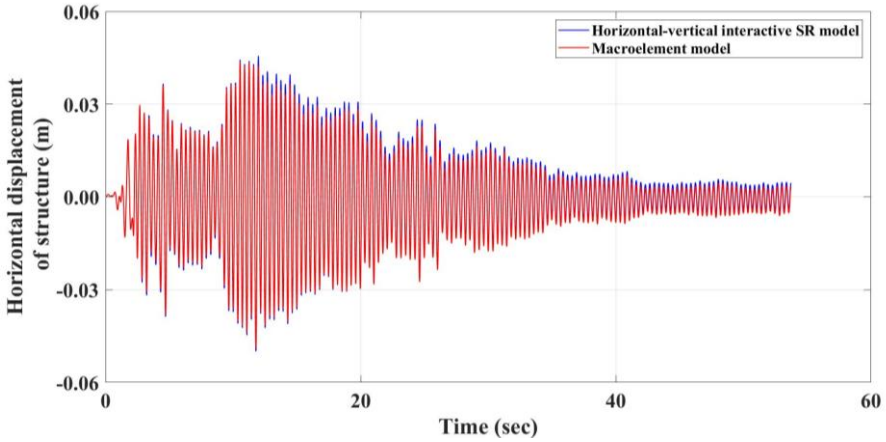

(b) When the structure is sustained on stiff soil.

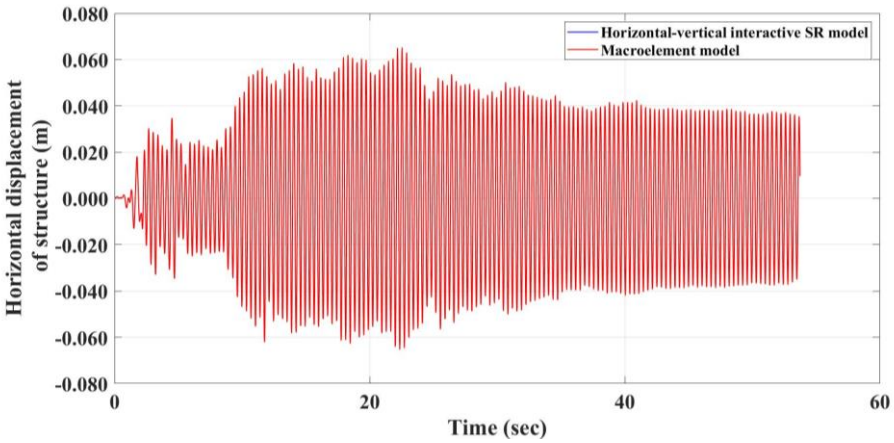

(c) When the structure is sustained on a rock.

Figure 2.15 Structural responses when the five-story building was subjected to the ground motion recorded at El Centro during the 1940 Imperial Valley Earthquake.

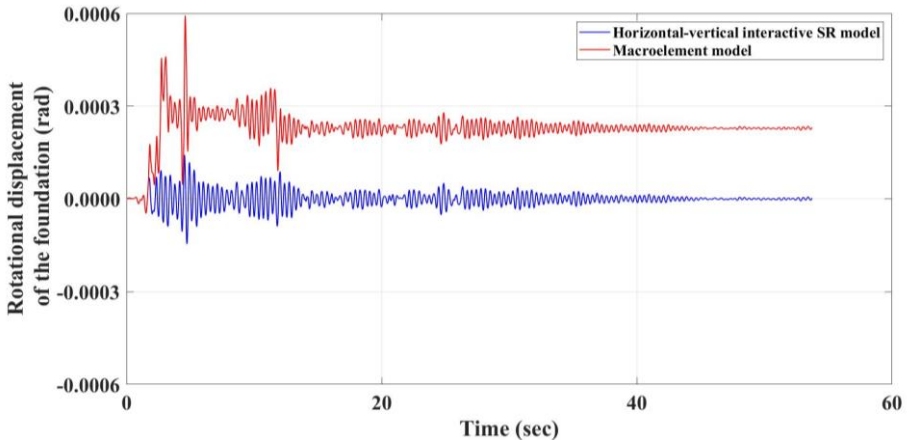

(a) When the structure is sustained on soft soil.

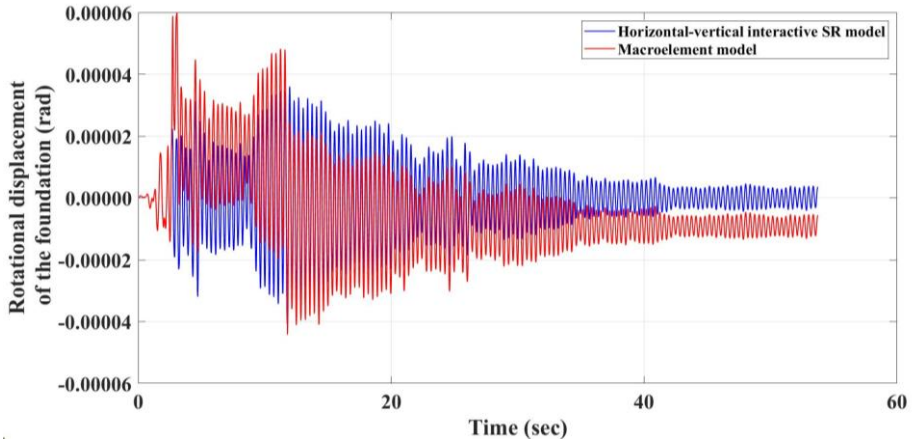

(b) When the structure is sustained on stiff soil.

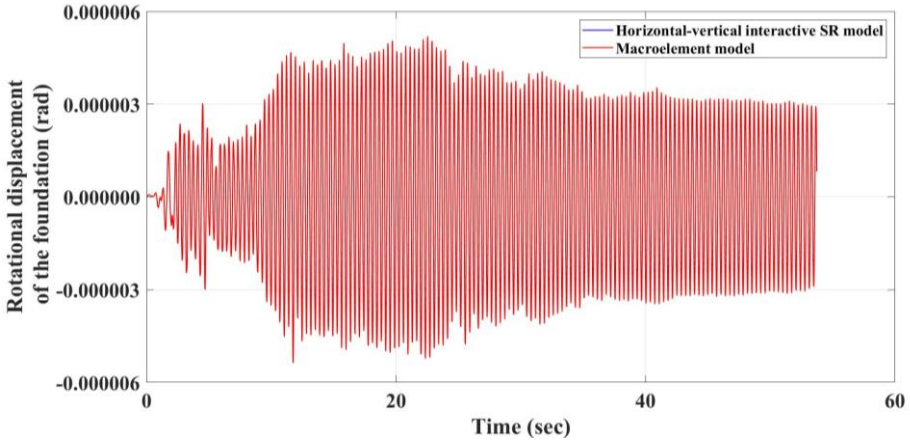

(c) When the structure is sustained on a rock.

Figure 2.16 Rotational displacement of the foundation when the five-story building was subjected to the ground motion recorded at El Centro during the 1940 Imperial Valley Earthquake.

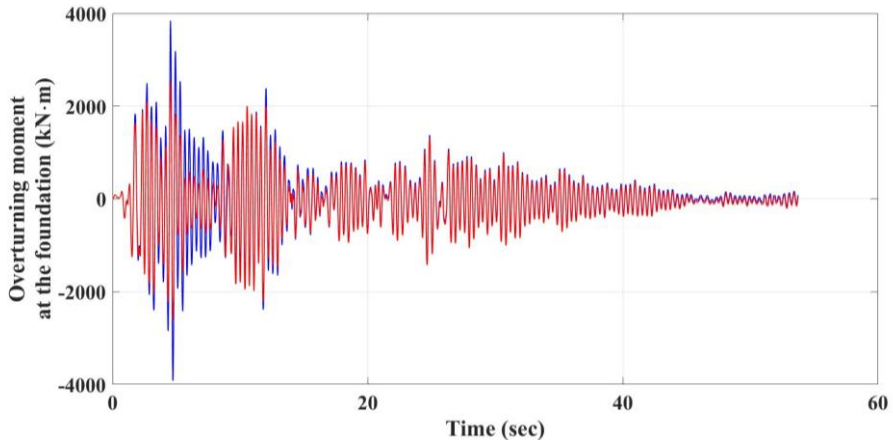

(a) When the structure is sustained on soft soil.

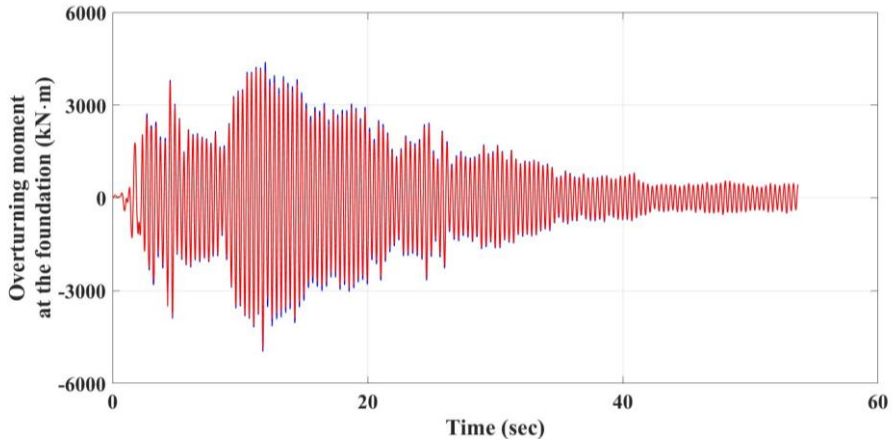

(b) When the structure is sustained on stiff soil.

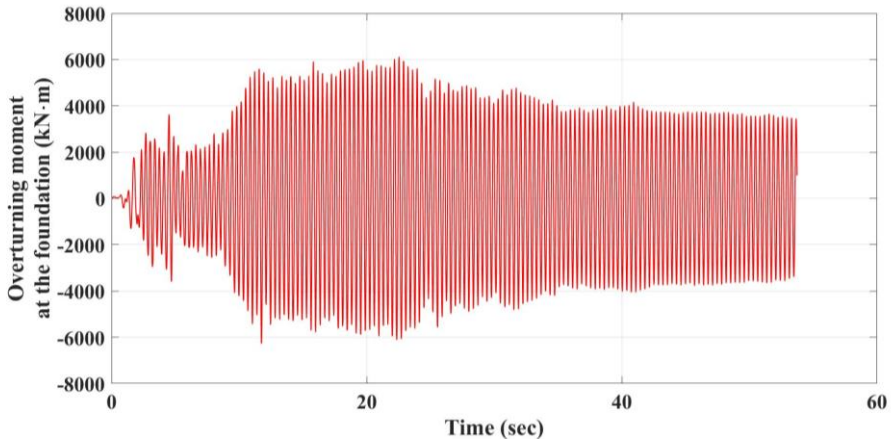

(c) When the structure is sustained on a rock.

Figure 2.17 Overturning moment of the foundation when the five-story building was subjected to the ground motion recorded at El Centro during the 1940 Imperial Valley Earthquake.

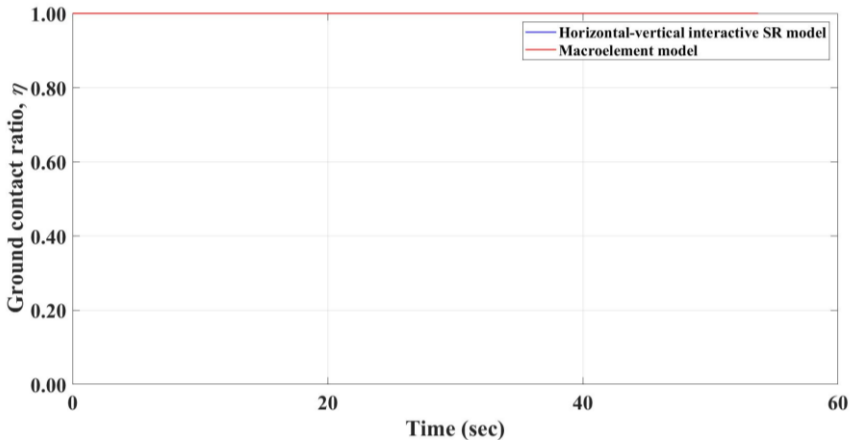

(a) When the structure is sustained on soft soil.

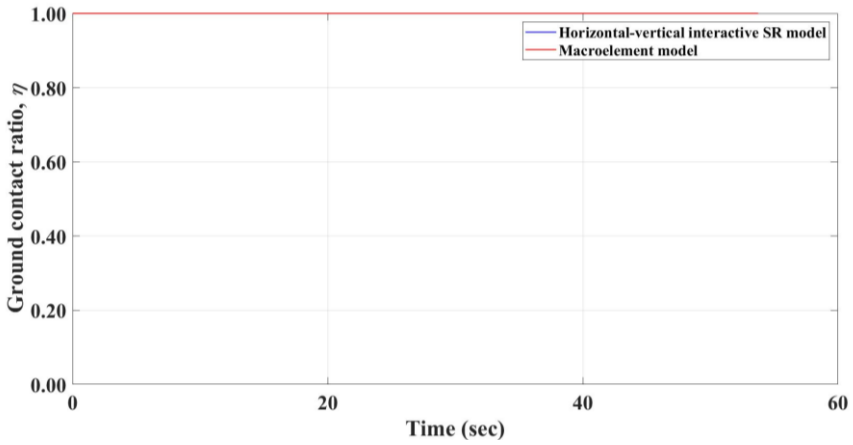

(b) When the structure is sustained on stiff soil.

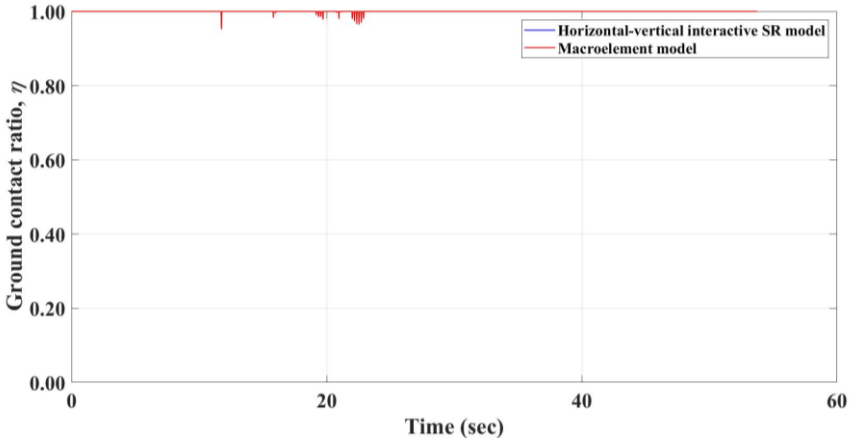

(c) When the structure is sustained on a rock.

Figure 2.18 Ground contact ratio when the five-story building was subjected to the ground motion recorded at El Centro during the 1940 Imperial Valley Earthquake.

To pursue the foundation uplift, the overturning moment of the foundation and the ground contact ratio for both numerical models are compared in Figures 2.17 and 2.18. Figures 2.17(a)–(c) compare the overturning moments of the foundation for the horizontal–vertical interactive SR and macroelement models when the structure is founded on soft soil, stiff soil, and rock, respectively. When the structure is sustained on soft soil, the overturning moment seems to decay compared to that for the structures on stiff soil and a rock, as presented in Figure 2.17(a). Figures 2.18(a)–(c) illustrate the ground contact ratio for the horizontal–vertical interactive SR and macroelement models when the structures are on soft soil, stiff soil, and rock, respectively. The foundation exhibits an uplift, as shown in Figure 2.18(c). Figures 2.19–2.21 compare the relationships between the rotational displacement and the overturning moment at the foundation for both numerical models for the structures on soft soil, stiff soil, and rock, respectively. The relationship between the rotational displacement and the overturning moment at the foundation for the horizontal–vertical interactive SR model of all cases (i.e., structures on soft soil, stiff soil, and rock) is a linear behavior, as presented in Figures 2.19(a), 2.20(a), and 2.21(a), respectively. Although the foundation exhibits an uplift when the structure is sustained in a rock, the relationship between the rotational displacement and the overturning moment remains linear for both numerical models because the foundation slightly uplifts and is still almost in contact with the soil. Figures 2.19(b) and 2.20(b) illustrate that the relationship between the rotational displacement and the overturning moment for the

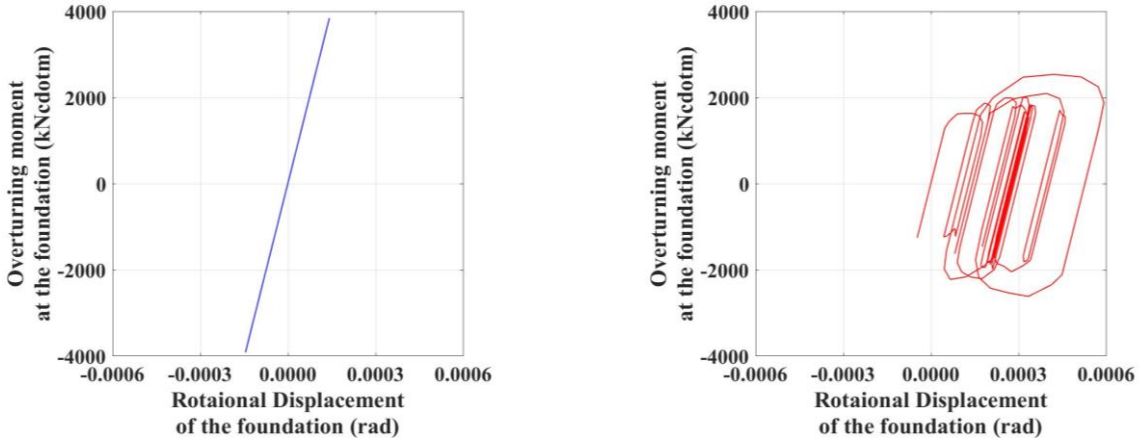

(a) Horizontal–vertical interactive SR model (b) Macroelement model

Figure 2.19 Relationship between the rotational displacement and the overturning moment at the foundation when the five-story building sustained on soft soil was subjected to the recorded ground motion at El Centro during the 1940 Imperial Valley Earthquake during an earthquake.

macroelement model is a nonlinear curve for the soft and stiff soil cases due to the soil nonlinearity.

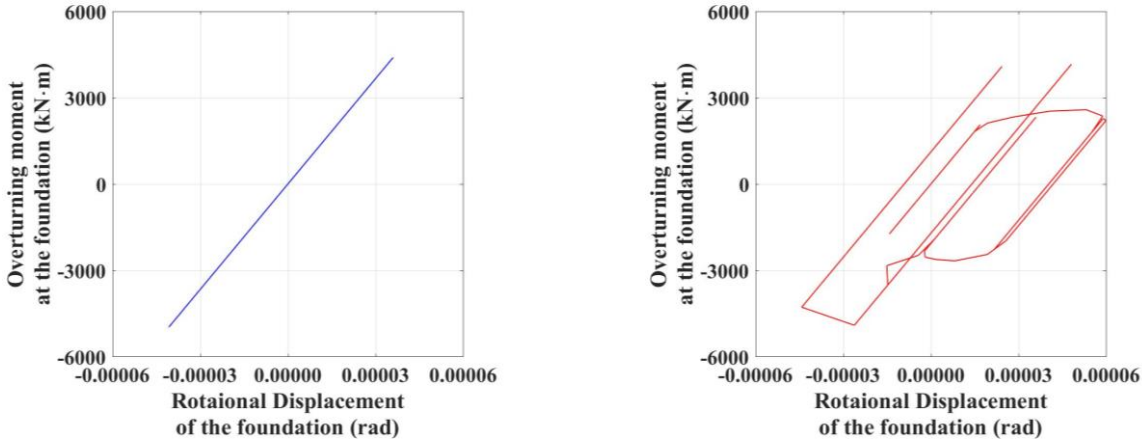

(a) Horizontal–vertical interactive SR model (b) Macroelement model

Figure 2.20 Relationship between the rotational displacement and the overturning moment at the foundation when the five-story building sustained on stiff soil was subjected to the recorded ground motion at El Centro during the 1940 Imperial Valley Earthquake during an earthquake.

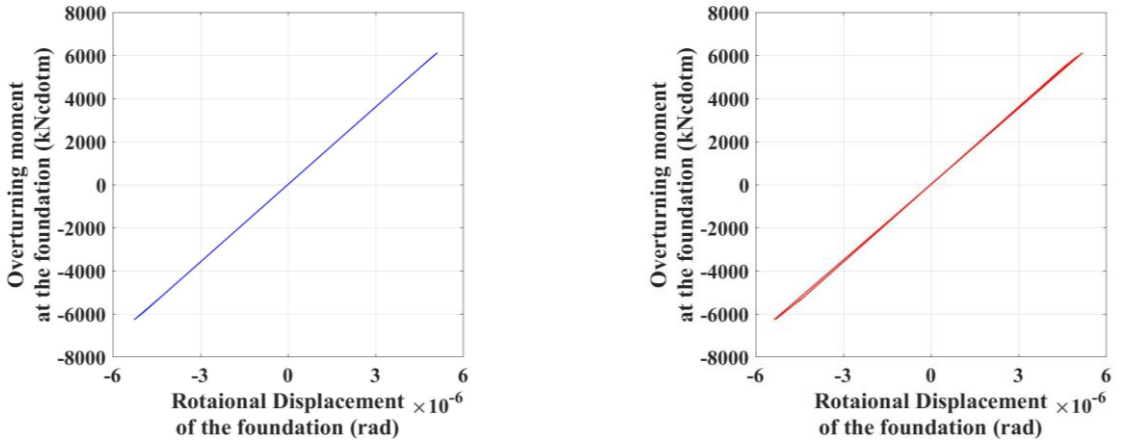

(a) Horizontal–vertical interactive SR model (b) Macroelement model

Figure 2.21 Relationship between the rotational displacement and the overturning moment at the foundation when the five-story building sustained on a rock was subjected to the recorded ground motion at El Centro during the 1940 Imperial Valley Earthquake during an earthquake.

Two analytical models (i.e., low- and medium-rise structures) under three soil conditions are subjected to five selected recorded ground motions with various amplitudes (i.e., PGA or maximum acceleration is adjusted). The results will be discussed in Sections 2.7.1 and 2.7.2 for the low- and medium-rise buildings, respectively, from the following viewpoints:

(1) maximum horizontal structural response;

(2) minimum ground contact ratio; and

(3) rotation angle of the foundation in the plastic and uplift components for the macroelement model to discuss the amount of soil displacement in the plastic deformation.

2.7.1 Comparison responses for the low-rise building cases

Figures 2.22 and 2.23 compare the maximum structural displacements and the minimum ground contact ratios for both numerical models, respectively. Figures 2.22(a)–(c) depict the maximum structural displacement for the low-rise building found on soft soil, stiff soil, and rock, respectively. Figure 2.22(a) illustrates comparatively different values of the maximum structural response for the structure on soft soil. Figures 2.22(b) and (c) show that the maximum value of the structural responses for the horizontal–vertical interactive SR models is almost equivalent to the macroelement model for the structure sustained on stiff soil

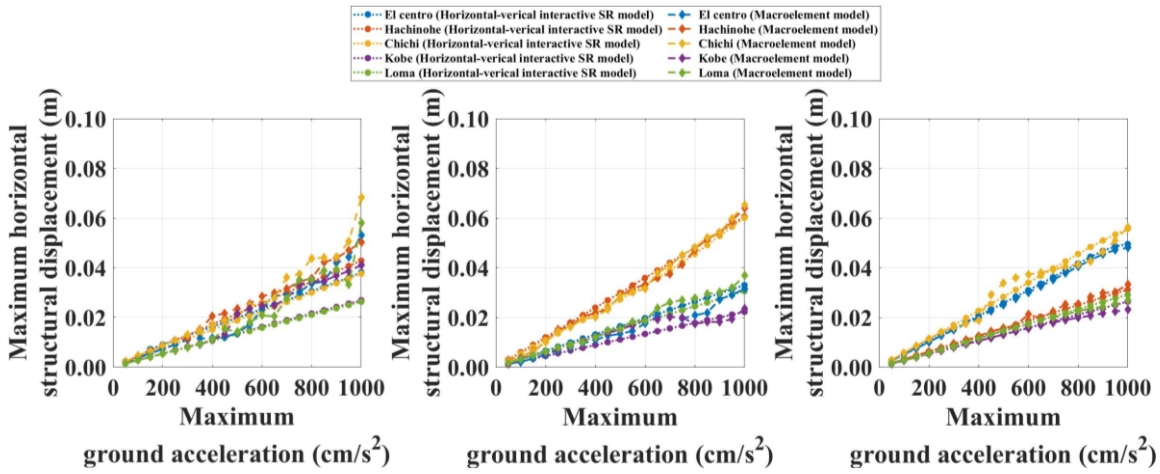

(a) Soft soil (b) Stiff soil (c) Rock

Figure 2.22 Comparison of the maximum horizontal structural responses for the low-rise building

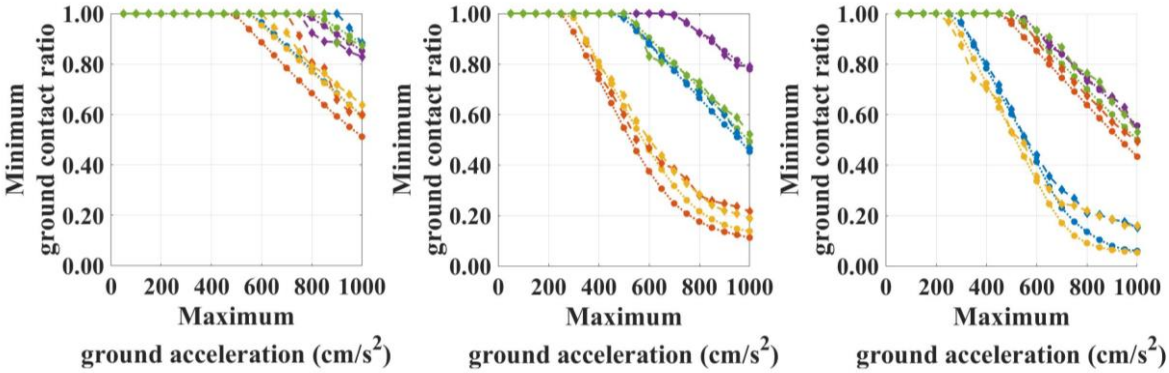

(a) Soft soil (b) Stiff soil (c) Rock

Figure 2.23 Comparison of the minimum ground contact ratios for the low-rise building

and rock. To discuss the foundation uplift behavior, Figures 2.23(a)–(c) compare the minimum values of the ground contact ratio for the low-rise buildings sustained on soft soil, stiff soil, and rock, respectively. Except in some cases, in which the structure is sustained on soft soil, the degree of the ground contact ratio mostly agrees well when the ground contact ratio range is higher than 40%. This might be the result of the soil nonlinearity. Figures 2.24 and 2.25 show the rotational angle ratio in the plastic and uplift components to the total rational angle of the foundation or the macroelement model, respectively, for the structure sustained on soft soil, stiff soil, and rock to discuss the plastic deformation of the soil and the foundation uplift behavior. According to the ground acceleration increase, the total rotational angle of the foundation for the structure on soft soil mostly comprises plastic components, as shown in

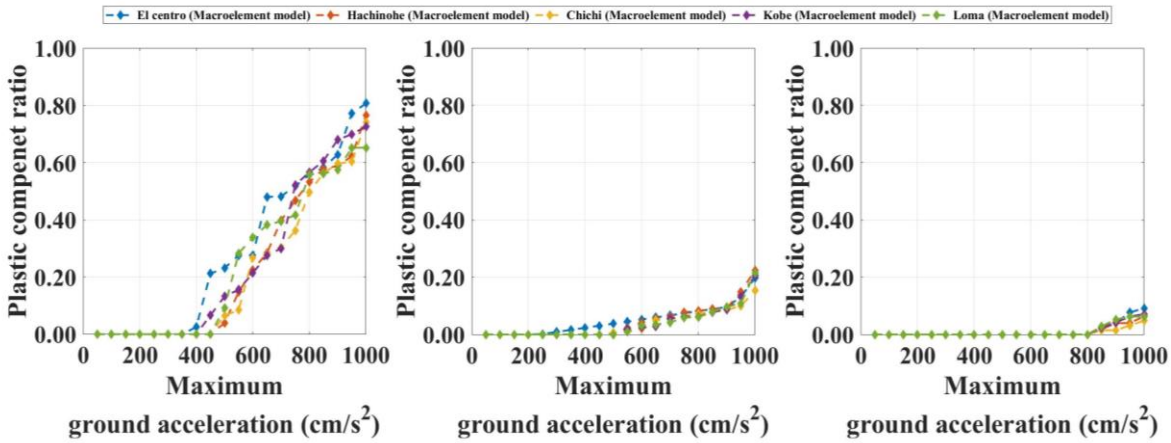

(a) Soft soil (b) Stiff soil (c) Rock

Figure 2.24 Ratio of the rotational angle in the plastic components to the total rational angle of the foundation for the macroelement model of the low-rise building

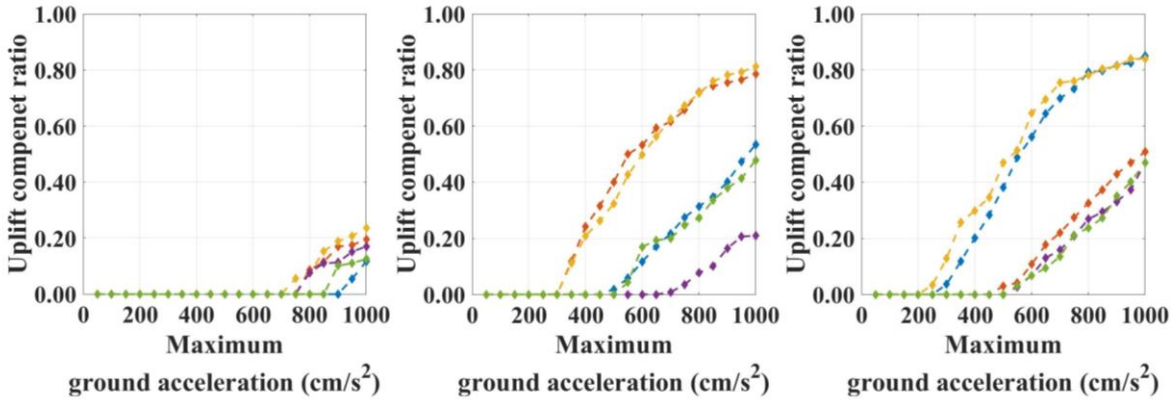

(a) Soft soil (b) Stiff soil (c) Rock

Figure 2.25 Ratio of the rotational angle in the uplift components to the total rational angle of the foundation for the macroelement model of the low-rise building

Figure 2.24(a) corresponding to a high value of the ground contact ratio, as shown in Figure 2.23(a). In contrast, even though the structure sustained on a rock has less rotation in plastic components, most of the deformation comprises uplift components, as indicated in Figures 2.24(c) and 2.25(c), corresponding to a lesser ground contact ratio, as presented in Figure 2.23(c).

2.7.2 Comparison responses for the medium-rise building cases

The maximum structural displacements and the minimum ground contact ratios for the medium-rise structure subjected to various recorded ground motions are compared in Figures 2.26 and 2.27, respectively. Figures 2.26(a)–(c) illustrate the maximum structural displacement

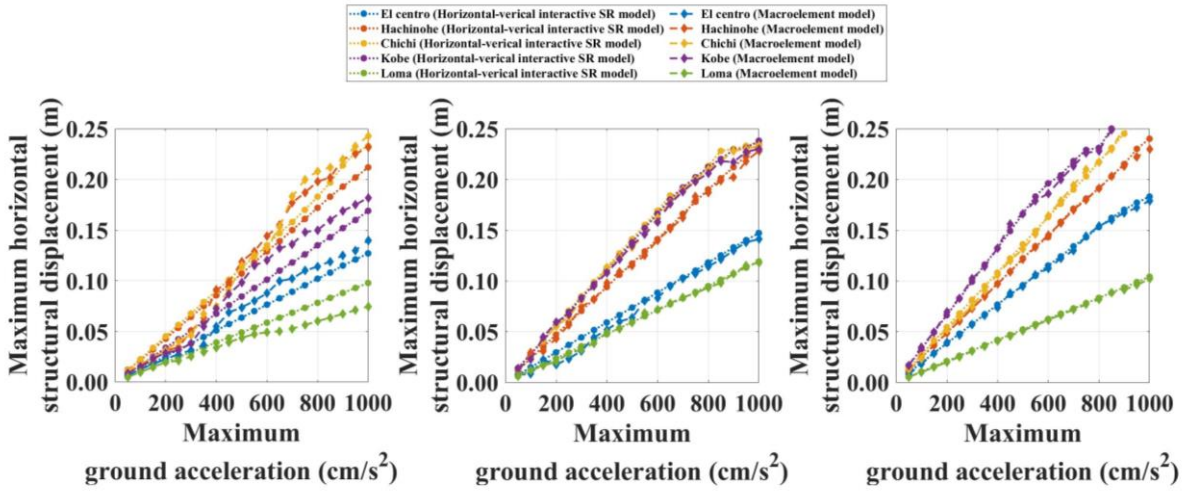

(a) Soft soil (b) Stiff soil (c) Rock

Figure 2.26 Comparison of the maximum horizontal structural responses for the medium-rise building

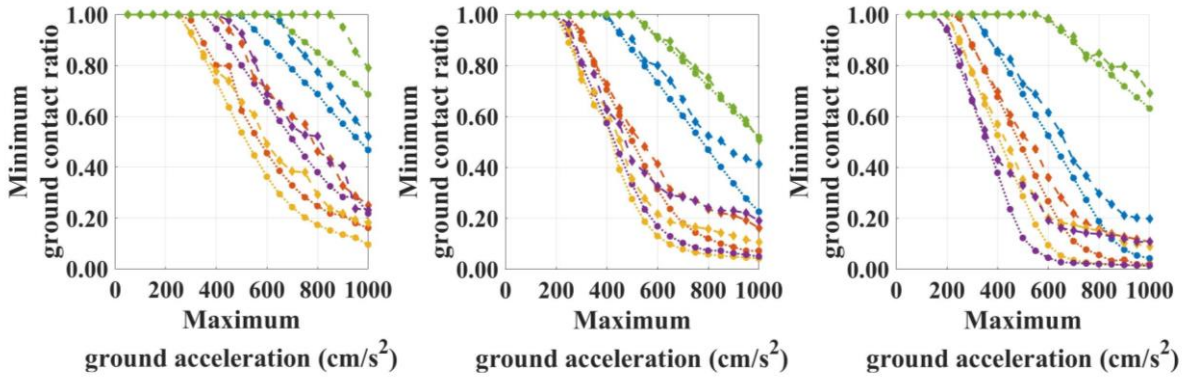

(a) Soft soil (b) Stiff soil (c) Rock

Figure 2.27 Comparison of the minimum ground contact ratios for the medium-rise building

for the medium-rise buildings sustained on soft soil, stiff soil, and rock, respectively. When the medium-rise building is sustained on soft soil, the maximum structural responses for the horizontal–vertical interactive SR models comparatively differ from the macroelement model as the maximum acceleration of the ground input motion increases. In contrast, the maximum value of the structural responses for the horizontal–vertical interactive SR models is almost equivalent to that of the macroelement model when the structures are sustained on stiff soil and rock, as illustrated in Figures 2.26(b) and 2.26(c). Figures 2.27(a)–(c) compare the minimum values of the ground contact ratio for the medium-rise building sustained on soft soil, stiff soil, and rock, respectively. Figure 2.27(a) shows that the structure on soft soil demonstrates relatively different values, even though the ground contact ratio is not low. Meanwhile, the

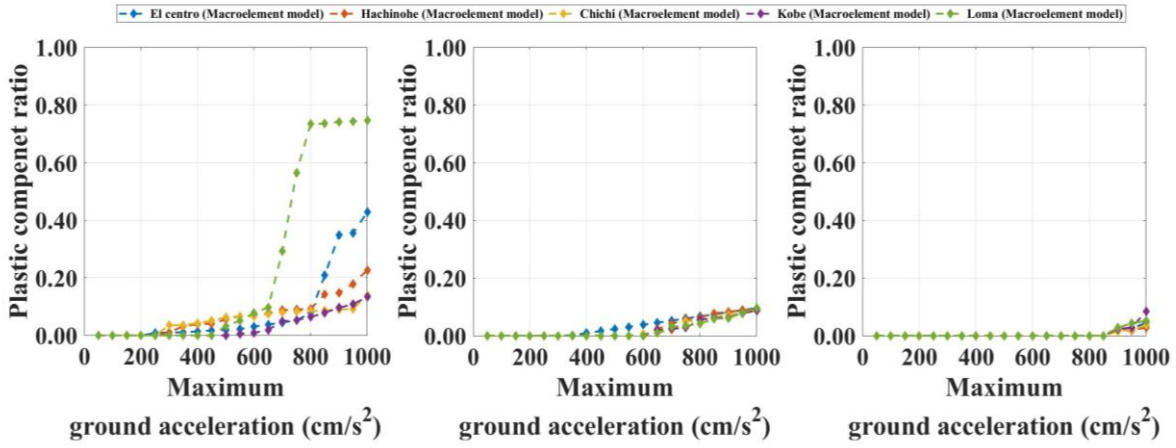

(a) Soft soil (b) Stiff soil (c) Rock

Figure 2.28 Ratio of the rotational angle in the plastic components to the total rational angle of the foundation for the macroelement model of the medium-rise building

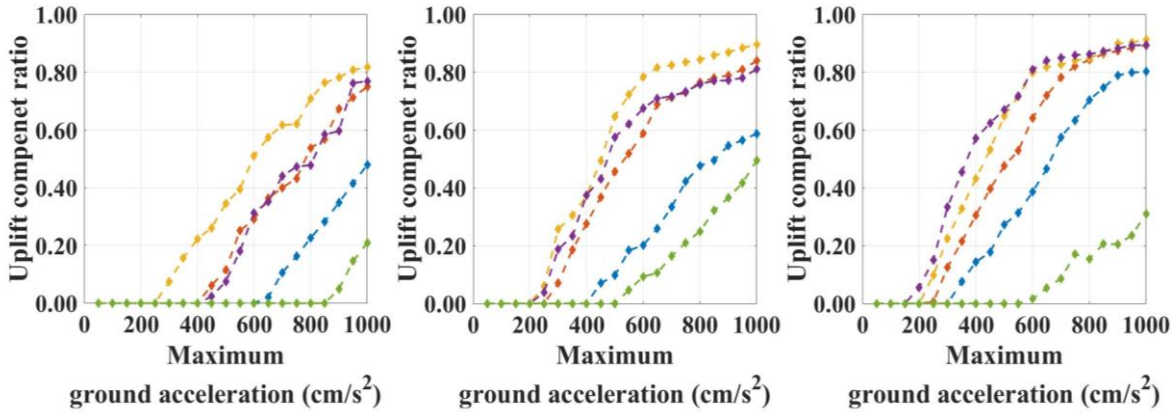

(a) Soft soil (b) Stiff soil (c) Rock

Figure 2.29 Ratio of the rotational angle in the uplift components to the total rational angle of the foundation for the macroelement model of the medium-rise building

ground contact ratio of each case almost agrees well for both numerical models when the ground contact ratio is not less than 40% for the structure sustained on stiff soil or rock, as illustrated in Figures 2.27(b) and 2.27(c). Figures 2.28 and 2.29 display the ratios of the rotational angle in the plastic and uplift components to the total rational angle of the foundation for the macroelement model for the five-story building sustained on soft soil, stiff soil, and rock. Figure 2.28(a) illustrates that the rotational angle in the plastic component for the structure sustained on soft soil is the highest when compared with that sustained on stiff soil and rock. By contrast, less deformation is found in the plastic component when the structure is founded on a rock. Most of this deformation comprises the uplift component, as shown in Figure 2.29(c).

The comparison results show that, although the structures on stiffer soil are safely sustained, the foundation becomes more likely to uplift. However, if foundation uplift become excessive, which is caused by intensive earthquakes and may bring structural instability. The level of the foundation uplift will also vary depending on the intensity of the seismic ground motion input and the dynamic structure characteristics, frequency characteristics of ground input motion, and soil conditions.

2.8 Summary

In summary, Chapter 2 compared two numerical models considering the foundation uplift, that is, the horizontal–vertical interactive sway-rocking model proposed by Tanaka et al. [4] and Momma et al. [5] and the macroelement model proposed by Nakatani et al. [7], to discuss the effect of soil nonlinearity or geometrical nonlinearity on the foundation uplift behavior and structural responses. This objective was achieved by preparing low- and medium-rise buildings with shallow foundations considering the foundation uplift with three different soil conditions. This chapter prepared two different types of ground motions considering inland and subduction-zone earthquakes; hence, five ground motions with different frequency characteristics recorded from major earthquakes were selected for the time history analysis. The conclusions are drawn:

1. Although the ground contact ratios for both models are relatively different, the structural responses of both are relatively similar when the structures are sustained on stiff soil and rock. When the structures are sustained on soft soil, the structural responses of both numerical models are comparatively different due to the soil nonlinearity. Hence, the effect of the soil nonlinearity should be considered when the structures are sustained on soft soil.

2. When structures are sustained on soft soil, the macroelement model may be more suitable for calculating the seismic response considering the foundation uplift because it considers the soil nonlinearity and the foundation uplift. However, structures supported by a mat foundation are generally sustained on stiff soil or rock; therefore, the macroelement and horizontal–vertical interactive SR models are appropriate for calculating the seismic responses considering the foundation uplift.

3. The plastic deformation of soil might reduce the rotational angle in the uplift component, resulting in a higher ground contact ratio level.

4. In contrast, although the plastic component shows less rotation angle when the structure is sustained on a rock, the total rotation angle mostly comprises the rotational angle in the uplift components, which results in becoming more likely to uplift.

5. The degree of the foundation uplift will variously depend on the structure characteristics, seismic input motion characteristics, and soil conditions.

Sometimes, when a structure supported by a shallow foundation is on stiffer soil for a safer sustainment, the foundation becomes more likely to uplift, which may have a positive impact on the dynamic structural response due to the seismic isolation. Nevertheless, if the foundation uplift becomes excessive, the structure may become unstable, which must be avoided.

References

[1] Nakatani, S., Shirato, M. and Kouno, T.: Development of a numerical analysis model to predict seismic behavior of shallow foundations, *Public Works Research Institute Report*, ISSN 0386-5878, No. 4101, 2008 (in Japanese).

[2] Tanaka, H., Moriyama, K. and Watanabe, S.: Study on horizontal – vertical interactive SR model for basemat uplift (Part 1: Formulation of non-linear characteristics of soil), *Transactions of the 13th International Conference on Structure Mechanics in Reactor Technology (SMiRT 13)*, 1995.

[3] Oliveto, G., Caliò, I. and Greco, A.: A large displacement behaviour of a structural model with foundation uplift under impulsive and earthquake excitations, *Earthquake Engineering and Structural Dynamics*, 32, 369-393, 2003.

[4] Fukui, J., Kimura, Y., Ishida, M. and Kishi Y.: An investigation on the response of shallow foundations to large earthquakes, *Technical Memorandum of PWRI*, Public Works Research Institute, 3627, 1999. (in Japanese)

[5] Hayashi, Y.: Damage reduction effect due to basemat uplift of buildings. *Journal of Structural and Construction Engineering*, 485, 53-62, 1996. (in Japanese)

[6] Momma, T., Shirahama, K. and Suzuki, K.: Study on horizontal – vertical intercative SR model for basemat uplift (Part 2: Non-linear response analysis and validation), *Transactions of the 13th International Conference on Structure Mechanics in Reactor Technology (SMiRT 13)*, 1995.

[7] Nakamura, N., Ino, S., Kurimoto, O. and Miake, M., : An estimation method for basemat uplift behavior of nuclear power plant buildings, *Nuclear Engineering and Design 237*, 1275-1287, 2007.

[8] Qin, X., Chen, Y. and Chouw, N.: Effect of uplift and soil nonlinearity on plastic hinge development and induced vibrations in structures, *Advances in Structural Engineering*, 16, 135-147, 2013.

[9] Inoue, T. and Mikami, A.: Investigation of stress reduction effect on structures due to basemat uplift using energy concept, *International Journal of GEOMATE*, 6, 749-756, 2014.

[10] Inoue, T. and Mikami, A.: Study on stress reduction effect of bridge pier due to basemat uplift and soil yielding, *Japanese Geotechnical Journal*, 10, 1-16, 2014. (in Japanese)

[11] Chopra, AK. *Dynamics of Structures*: *Theory and Applications to Earthquake Engineering*. Prentice Hall, Inc.: Englewood Cliffs, New Jersey, 1995.

[12] Nova, R. and Montrasio, L.: Settlements of shallow foundations on sand, *Gèotechnique*, 41, 243-256, 1991.

[13] Montrasio, L. and Nova, R.: Settlements of shallow foundations on sand: geometric effects, *Gèotechnique*, 47, 49-60, 1997.
[14] Georgiadis, M. and Butterfield, R.: Displacement of footing on sand under eccentric and inclined loads, *Canadian Geotechnical Journal*, 25, 199-212. 1988
[15] Paolucci, R.: Simplified evaluation of earthquake-induced permanent displacements of shallow foundations, *Journal of Earthquake Engineering*, 1, 563-579, 1997
[16] Cremer, C., Pecker, A. and Davenne, L.: Cyclic macro-element for soil-structure interaction: material and geometrical non-linearities, *International Journal for Numerical and Analytical methods in Geomechanics*, 25, pp.1257-1284, 2001.
[17] Shirato, M., Paolucci, R., Kouno, T., Nakatani, S., Fukui, J., Nova, R. and di Prisco, C.: Numerical simulation of model tests of pier-shallow foundation systems subjected to earthquake loads using an elasto-uplift-plastic macro element, *Soil and Foundation*, 48, 693-711, 2008.
[18] TDAP III batch version user's guide version 3.09, *ARK Information Systems*, INC, 2017. (in Japanese)
[19] Nuclear standard committee of JEA: Technical regulations for seismic design of nuclear power plants, *Japan Electric Association*, JEAC 4601-2008, 181-186, 2009. (in Japanese)
[20] Nakamura, N., Kasuga, Y., Yabushita, N., Onimura, S., Nakayama, A., Murakami, Y., Ozaki, M. and Nakano, T.: Study on estimation of basemat uplift of PWR reactor building, *Transactions of the 17th International Conference on Structure Mechanics in Reactor Technology (SMiRT 17)*, 2003.
[21] Gazetas, G.: *Foundation Engineering Handbook* (second edition, ed. By Fang, H. Y.), Chapter 15, Van Nostrand Reinhold, 1991.
[22] Nishiyama, I., Okawa, I., Fukuyama, H. and Okuda, Y.: Building damage by the 2011 off the Pacific coast of Tohoku earthquake and coping activities by NILIM and BRI collaborated with the administration, UJNR, 2011.
[23] Suppasri, A., Shuto, N., Imamura, F., Koshimura, S., Mas, E. and Yalciner, A. C.: Lessons learned from the 2011 Great East Japan tsunami: performance of tsunami counter-measures, coastal buildings, and tsunami evacuation in Japan, *Pure and Applied Geophysics*, 170, 993-1018, 2013.
[24] Tokimatsu, K., Ishida, M. and Inoue, S.: Tsunami-induced overturning buildings in Onagawa during the 2011 Tohoku earthquake, *Earthquake Spectra*, 32, 1989-2007, 2016.
[25] Latcharote, P., Suppasri, A., Yamashita, A., Adriano, B., Koshimura, S., Kai, Y. and Imamura, F.: Possible failure mechanism of buildings overturned during the 2011 Great East

Japan Tsunami in the town of Onagawa, *Frontiers in Built Environment. Earthquake Engineering*, 3, 2017.
[26] Osaki, J.: *Architectural Vibration Theory*, Shokoku-sha, 1996. (in Japanese).
[27] Awlla, H. A., Taher, N. R. and Mawlood, Y. I.: Effect of fixed base and soil-structure interaction on dynamic responses of steel structure, *International Journal of Emerging Trends in Engineering Research*, 8, 6298-6305, 2020.
[28] Look, B.G.: *Handbook of geotechnical investigation and design tables*, Taylor & Francis: Abingdon, UK, 2014.
[29] NEHRP, National Earthquake Hazard Reduction Program: Recommended provisions for seismic regulations of new buildings: Part I, Provisions, FEMA 222A, Federal Emergency Management Agency, Washington, D.C., 1994.
[30] ASCE: Minimum design loads and associated criteria for buildings and other structures, ASCE/SEI 7-10, 2010.

3. SEISMIC RESPONSE OF NONLINEAR STRUCTURE SYSTEMS CONSIDERING FOUNDATION UPLIFT

Chapter 2 explained the basics of the soil–structure interaction considering the foundation uplift, numerical models for calculating the seismic responses, and the foundation uplift phenomenon. The superstructure assumptions are, however, based on linear or elastic systems. The structural responses exhibit a nonlinear or inelastic behavior under the ground motion intensity, which must be considered. Therefore, in Chapter 3, the superstructure assumptions are considered herein based on a nonlinear system. Section 3.1 introduces the background of the studies on the nonlinear structures considering the foundation uplift and the study purpose. Section 3.2 presents the nonlinear system used in this chapter by referring to Osaki [1]. Section 3.3 explains the recorded ground motion. Sections 3.4 and 3.5 discuss the computation results from the viewpoints of the structural responses and the energy concept or dissipation, respectively. Lastly, Section 3.6 summarizes this chapter.

3.1 Background and Purpose

As reviewed in Section 1.3, the foundation uplift significantly affects the structural displacement [2] and reduces the base shear of structures [3,4]. Some studies showed that the foundation uplift greatly affects the linear and nonlinear behaviors of superstructures [5,6]. Therefore, structures may suffer from different damages when the foundation uplift is considered. However, when the foundation is separated from the soil, the energy from the soil to the structure may not be high. Hence, investigating the foundation uplift effect may be more interesting when discussed using the energy concept or the energy flow. Only few studies introduced and investigated the foundation uplift effect from the energy viewpoint. For example, Sarrafzadeh et al. [7] performed shake table tests while considering the structure and soil nonlinearities and the foundation uplift to discuss the foundation uplift effect from the energy viewpoint. They concluded that the foundation uplift effect and the soil nonlinearity reduce the kinetic and damping energies of a structure. Inoue and Mikami [8-10] investigated the reduction effect of the sectional force induced in the bridge structure by the foundation uplift. They used the macroelement model to treat the soil–foundation system considering the foundation uplift, emphasizing a structure based on a linear assumption. They concluded that the foundation uplift effect significantly reduced the input energy to the structure and the structure's strain energy. To extend the discussion of Inoue and Mikami [8-10], this chapter also examines the seismic isolation effects caused by the foundation uplift on the building

structure by considering the structural nonlinearity with the trilinear model and using the macroelement model to treat the soil–structure interaction considering the foundation uplift based on the energy concept.

This chapter discusses the effects of seismic isolation caused by the foundation uplift considering both the structure and soil nonlinearities using the energy concept. For this purpose, low- and medium-rise buildings with shallow foundations sustained on stiff soil are prepared. The macroelement model proposed by Nakatani et al. [11] is used here to treat the soil–structure interaction because the model considers the soil nonlinearity and the foundation uplift. Fifteen ground motions with different frequency characteristics recorded from 100 ground motions at the sites are prepared to construct the structure supported by a mat foundation as earthquake loading for the time history analysis. Furthermore, the three different scenarios were taken to discuss the foundation uplift effect: fixed-base case (i.e., the soil–structure interaction is not considered); case of the structure considering the linear soil–structure interaction (without foundation uplift); and case of the nonlinear soil–structure interaction considering the foundation uplift. The computation results are discussed from the following perspective:

(1) different structure characteristics (i.e., fixed-base foundation, structure considering the linear soil–structure interaction (without foundation uplift), and nonlinear soil–structure interaction considering the foundation uplift);

(2) different structure types (i.e., low- and medium-rise buildings);

(3) different frequency characteristics of the ground input motions;

(4) structural responses; and

(5) energy flow.

3.2 Nonlinear Vibration of the Mass System Considering the Foundation Uplift

Chapter 3 considers the structural nonlinearity using a trilinear model following Masing's rules; hence, Section 3.2 will present a brief overview of the nonlinear system. Please refer to Osaki for the details [1].

3.2.1 Governing equation for the nonlinear system

The governing equation of the linear model considering the foundation uplift, namely Equation (2.29), is recalled here.

$$[M]\{\ddot{u}\}+[C]\{\dot{u}\}+[K_S]\{u\}+\{F_{HD}\}=\{P\} \tag{3.1}$$

For a nonlinear system, the mass and damping matrices are assumed constant. The

stiffness matrix that expresses the restoring force characteristic will be changed by displacement and velocity responses. Consequently, the governing equation for the structure nonlinearity system is written as Equation (3.2), where Q is the restoring force for the nonlinear structure system.

$$[M]\{\ddot{u}\}+[C]\{\dot{u}\}+\{Q(\{u\},\{\dot{u}\})\}+\{F_{HD}\}=\{P\} \tag{3.2}$$

3.2.2 Nonlinear restoring force

Figure 3.1(a) shows the restoring force characteristics of the trilinear model. A indicates the concrete cracking load. Point B is assumed to be the yield load of the reinforcing bar or steel frame. The spring constant ratio ranges are k_2/k_1 = 0.2–0.5 and k_3/k_1 = 0.01–0.05. Figure 3.1(b) demonstrates that, when the load is increased or decreased, even for the same displacement (u), the applied and damping forces differ.

3.2.3 Masing's rule

This section describes Masing's law as a method of analytically expressing the restoring force characteristics of a nonlinear system. The definitions of the related terms are clarified in Table 3.1 [1].

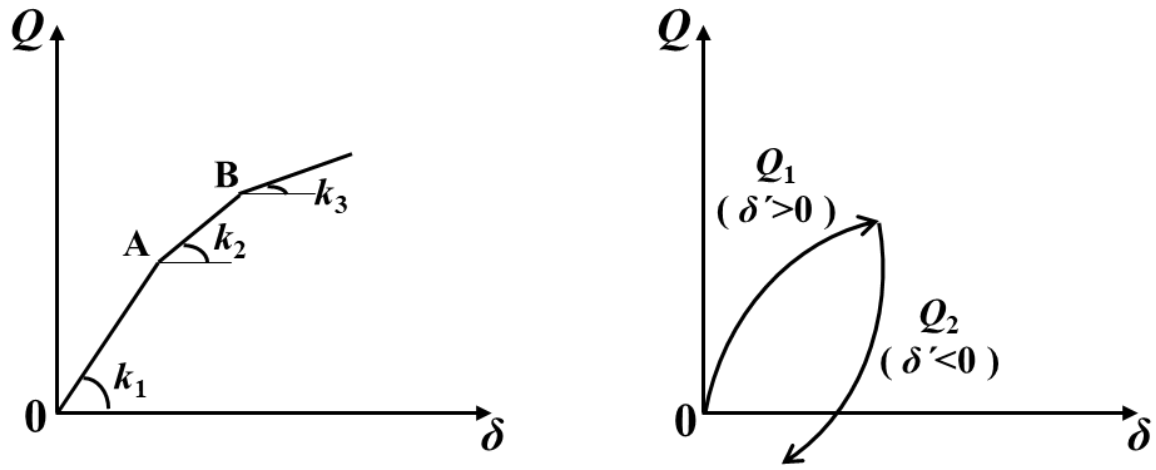

(a) Trilinear model (b) When load is increased or decreased

Figure 3.1 Nonlinear restoring force–deformation curve (referred to Osaki [1])

Table 3.1 Definitions of the related terms for the trilinear model following Masing's rule (referred to Osaki [1])

Terms	Definitions
Force–displacement curve	In the nonlinear case, a curve consists of a skeleton curve and a hysteresis curve.
Turning point	This is the point where the sign of the velocity displacement changes. The velocity displacement at the turning point is zero.
Skeleton curve	When the displacement starts from 0, the restoring force–displacement curve has no turning point, and the displacement monotonically increases or decreases.
Hysteretic curve	Restoring the force–displacement curve after the turning point appears; when the velocity displacement is less and higher than 0, the hysteresis curves are called loading and unloading curves, respectively.
Initial point	This is a turning point where one hysteresis curve is formed. The starting point of the skeletal curve is the origin.
Terminal point	If no new turnaround point occurs, this is the point where the history curve intersects the skeleton curve or the history curve immediately before its initial point
Effective branch	Thi is the portion of the curve between the origin of the skeletal curve and the first turning point or if a new turning point occurs between the initial and terminal points of the history curve, the part of the curve between the starting and turning points.

3.2.3.1 Skeleton curve

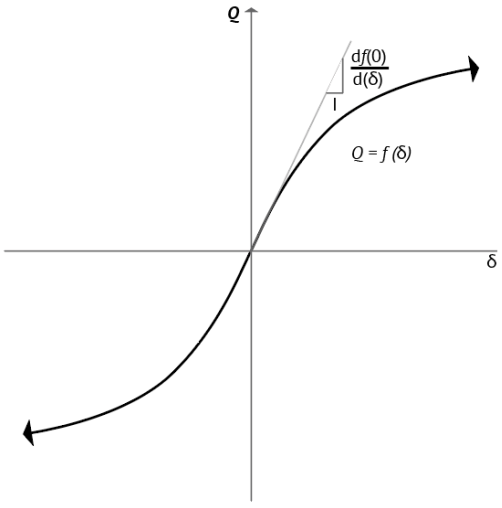

Figure 3.2 Skeleton curve (referred to Osaki [1])

The skeleton curve is expressed as Equation (3.3) and symmetrical with respect to the origin according to its definition (f (0) = 0) and considering that the material is the same for both loading directions [Equation (3.4)].

$$Q = f(\delta) \tag{3.3}$$

$$-f(\delta) = f(\delta) \tag{3.4}$$

Function $f(\delta)$ is considered as the softening type. For the δ_1 and δ_2 combination, the inequality is held, and the function of the softening type and the slope are written as Equations (3.5) and (3.6), respectively. The slope monotonically decreases with the increasing displacement, as illustrated in Figure 3.2.

$$\frac{\mathrm{d}f(\delta_1)}{\mathrm{d}\delta} > \frac{\mathrm{d}f(\delta_2)}{\mathrm{d}\delta} \qquad \delta_1 < \delta_2 \tag{3.5}$$

$$\frac{\mathrm{d}Q}{\mathrm{d}\delta} = \frac{\mathrm{d}f(\delta)}{\mathrm{d}\delta} \tag{3.6}$$

3.2.3.2 Hysteretic curve

The hysteretic curve is expressed as Equation (3.7), where δ_0 and Q_0 denote the initial points. The system expressed by Equations (3.3) and (3.5) is the main point of Masing's rule. The relationship between the restoring force and the displacement in Figure 3.3 indicates that if the skeleton curve is expanded twice in both axes, the hysteretic curve shape is drawn.

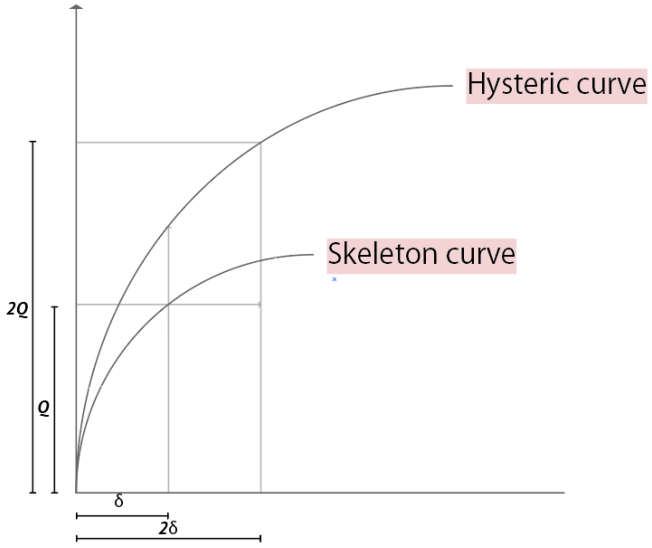

Figure 3.3 Hysteretic curve (referred to Osaki [1])

$$\frac{Q-Q_0}{2} = f\left(\frac{\delta-\delta_0}{2}\right) \tag{3.7}$$

Equation (2.1) is rewritten as Equations (3.8) and (3.9).

$$Q = Q_0 + 2f\left(\frac{\delta-\delta_0}{2}\right) \tag{3.8}$$

$$\frac{\mathrm{d}Q}{\mathrm{d}\delta} = \frac{\mathrm{d}}{\mathrm{d}\delta} f\left(\frac{\delta-\delta_0}{2}\right) \tag{3.9}$$

Therefore, the slope of the initial point of the hysteretic curve is equal to that at the origin of the skeleton curve, as expressed in Equation (3.10).

$$\left(\frac{\mathrm{d}Q}{\mathrm{d}\delta}\right)_{\delta=\delta_0} = \frac{\mathrm{d}f(0)}{\mathrm{d}\delta} \tag{3.10}$$

Figure 3.4 depicts the hysteretic loop shape. When curve AB is a hysteretic curve, and point A is the initial point (δ_0, Q_0), this curve is expressed as Equation (3.7). A new hysteretic curve CD is expressed in Equation (3.11) by supposing that a turning point occurs at point C (δ_1, Q_1) and following Masing's rule.

$$\frac{Q-Q_1}{2} = f\left(\frac{\delta-\delta_1}{2}\right) \tag{3.11}$$

According to Equation (3.4), Equation (3.11) is rewritten as Equations (3.12) and (3.13)

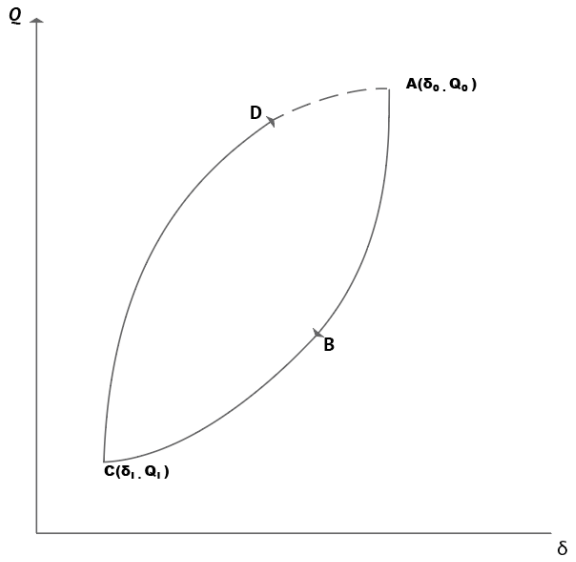

Figure 3.4 Formation loop by the hysteretic curve (referred to Osaki [1])

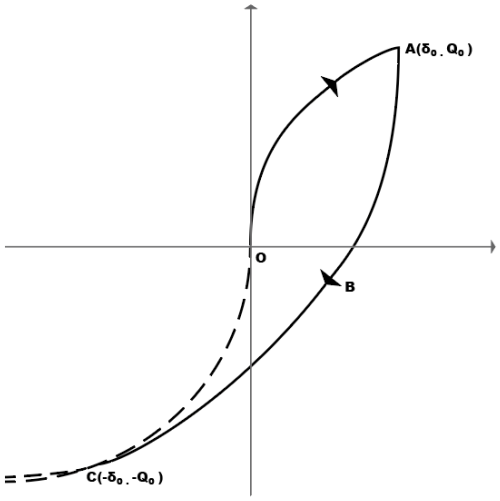

Figure 3.5 Hysteretic curve branched from the skeleton curve (referred to Osaki [1])

by substituting $\delta = \delta_0$ into Equation (3.11).

$$\frac{Q - Q_1}{2} = f\left(\frac{\delta_0 - \delta_1}{2}\right) \tag{3.12}$$

$$\frac{Q - Q_1}{2} = -\left(\frac{Q_1 - Q_0}{2}\right) \tag{3.13}$$

Equation (3.13) indicates that the CD curve passes through Point A and closes the loop, as displayed in Figure 3.4. In other words, the end of a new hysteretic curve is the same as the initial point of the previous hysteretic curve. This relationship must, however, be modified when the previous curve is a skeleton curve, as presented in Figure 3.5.

Assuming that curve AB is a hysteretic curve branched at Point A (δ_0, Q_0) on the skeleton curve, it can be written as Equation (3.14) by following Equations (3.3), (3.4), and (3.7).

$$\frac{Q - Q_0}{2} = f\left(\frac{\delta - \delta_0}{2}\right) \tag{3.14}$$

Equation (3.14) is then rewritten by substituting $\delta = -\delta_0$ into Equation (3.11), as shown in Equation (3.15).

$$\frac{Q - Q_0}{2} = -f(\delta_0) = -Q_0 \tag{3.15}$$

Equation (3.15) indicates that the end point of a hysteretic curve, which starts on a skeleton curve, is the point on a skeleton curve that is symmetrical to the initial point with respect to the origin. Thus, the hysteretic curve shares Point C with the skeleton curve.

3.2.3.3 Hysteretic loop area

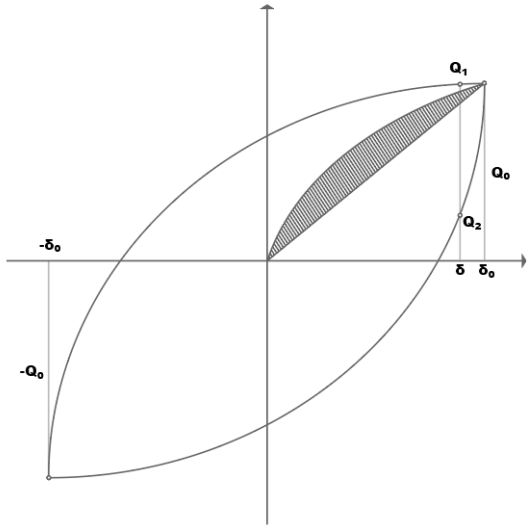

Figure 3.6 Hysteretic loop (referred to Osaki [1])

A close hysteretic loop occurs when displacement cycles are applied between $\pm\delta$ (Figure 3.6). The initial points of the adding and reducing curves are $(-\delta_0, -Q_0)$ and (δ_0, Q_0), respectively. Therefore, the curves are calculated using Equations (3.16) and (3.17), respectively. The loop is computed with Equation (3.18).

$$\frac{Q_1+Q_0}{2}=f\left(\frac{\delta+\delta_0}{2}\right) \tag{3.16}$$

$$\frac{Q_2-Q_0}{2}=f\left(\frac{\delta-\delta_0}{2}\right) \tag{3.17}$$

$$A=\int_{-\delta_0}^{\delta_0}(Q_1-Q_2)\mathrm{d}\delta=2\left[\int_{-\delta_0}^{\delta_0}f\left(\frac{\delta+\delta_0}{2}\right)\mathrm{d}\delta-\int_{-\delta_0}^{\delta_0}f\left(\frac{\delta-\delta_0}{2}\right)\mathrm{d}\delta-2\delta_0Q_0\right] \tag{3.18}$$

The hysteretic loop is rewritten as Equation (3.19), where u and $-u$ are expressed in Equations (3.20) and (3.21), respectively.

$$A=8\left[\int_0^{\delta_0}f(u)\mathrm{d}u-\frac{1}{2}\delta_0Q_0\right] \tag{3.19}$$

$$u=\frac{(\delta+\delta_0)}{2} \tag{3.20}$$

$$-u=\frac{(\delta-\delta_0)}{2} \tag{3.21}$$

Therefore, the enclosed area will be eight times by the skeleton curve and its chord. This relationship is a feature of Masing's model.

3.2.4 Structural nonlinear model

Referring to Osaki [1] and the TDAP III manual [12], the structural stiffness is considered herein using a trilinear model. Figure 3.7(a) illustrates the relationship between the restoring force and the displacement for the low- and medium-rise buildings. Tables 3.2 and 3.3 summarize the parameters defining the restoring force characteristics for the low- and medium-rise buildings.

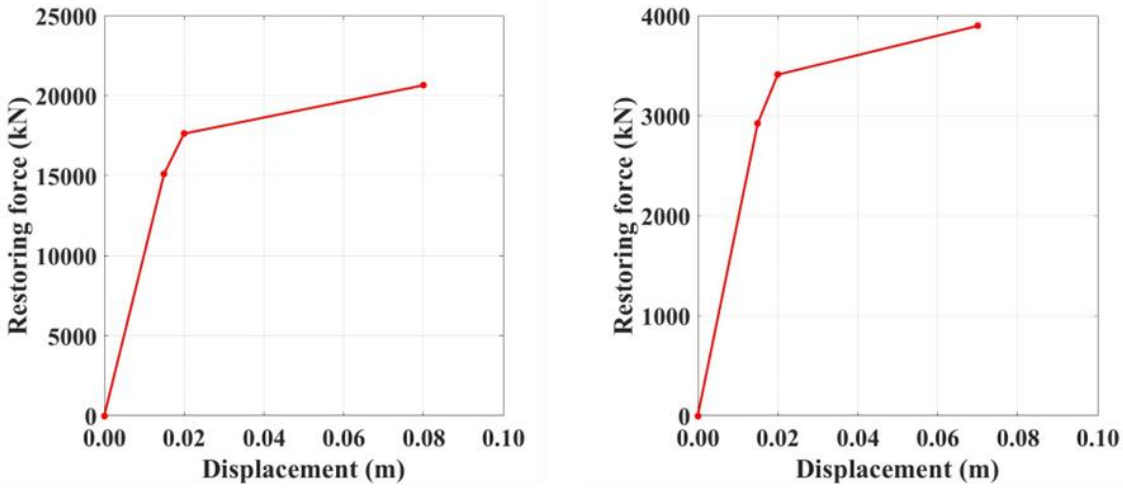

(a) Low-rise building (b) Medium-rise building

Figure 3.7 Trilinear skeleton curve

Table 3.2 Parameters for the restoring force characteristics for the low-rise building

Parameters	Value
First yield point displacement (m)	0.15
Second yield point displacement (m)	0.25
Initial stiffness, k_1 (kN/m)	1.0076×10^6
First stiffness reduction rate	0.5
Second stiffness reduction rate	0.1

Table 3.3 Parameters for the restoring force characteristics for the medium-rise building

Parameters	Value
First yield point displacement (m)	0.15
Second yield point displacement (m)	0.20
Initial stiffness, k_1 (kN/m)	1.9454×10^5
First stiffness reduction rate	0.5
Second stiffness reduction rate	0.1

3.3 Earthquake Ground Motions

Chapter 3 surveyed the 100 recorded ground motions at the sites for construction of the structure supported by a mat foundation (allowable bearing capacity of the soil should be larger 30 kN/m^2 [13]), as illustrated in Figure 3.8. The predominant frequency of each recorded ground motion and the sample ratio are presented in Figure 3.8 (a) and 3.8(b), respectively.

Therefore, Chapter 3 prepares 15 recorded ground motions with different frequency characteristics to discuss the effect of the frequency characteristic of the ground motion by following the sample ratio of the predominant frequency, as illustrated in Figure 3.8(b). However, since this study aims to discuss the effect of the low-frequency characteristic of the ground input motion, this study prepares two recorded ground motions with low-frequency characteristics. Table 3.4 summarizes the selected 15 ground motion properties. These recorded ground motions were selected from the National Research Institute for Earth Science and Disaster Resilience and the Pacific Earthquake Engineering Research Center; hence, the soil information differs. Considering the soil information, Chapter 3 classifies the soil type by the averaged shear-wave velocity to a depth of 30 m (V_{s30}) and the fundamental natural frequency of soil (f_0).

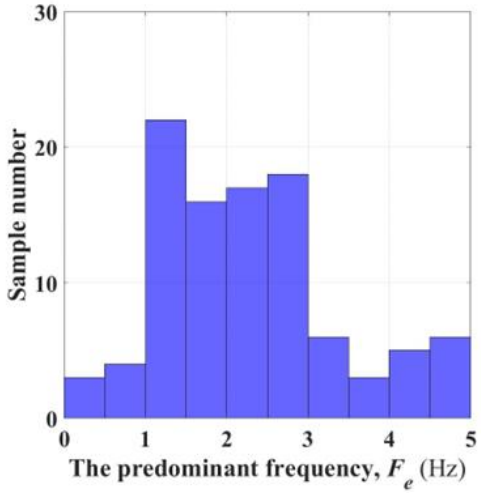

(a) The predominant frequency of 100 ground motions recorded

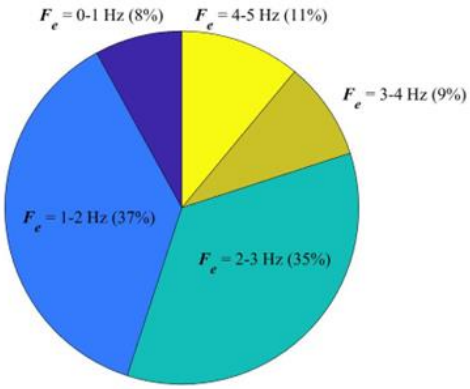

(b) The ratio of the predominant frequency of 100 ground motions recorded

Figure 3.8. The predominant frequency of 100 ground motions recorded at site for construction the structure supported by a mat foundation

Table 3.4 Properties of the selected ground motions

Earthquake (station)	PGA (cm/s^2)	F_e (Hz)	V_{s30} (m/s)	f_0 (Hz)	Site class/type
The 1940 Imperial Valley earthquake (El Centro)	341.695	1.477	213.44	-	D
The 1968 Tokachi-Oki earthquake (Hachinohe Harbor)	231.030	0.378	400.00	-	C
The 1979 Imperial Valley earthquake (El Centro Array #1)	138.299	2.197	237.33		D
The 1989 Loma Prieta earthquake (Anderson Dam (L Abut))	62.917	0.562	488.77	-	C
The 1989 Loma Prieta earthquake (Agnews State Hospital)	165.573	2.783	239.69	-	D
The 1995 Kobe earthquake (HIK)	136.645	1.685	256.00	-	D
The 1995 Kobe earthquake (JMA)	817.544	1.440	312.00	-	D
The 1999 Chi-Chi earthquake (CHY010)	170.791	2.319	538.69	-	C
The 1999 Chi-Chi earthquake (CHY014)	223.924	1.854	347.63	-	D
The 2011 Tohoku earthquake (FKS007)	690.900	4.761	-	8.257	II
The 2011 Tohoku earthquake (FKS011)	311.640	2.966	-	5.551	II
The 2011 Tohoku earthquake (FKS031)	407.680	1.269	-	10.914	II
The 2011 Tohoku earthquake (IWT008)	323.400	3.577	-	18.751	II
The 2011 Tohoku earthquake (IWTH23)	148.960	1.685	-	7.691	II
The 2011 Tohoku earthquake (MYGH03)	133.280	2.002	-	7.783	II

*Site classification: C(soft rock/dense soil), D(stiff soil)

References:

[14] NEHRP, National Earthquake Hazard Reduction Program, Recommended provisions for seismic regulations of new buildings: Part I, Provisions, FEMA 222A, Federal Emergency Management Agency, Washington, D.C., 1994.

[15] ASCE: Minimum Design Loads and Associated Criteria for Buildings and Other Structures, *ASCE/SEI 7-10*, 2010.

*Site classification: Type II(medium), Type III(soft), Type IV(very soft)

References:

[16] Kanai, K., Seismology in Engineering, Tokyo University, Japan, 1983.

[17] Varecha V. P., Fadllan A., and Hartono, H.: Soil classification using horizontal to vertical spectrum ratio methods on Scilab in Sendangmulyo, Semarang, *Physics Education Research Journal,* 4, 71-78, 2022.

3.4 Structural Responses

This section discusses the foundation uplift effect on the structural displacement and acceleration responses. The two analytical models in Section 2.5 are recalled for this discussion. This section, however, focuses on the structures supported by a shallow foundation on stiff soil. Three different scenarios are taken up to discuss the effect of the nonlinear soil–structure interaction considering the foundation uplift: (1) fixed-base case, wherein the effect of the soil–structure interaction is not considered; (2) case of the structure considering the linear soil–structure; and (3) case of the structure considering the nonlinear soil–structure with the foundation uplift.

Figures 3.9 and 3.10 depict the two different structural responses when the five-story (medium-rise) building is subjected to the recorded ground motion during the 1995 Kobe Earthquake, in which the maximum acceleration is adjusted to 50 cm/s^2 representing a small ground motion and 800 cm/s^2 representing a large ground motion. The structural responses for the fixed-base case and the case considering the soil–structure interaction (i.e., linear soil–structure and nonlinear soil–structure interactions considering the foundation uplift) are compared for the small and large ground motions to discuss the foundation uplift effect. Figures 3.9(a) and 3.10(a) show the horizontal displacement of node one (i.e., top of the structure) as two examples of structural responses in the case of 50 and 800 cm/s^2 ground motions, respectively. Figures 3.9(b) and 3.10(b) compare the structural response accelerations in the horizontal direction for the fixed-base case, the case of the structure considering the linear SSI, and the case considering the nonlinear SSI with the foundation uplift. To pursue the foundation uplift phenomenon, Figures 3.9(c) and 3.10(c) present the corresponding rotation angles in the uplift component for the small and large ground motions, respectively. Figures 3.9(a) and (b) and 3.10(a) and (b) show that the structural displacement and acceleration responses for the fixed-base case do not decay as much as that in the case of the structure considering the soil–structure interaction (linear and nonlinear SSI) in both the small and large ground motions, even though the foundation does not exhibit an uplift for the small ground input motion case corresponding to the zero rotation angle in the uplift component, as illustrated in Figure 3.9(c). When the structure is subjected to a comparatively intensive ground motion, the structure response exhibits a nonlinear interaction, and the foundation exhibits a noticeable uplift, as illustrated in Figure 3.10. In Figure 3.10(b), the structural acceleration response for the case considering the foundation uplift is less than that for the fixed-base and linear SSI cases. In conclusion, the foundation uplift may work as a seismic isolation, resulting in the cutting-off of the seismic input motion.

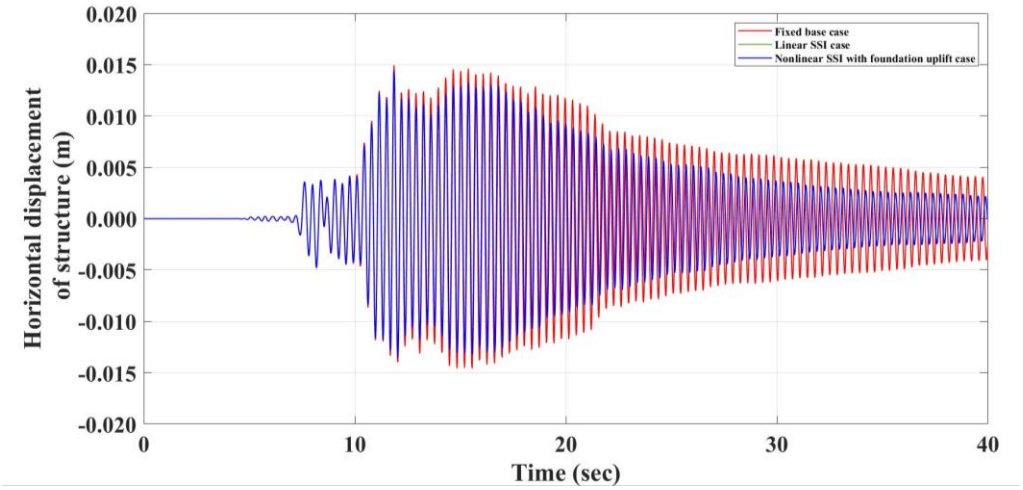

(a) Structural horizontal displacement response

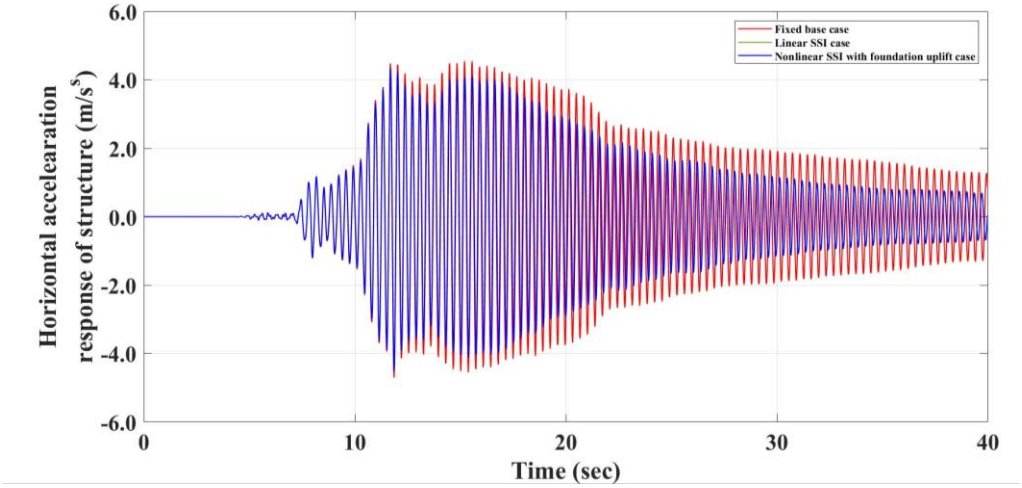

(b) Structural horizontal acceleration response

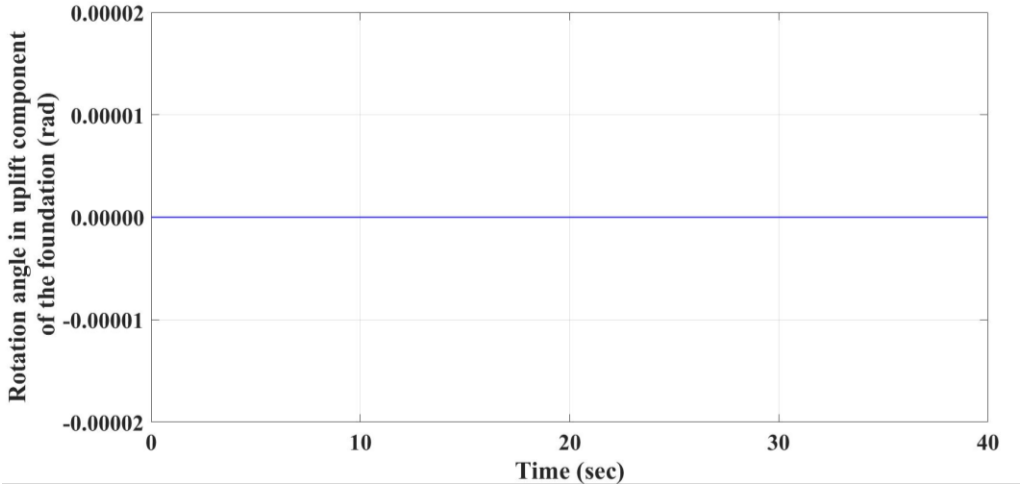

(c) Rotational angle in the uplift component

Figure 3.9 Response when the five-story building is subjected to the 50 cm/s^2 ground motion.

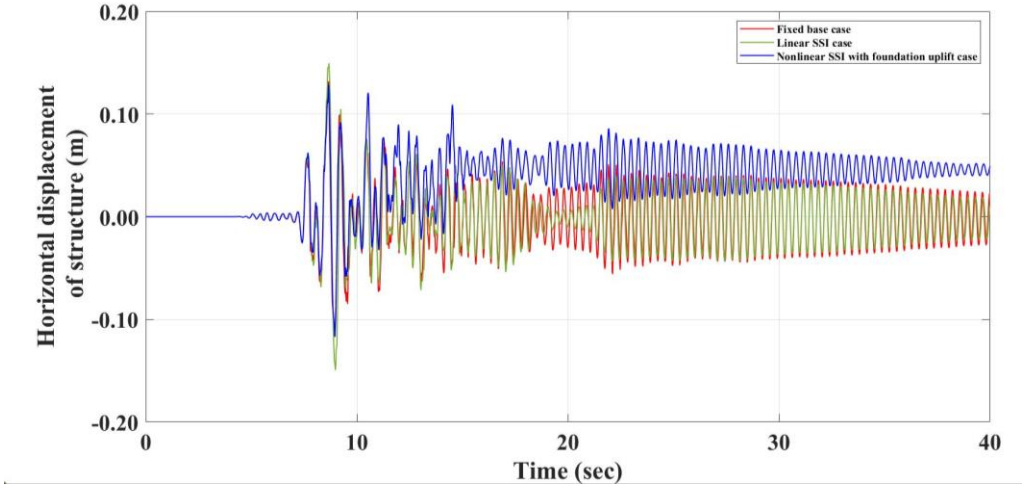

(a) Structural horizontal displacement response

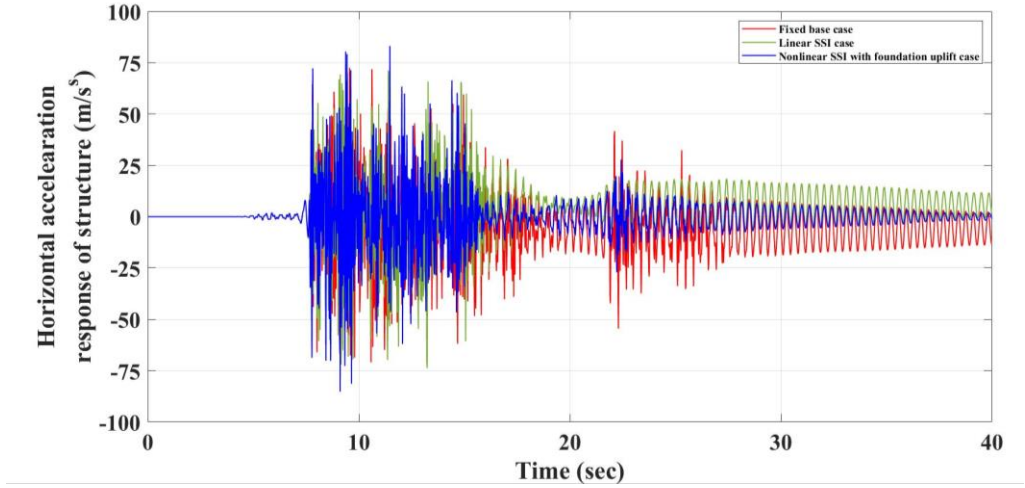

(b) Structural horizontal acceleration response

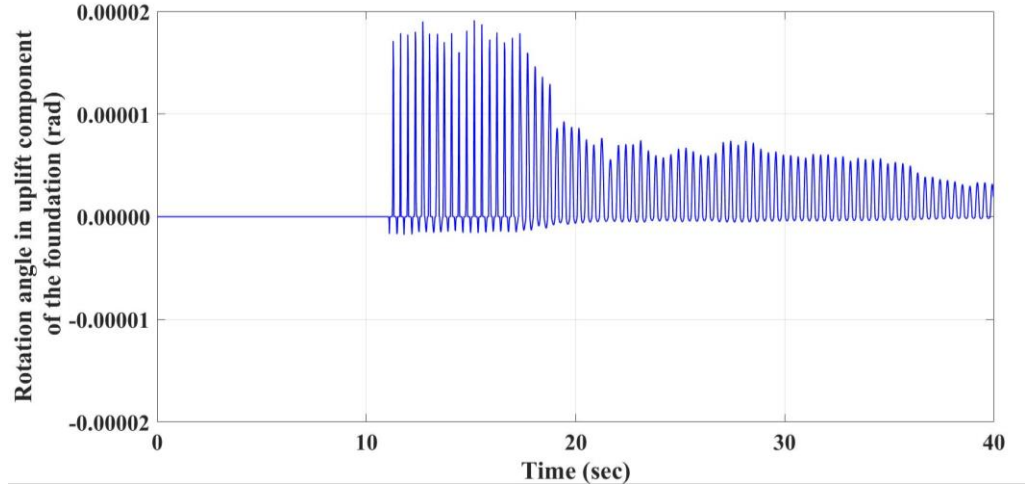

(c) Rotation angle in uplift component

Figure 3.10 Response when the five-story building is subjected to the 800 cm/s^2 ground motion.

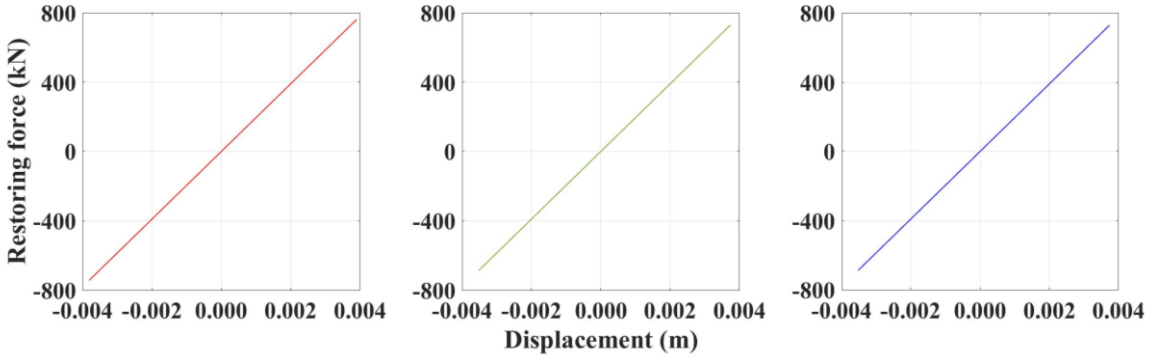

(a) Fixed-base case (b) Linear SSI case (c) Foundation uplift case

Figure 3.11 Restoring the force–displacement curve when the five-story building is subjected to the 50 cm/s^2 ground motion.

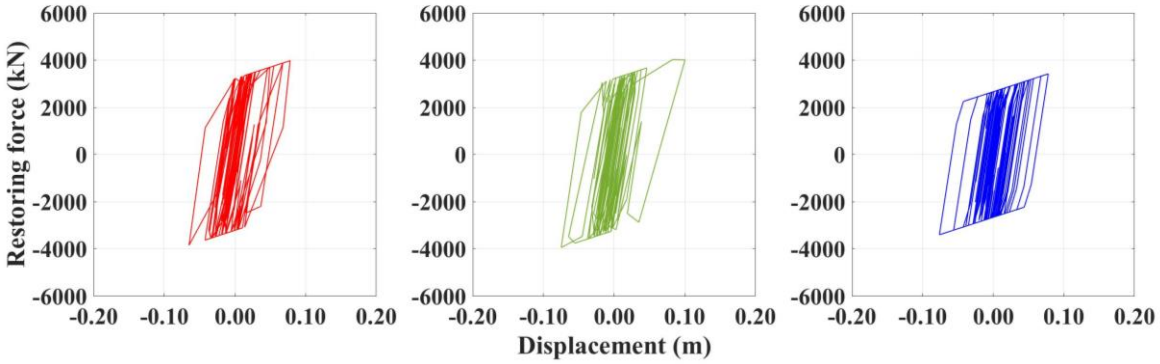

(a) Fixed-base case (b) Linear SSI case (c) Foundation uplift case

Figure 3.12 Restoring the force–displacement curve when the five-story building is subjected to the 800 cm/s^2 ground motion.

Figures 3.11 and 3.12 demonstrate the restoring force and displacement relationship for the small and large ground input motions, respectively. The restoring force and displacement relationship is linear for all three cases, as displayed in Figure 3.11. However, when the structure is subjected to a large ground motion, a remarkable hysteresis loop is drawn for all cases, as shown in Figure 3.12.

To discuss the universality of the effect of the nonlinear soil–structure interaction considering the foundation uplift, the structures with a fixed base and considering the soil–structure interaction are subjected to fifteen recorded ground motions with various amplitudes (i.e., PGA or maximum acceleration is adjusted). The results are compared and discussed in subsequent sections.

3.3.1 Low-rise building

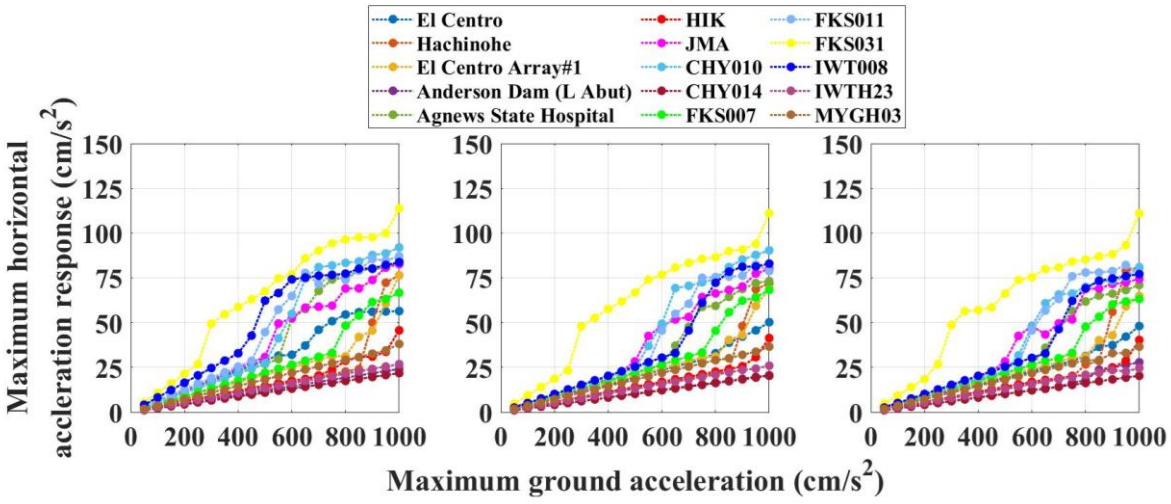

(a) Fixed-base case (b) Linear SSI case (c) Foundation uplift case

Figure 3.13 Maximum acceleration response of the low-rise building when subjected to various ground motions.

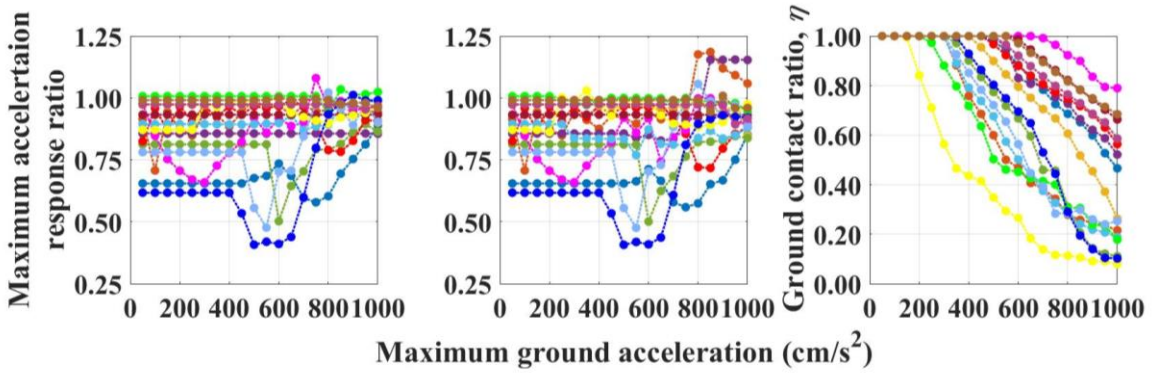

(a) Ratio of the linear SSI fixed-base case (b) Ratio of the nonlinear SSI to the fixed base case (c) Minimum ground to contact ratio

Figure 3.14 Comparison of the responses of the low-rise building when subjected to various ground motions.

Figures 3.13(a)–(c) illustrate the maximum structural acceleration responses for the fixed-base, structure considering the linear SSI, and structure considering the nonlinear SSI with the foundation uplift cases, respectively, when the low-rise building sustained on stiff soil is subjected to the fifteen recorded ground motions with various amplitudes. The maximum structural acceleration for the fixed-base case increased more than those for the cases of the structure considering the SSI (i.e., linear and nonlinear SSI considering the foundation uplift), as shown in Figure 3.13, except when the structure is subjected to the ground motion recorded

at the Hachinohe Harbor station during the 1968 Tokachi–Oki Earthquake. Figures 3.14(a) and (b) illustrate the ratios of the maximum structural acceleration response of the cases considering the linear SSI to the structural acceleration response for the fixed-base foundation case and the nonlinear SSI with the foundation uplift to the structural acceleration response for the fixed-base foundation case, respectively, to more evidently compare the effects of the soil–structure interaction. Most ratios indicate that the acceleration responses for the structure considering the soil–structure interaction, especially with the foundation uplift, tend to be less than those for the fixed base. This indicates that the horizontal structural response is reduced in most cases by the effect of the soil–structure interaction, especially the nonlinear SSI considering the foundation uplift corresponding to the ground contact ratio, as shown in Figure 3.14(c).

3.3.2 Medium-rise building

Figure 3.15 presents the maximum structural response acceleration for the cases of the fixed base, linear SSI, and nonlinear SSI considering the foundation uplift when the medium-rise building sustained on stiff soil is subject to 15 selected recorded ground motions with various amplitudes. Figure 3.15 shows that the maximum structural acceleration responses for the cases considering the soil–structure interaction (i.e., linear and nonlinear SSI with the foundation uplift) moderately increase compared to those in the fixed-base case, except when the structure is subjected to the ground motion with a low predominant frequency (i.e., the ground motions recorded at the Hachinohe Harbor station during the 1968 Tokachi–Oki Earthquake. Figures 3.16(a) and (b) present the maximum ratios of the structural acceleration responses for the cases considering the linear SSI and SSI with the foundation uplift to the structural acceleration response of the fixed-base case. The ratio indicates that the maximum acceleration response for the fixed-base case tends to be larger than that for the cases of the structure considering the soil–structure interaction (i.e., linear and nonlinear SSI with the foundation uplift), as illustrated in Figure 3.16(a) and (b). This indicates that the horizontal response is reduced in most cases due to the increasing foundation uplift corresponding to the ground contact ratio as shown in Figure 3.16(c). When the structure is subjected to the recorded ground motion at the Agnews State Hospital station during the 1989 Loma Prieta Earthquake, the maximum acceleration response for the linear SSI becomes larger than that for the cases with the fixed base and a nonlinear SSI with the foundation uplift because the predominant frequency of the ground motion recorded at the Agnews State Hospital station during this event is close to the natural frequency of the linear SSI system; hence, the structure becomes close to

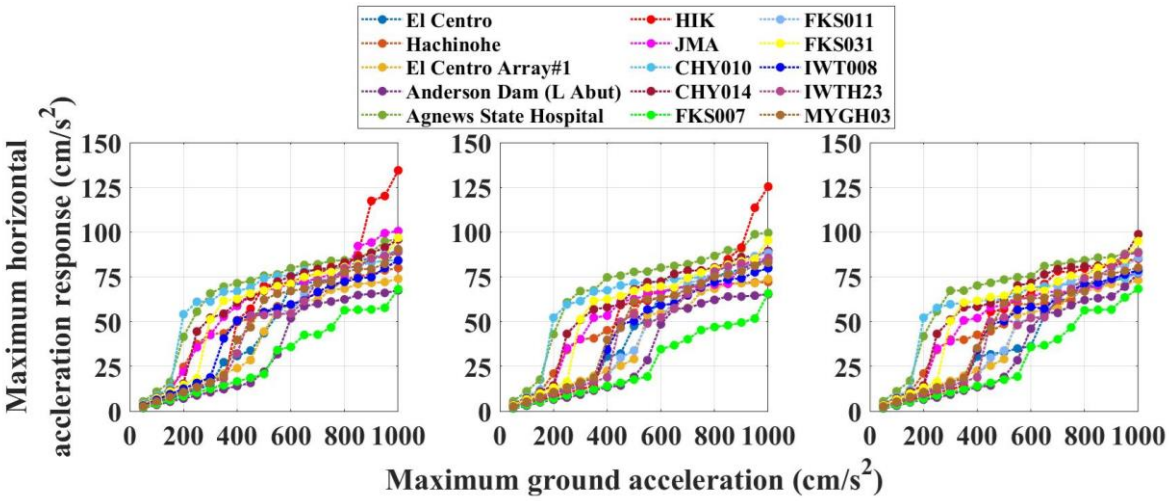

(a) Fixed-base case (b) Linear SSI case (c) Foundation uplift case

Figure 3.15 Maximum acceleration response of the medium-rise building when subjected to various ground motions.

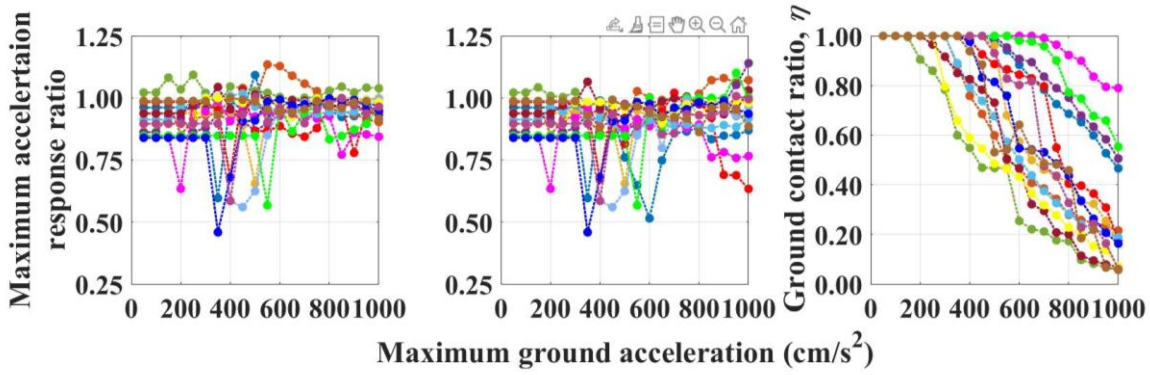

(a) Ratio of the linear SSI to fixed-base case (b) Ratio of the nonlinear SSI to the fixed base case (c) Minimum ground contact ratio

Figure 3.16 Comparison of the responses of the medium-rise building when subjected to various ground motions.

the resonance state. In conclusion, the reduction effect of the reduction degree depends on the structure and frequency characteristics of the ground input motion.

3.5 Energy flow

Referring to Chopra [18] and Akiyama [19], various energy terms can be calculated by integrating the equation of motion. Therefore, the energy balance equation for the nonlinear

system considering the foundation uplift, namely Equation (3.2), is expressed in Equation (3.22).

$$\begin{aligned}&\int_0^t \{\dot{u}\}^T [M]\{\ddot{u}\}\,dt + \int_0^t \{\dot{u}\}^T [C_S]\{\dot{u}\}\,dt + \int_0^t \{\dot{u}\}^T \{Q\}\,dt \\ &+ \int_0^t \{\dot{u}\}^T [C_F]\{\dot{u}\}\,dt + \int_0^t \{\dot{u}\}^T \{F_{HD}\}\,dt = \int_0^t \{\dot{u}\}^T \{P\}\,dt\end{aligned} \tag{3.22}$$

The right side of the energy balance equation of Equation (3.22) is the energy input to the structure (E_I). When a structure is subjected to an earthquake ground motion, the energy input to the structure is written as Equation (3.23), where $\{\ddot{u}_g\}$ is the ground acceleration vector.

$$E_I = -\int_0^t \{\dot{u}\}^T [M]\{\ddot{u}_g\}\,dt \tag{3.23}$$

The first term of the left side of the energy balance equation of Equation (3.22) is the kinetic energy (E_K) of the lumped mass due to its motion relative to the ground, as presented in Equation (2.44).

$$E_K = \int_0^t \{\dot{u}\}^T [M]\{\ddot{u}\}\,dt \tag{3.24}$$

The second term of Equation (3.22) is the dissipation energy caused by structural damping (E_D) expressed in Equation (3.25).

$$E_D = \int_0^t \{\dot{u}\}^T [C_S]\{\dot{u}\}\,dt \tag{3.25}$$

The third term of Equation (3.22) is the absorbed energy since the nonlinear structural stiffness (E_{ASK}) written in Equation (3.26), where $\{Q\}$ is the restoring force vector. The absorbed energy comprises the recoverable elastic strain energy (E_{SK}) and the irrecoverable hysteretic energy (i.e., E_{IRK}, energy dissipated by yielding) expressed in Equation (3.27). The recoverable elastic strain energy (E_{SK}) is calculated using Equation (3.28), where $[K_{S0}]$ is the initial stiffness matrix of a structure. Therefore, the irrecoverable hysteretic energy (E_{IRK}) can be computed using Equation (3.29).

$$E_{ASK} = \int_0^t \{\dot{u}\}^T \{Q\}\,dt \tag{3.26}$$

$$E_{ASK} = E_{SK} + E_{HSK} \tag{3.27}$$

$$E_{SK} = \int_0^t \{\dot{u}\}^T [K_{S0}]\{u\}\,dt \tag{3.28}$$

$$E_{IRK} = E_{ASK} - E_{SK} \tag{3.29}$$

The fourth term of Equation (3.22) is the absorbed energy caused by the damping of the soil–foundation system (E_{RD}) calculated by Equation (3.30), where $\{\dot{u}_F\}$ is the velocity response of the foundation, and $[C_F]$ is the damping matrix of the damping of the soil–foundation system.

$$E_{RD} = \int_0^t \{\dot{u}_F\}^T [C_F] \{\dot{u}_F\} \, dt \tag{3.30}$$

The fifth term of Equation (3.22) is the strain energy of the foundation (E_{HD}) written in Equation (3.31), where $\{F_{HD}\}$ is the horizontal force, vertical force, and overturning moment at the base of the foundation (Section 2.2).

$$E_{HD} = \int_0^t \{\dot{u}_F\}^T \{F_{HD}\} \, dt \tag{3.31}$$

Accordingly, the energy balance equation is rewritten as Equation (3.32).

$$E_K + E_D + E_{ASK} + E_{HD} + E_{RD} = E_I \tag{3.32}$$

Chapter 3 prepares two scenarios to compare and discuss the effects of the soil–structure interaction considering the foundation uplift; thus, the energy balance equation for the fixed-base case considering the structure nonlinearity (i.e., neglecting the effect of the soil-structure interaction) is written as Equations (3.33) and (3.34) by integrating the governing equation for the fixed-base case with reference to Chopra [13] and Akiyama [14].

$$\int_0^t \{\dot{u}\}^T [M] \{\ddot{u}\} \, dt + \int_0^t \{\dot{u}\}^T [C_S] \{\dot{u}\} \, dt + \int_0^t \{\dot{u}\}^T \{Q\} \, dt = \int_0^t \{\dot{u}\}^T \{P\} \, dt \tag{3.33}$$

$$E_K + E_D + E_{ASK} = E_I \tag{3.34}$$

Recall that the structure responses are presented in Figures 3.09 and 3.10 in Section 3.3. Figures 3.17 and 3.18 illustrate the energy variation with time for the structure subjected to the recorded ground motion during the 1995 Kobe Earthquake, in which the maximum acceleration was adjusted to 50 and 800 cm/s^2. Figures 3.17(a)–(c) compare the energy time variations for the cases of the fixed-base structure, structure with the linear soil–structure interaction, and structure with the nonlinear soil–structure interaction considering the foundation uplift, respectively, when the structure is subjected to 50 cm/s^2 ground input motion. The foundation uplift does not occur when the structure is subjected to a comparatively small ground motion, as illustrated in Figure 3.9(c); hence, the energy for case of the structure with the linear SSI seems equivalent to that for the structure with the nonlinear SSI considering the foundation

uplift. The comparison results indicate that the energy input to the structure considering the linear soil–structure interaction cases is less than that for the structure in the fixed-base case. Consequently, the reduction in the kinetic and strain energies of the structure and the dissipated energy caused by structure damping is demonstrated, implying smaller structural velocity responses caused by the reduction effect of the soil–structure interaction. Figure 3.11 shows that a remarkable hysteresis loop in the restoring force and displacement relationship does not occur in both cases when the structures are subjected to the small ground motion, implying the absence of irrecoverable hysteretic energy (E_{IRK}).

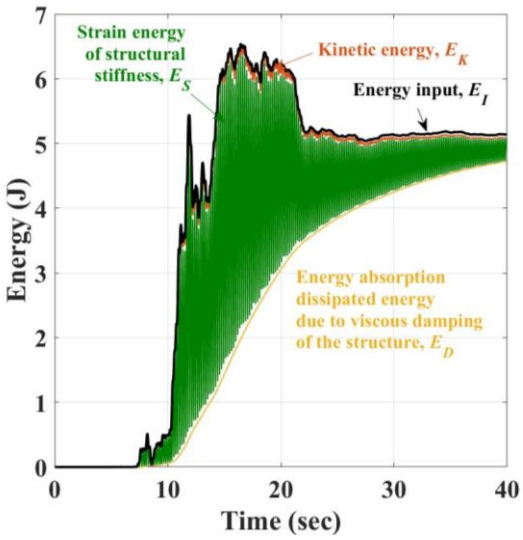

(a) Fixed-base case

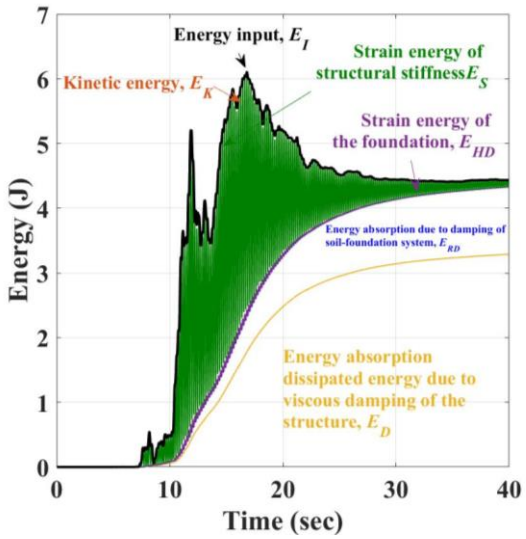

(b) Linear SSI case

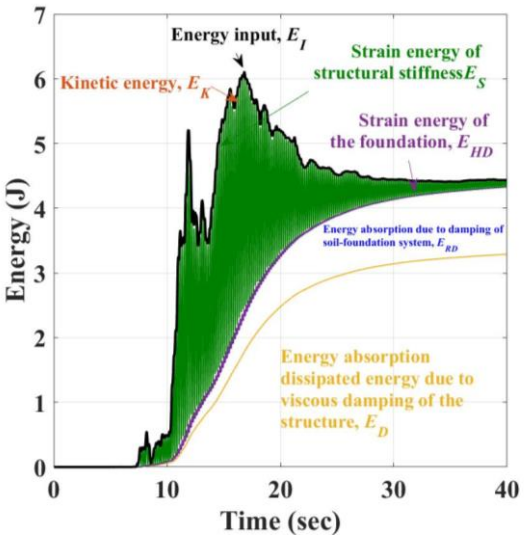

(c) Nonlinear SSI considering the foundation uplift case

Figure 3.17 Energy in time history when the structure is subjected to 50 cm/s^2 ground motion.

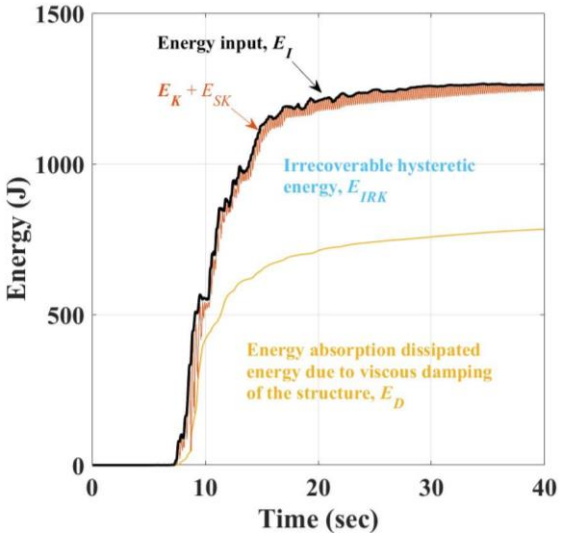

(a) Fixed-base case

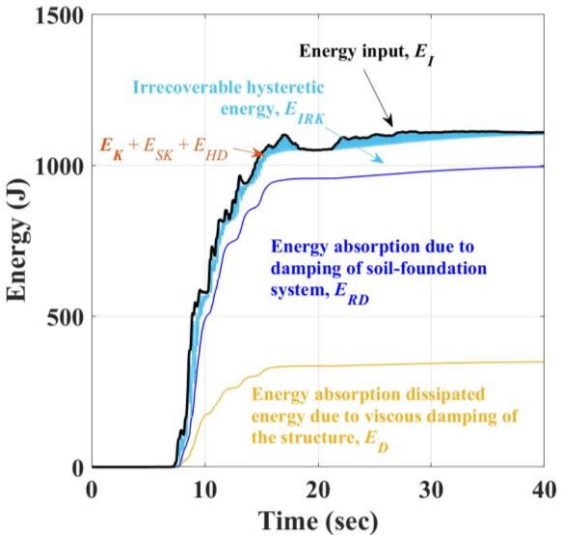

(b) Linear SSI case

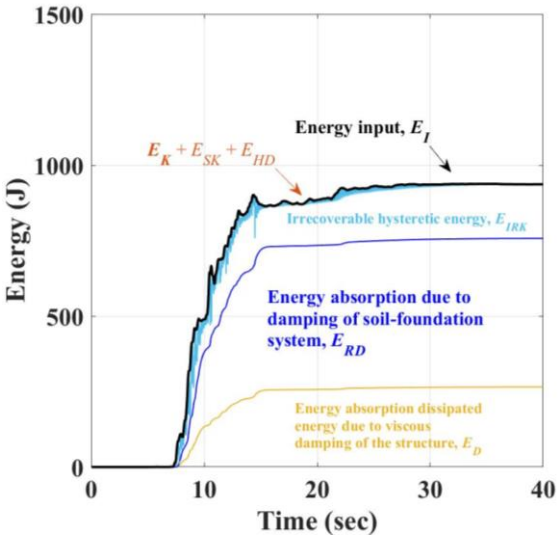

(c) Nonlinear SSI considering the foundation uplift case

Figure 3.18 Energy in time history when the structure is subjected to 800 cm/s^2 ground motion.

Figure 3.18 illustrates the energy variation with time for the structure subjected to the comparatively large ground motion of 800 cm/s^2. The results are compared with the cases having a fixed-base foundation and that considering the soil–structure interaction allowing the foundation, as presented in Figures 3.18(a) and 3.18(b), clarifying the difference in the energy variation for the cases with a fixed base and considering the foundation. The foundation uplift reduces the structural velocity responses. In Figure 3.18(a), when the structure is subjected to a more intensive ground motion, the energy is absorbed by the nonlinear structural stiffness resulting from the remarkable hysteresis loop. This cumulative nonlinear deformation may

damage the superstructure. In contrast, Figure 3.18(c) illustrates that the foundation uplift tends to reduce the energy absorption by the nonlinear structural stiffness.

The maximum energy input to the structure in the cases of a fixed base, linear SSI, and nonlinear SSI considering the foundation uplift with various ground motion amplitudes are compared and discussed in the subsequent section.

3.5.1 Low-rise building

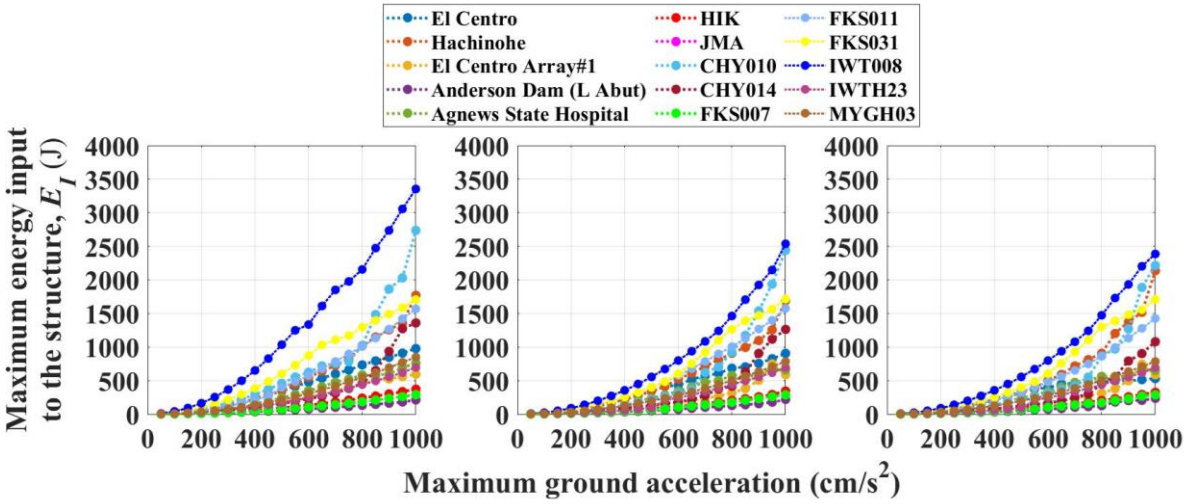

(a) Fixed-base case (b) Linear SSI case (c) Foundation uplift case

Figure 3.19 Maximum energy input of the low-rise building when subjected to various ground motions.

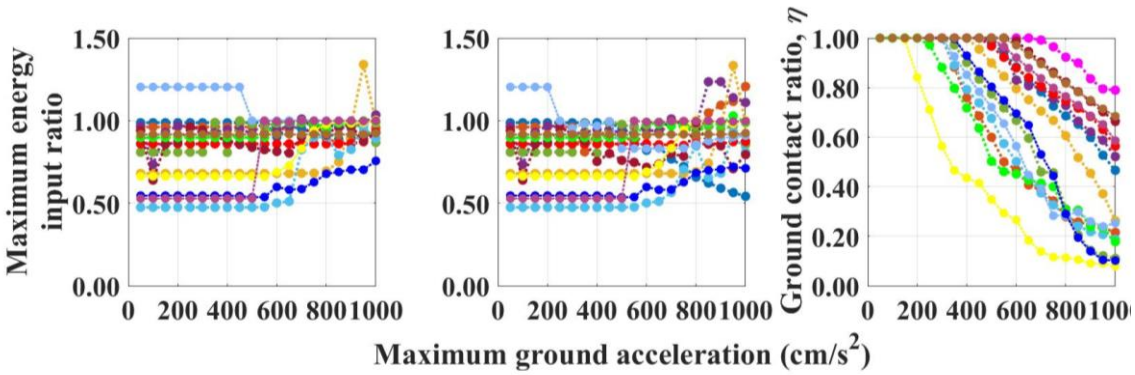

(a) Ratio of the linear SSI to fixed-base case (b) Ratio of the nonlinear SSI to the fixed base case (c) Minimum ground contact ratio

Figure 3.20 Comparison of energy input ratio of the low-rise building when subjected to various ground motions.

Figure 3.19 compares the maximum energy input to the structure for the fixed-base, linear SSI, and nonlinear SSI with the foundation uplift cases when the low-rise building is subjected to various ground motion amplitudes. Figure 3.19 demonstrates that, in most cases, the maximum energy for the case considering the foundation uplift results in less maximum input energy to the structure when compared to the fixed-base foundation. Figure 3.20 depicts the maximum energy input ratios for the cases considering the linear and nonlinear SSI with the foundation uplift to the structural acceleration response of the fixed-base case. Figures 3.20(a) and 3.20(b) highlight the beneficial effect of the linear soil–structure and nonlinear soil–structure interactions considering the foundation in reducing the energy imparted to the structure. However, when the structure is subjected to a low-frequency seismic motion, the energy input to the structure becomes excessive for the case considering the foundation uplift (e.g., when the structure is subjected to the ground motion recorded at Hachinohe Harbor during the 1968 Tokachi–Oki Earthquake), as indicated in Figure 3.20(b) corresponding to the ground contact ratio in Figure 3.20(c). Nevertheless, when the low-rise structure is subjected to the recorded ground motions at FKS007 during the 2011 Tohoku Earthquake, the energy for the linear SSI becomes more extensive than in other cases because the predominant frequency of the ground motion is close to the natural frequency at the first mode of the linear SSI structure system.

3.5.2 Medium-rise building

The maximum energy input to the structure when the medium-rise building sustained on stiff soil is subjected to various ground motion amplitudes for the cases with a fixed base, linear SSI, and nonlinear SSI considering the foundation uplift are compared in Figure 3.18. The maximum input energy to the structure value for the fixed-base case is mostly higher than those for the cases of the structure for the linear and nonlinear SSI with the foundation uplift, except when the structure is subjected to the low-frequency seismic motion (i.e., the ground motion recorded at Hachinohe Harbor during the 1968 Tokachi–Oki Earthquake), as illustrated in Figure 3.21. For the discussion, the ratio of the input energy is presented in Figure 3.22 for the structures considering the linear and nonlinear SSI with the foundation uplift to the fixed-base foundation structure. The input energy ratio for the structure with the linear and nonlinear SSI considering the foundation uplift tends to be less than that for the structure in the fixed-base case. In contrast, when the structure is subjected to the ground motions recorded at Hachinohe Harbor the 1968 Tokachi–Oki Earthquake, the foundation uplift becomes excessive, making the structures more unstable. The foundation uplift may reduce and change the natural

frequency of structures; thus, it may be close to the predominant frequency of the ground motions, which will become the resonance state and make the structures more unstable. However, when the predominant frequency of the ground motion is close to the structure system (e.g., recorded ground motion at the Agnews State Hospital station during the 1989 Loma Prieta Earthquake), it will become a resonance state, resulting in a higher energy input. This indicates that the reduction effect of the SSI, especially the foundation uplift, depends on various factors, including the structure and frequency characteristics of the seismic motion, which must repeatedly be investigated and discussed to ensure the effect of the nonlinear soil–structure interaction considering the foundation on structures.

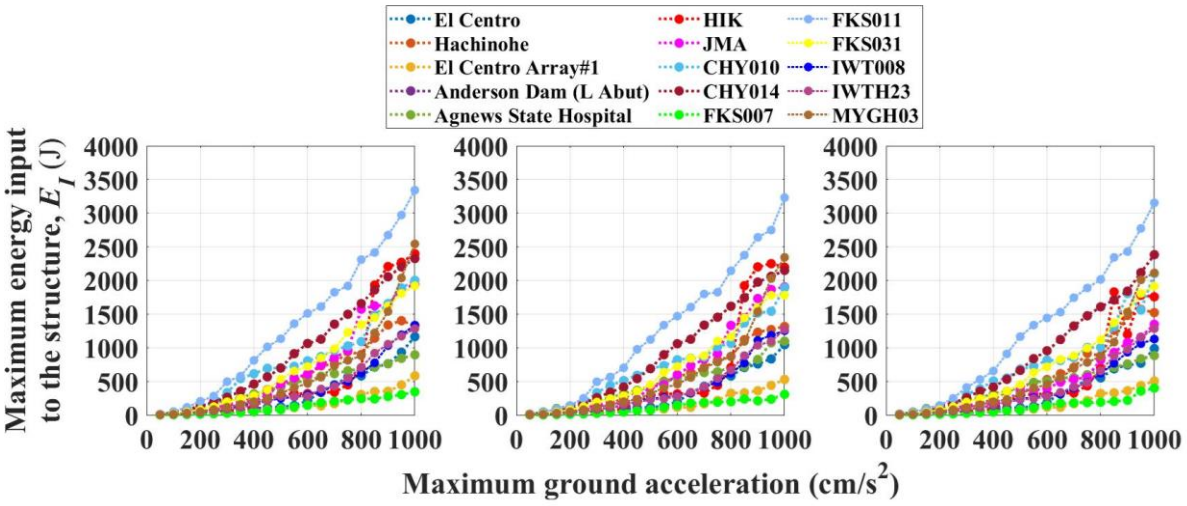

(a) Fixed-base case (b) Linear SSI case (c) Foundation uplift case

Figure 3.21 Maximum energy input of the medium-rise building when subjected to various ground motions.

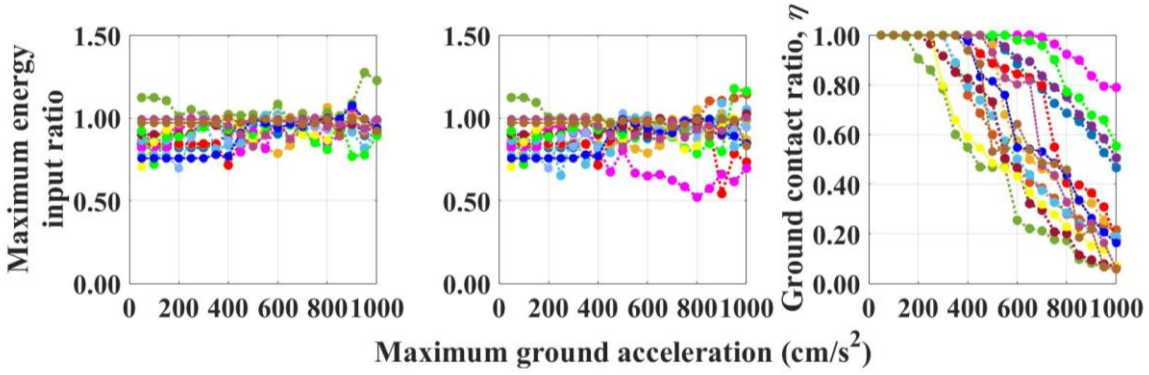

(a) Ratio of the linear SSI to fixed-base case (b) Ratio of the nonlinear SSI to the fixed base case (c) Minimum ground contact ratio

Figure 3.22 Comparison of energy input ratio of the medium-rise building when subjected to various ground motions.

3.6 Summary

This chapter discussed the effect of the seismic isolation caused by the foundation uplift on structures using the energy concept. This study specifically focused on the amount of irrecoverable hysteretic energy that can be used to estimate the structural damage and considered a low-rise building and a five-story building constructed on a mat foundation supported by stiff soil. The current chapter compared the performances under three different scenarios (i.e., fixed-base condition, structure considering the linear soil–structure interaction, and structure considering the nonlinear soil–structure interaction with the foundation uplift) to discuss the foundation uplift effect. The structures were subjected to 15 different ground motions recorded during various earthquake events. The obtained results are as follows:

1. The soil–structure interaction, especially the nonlinear soil–structure interaction with the foundation uplift, positively affects the structure because the foundation uplift works to cut off the seismic motion, resulting in less structural acceleration responses.
2. The effectiveness of the foundation uplift in reducing the structural responses depends on the intensity and frequency characteristics of the earthquake ground motion. In some cases, the foundation uplift may not effectively reduce the structural responses, such as when a structure is subjected to a high-intensity and low-frequency ground motion.
3. The foundation uplift has a beneficial effect in reducing the input energy, which may result in smaller structural velocity responses. However, the amount of the energy input to the structure can be influenced by the intensity and frequency characteristics of the earthquake ground motion, which can affect the structural responses.
4. The foundation uplift may prevent the occurrence of a hysteretic loop or the accumulation of the nonlinear deformation of the superstructure.

Some factors, such as the structural slenderness ratio and the foundation size, must still be considered because the reduction effect varies depending on the dynamic characteristics of the structure and the input ground motion. Further research is also necessary to better understand the complex interactions between these various factors and develop a more accurate predicting method for the effectiveness of the foundation uplift in various situations. Additionally, experiment tests are recommended to verify the investigation in this work.

References

[1] Osaki, J.: *Architectural Vibration Theory*, Shokoku-sha, 1996. (in Japanese).

[2] Oliveto, G., Caliò, I. and Greco, A.: A large displacement behaviour of a structural model with foundation uplift under impulsive and earthquake excitations, *Earthquake Engineering and Structural Dynamics*, 32, 369-393, 2003.

[3] Hayashi, Y.: Damage reduction effect due to basemat uplift of buildings. *Journal of Structural and Construction Engineering*, 485, 53-62, 1996. (in Japanese)

[4] Iwashita, K. and Taniguchi, H.: Effect of uplift on earthquake response of building, *Proceedings of the 12th World Conference on Earthquake Engineering (WCEE)*, 1328, 2000.

[5] Ghannad, M.A. and Jafarieh, A.H.: Inelastic displacement ratios for soil–structure systems allowed to uplift, *Earthquake Engineering and Structural Dynamics*, 43, 1401-1421, 2014.

[6] Dolatshahi, KM., Vafaei, A., Kildashti, K. and Hamidia, M.: Displacement ratios for structures with material degradation and foundation uplift, *Bulletin of Earthquake Engineering*, 17, 5133-5157, 2019.

[7] Sarrafzadeh, E., Lim, E., Qin, X. and Chouw, N.: Effect of plastic hinge, soil nonlinearity and uplift on earthquake energy in structure, *Proceedings of the 2014 New Zealand Society for Earthquake Engineering (NZSEE) Conference*, 2014.

[8] Inoue, T. and Mikami, A.: Investigation of stress reduction effect on structures due to basemat uplift using energy concept, *International Journal of GEOMATE*, 6, 749-756, 2014.

[9] Inoue, T. and Mikami, A.: Investigation of stress reduction effect of bridge pier due to non-linear dynamic interaction using energy concept, *Proceeding of JSCE A1 (Structural and Earthquake Engineering)*, 76, 41-60, 2014. (in Japanese)

[10] Inoue, T. and Mikami, A.: Study on stress reduction effect of bridge pier due to basemat uplift and soil yielding, *Japanese Geotechnical Journal*, 10, 1-16, 2014. (in Japanese)

[11] Nakatani, S., Shirato, M. and Kouno, T.: Development of a numerical analysis model to predict seismic behavior of shallow foundations, *Public Works Research Institute Report*, ISSN 0386-5878, No. 4101, 2008 (in Japanese).

[12] TDAP III Batch Version User's Guide Version 3.09, *ARK Information Systems*, INC, 2017. (in Japanese)

[13] Ministry of Land, Infrastructure, Transport and Tourism, Ministry of Construction Notification No. 1347 (Allowable soil stress and foundation structure), Japan, 2001. (in Japanese)

[14] NEHRP, National Earthquake Hazard Reduction Program, Recommended provisions for seismic regulations of new buildings: Part I, Provisions, FEMA 222A, Federal Emergency Management Agency, Washington, D.C., 1994.
[15] ASCE: Minimum Design Loads and Associated Criteria for Buildings and Other Structures, *ASCE/SEI 7-10*, 2010.
[16] Kanai, K., Seismology in Engineering, Tokyo University, Japan, 1983.
[17] Varecha V. P., Fadllan A., and Hartono, H.: Soil classification using horizontal to vertical spectrum ratio methods on Scilab in Sendangmulyo, Semarang, *Physics Education Research Journal*, 4, 71-78, 2022.
[18] Chopra, AK. *Dynamics of Structures*: *Theory and Applications to Earthquake Engineering*. Prentice Hall, Inc., Englewood Cliffs, New Jersey, 1995.
[19] Akiyama, J. *Earthquake-Resistant Design Method for Buildings Based on Energy Balance*, Gihodo Publishing, Japan 1999. (in Japanese)

4. EARTHQUAKE–TSUNAMI MULTIHAZARD ANALYSIS CONSIDERING FOUNDATION UPLIFT

After the physics of the foundation uplift problems were discussed in Chapters 2 and 3, this chapter combines the earthquake–tsunami multihazard problems considering the foundation uplift problems. Section 4.1 introduces the study background and purpose. Section 4.2 describes the framework analysis. Section 4.3 explains the definition of the limit state considered in this study. Sections 4.4 and 4.5 clarify the earthquake and tsunami loadings. Sections 4.6 presents the earthquake–tsunami interaction diagrams. Section 4.7 summarizes this chapter.

4.1 Background and Purpose

Mimura et al. [1] reported that the combination of sequential earthquakes and tsunamis resulted in extensive damage to numerous coastal area structures during the 2011 Tohoku Earthquake and Tsunami events. Large intensive earthquakes generate massive tsunamis that cause considerable damage to coastal structures; hence, a method for evaluating the effects of sequential earthquake–tsunami hazards (i.e., a multihazard) is essentially required. Studies on the combined earthquake–tsunami disasters are nowadays garnering considerable interest. For example, Carey et al. [2] established an earthquake–tsunami interaction diagram that can illustrate that a structures' resistance to subsequent tsunamis is reduced by the effects of the earthquake on the structure. Carey et al. [2] focused on the bridge structure considering the soil–structure interaction and prescribed the structural damage as the limit state. However, during the 2011 Great Tohoku Earthquake, numerous buildings were overturned by the earthquake and the following tsunami [3], which are directly associated with the loss of human life and must be prevented. The foundation uplift significantly affects the structural responses during earthquakes (Chapter 3). This chapter further develops the earthquake–tsunami interaction diagram by considering the foundation uplift because the limit state considered as the target structure system is different. Whether or not the building or foundation damage has a dominant effect may differ depending on the input seismic motion characteristics. This chapter simultaneously considers two different limit states, namely the inter-layer deformation angle that represents the structural damage, and the ground contact ratio that denotes the amount of the foundation uplift. The purpose of this chapter is explained in Sections 4.6.1 and 4.6.2 and summarized as follows.

(1) Earthquake–tsunami interaction diagrams are further developed by considering the

foundation uplift.

(2) The earthquake–tsunami interaction diagrams are further developed by simultaneously considering the foundation uplift and the inter-layer deformation.

4.2 Analytical Framework and Earthquake–Tsunami Interaction Diagram

This study follows the analysis framework developed by Carey et al. [2]; therefore, this chapter describes the analytical framework and the flow chart of the earthquake–tsunami interaction diagram method.

4.2.1 Analytical framework

Referring to Carey et al. [13], the earthquake–tsunami framework analysis sequence is separated into three stages , as illustrated in Figure 4.1.

4.2.1.1 Stage 1: Earthquake ground motion loading

In the first stage, the earthquake ground motion is applied to a shallow foundation at the ground surface level, as presented in Figure 4.1(a). This stage applies the ground motion as earthquake loading to the structure at the ground surface level for the time history analysis.

4.2.1.2 Stage 2: Before the tsunami loading

In the second stage, the structure is presented as the initial condition with its damaged state caused by the earthquake. This study considers the application of zero external load in the second stage before the tsunami loading. Note that Mimura et al. [1] reported that the time between the 2011 Tohoku Earthquake and the arrival time of the highest tsunami waves in Iwate Prefecture is approximately 30 to 40 min. However, a tsunami force is applied to the structure after the earthquake analysis a few minutes later in this study.

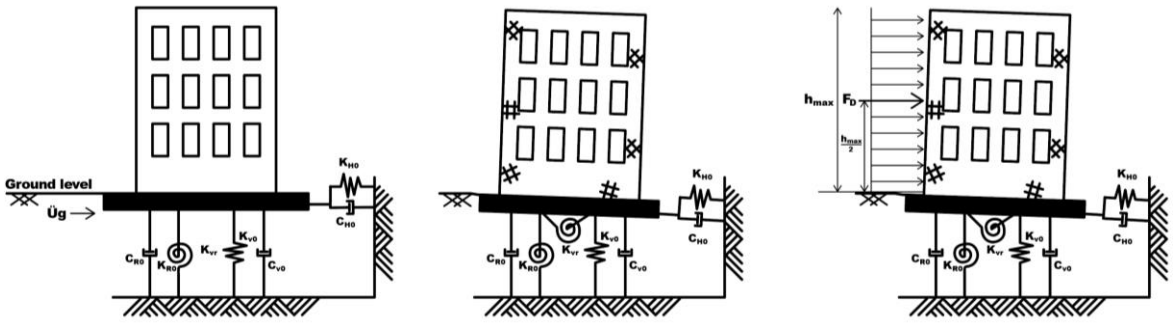

(a) Earthquake loading (b) Preparation before a tsunami (c) Tsunami loading

Figure. 4.1 Analysis framework of the three stages

4.2.1.3 Stage 3: Tsunami loading

The third stage involves a hydrodynamic pushover analysis. Referring to ASCE/SEI 7-16 [3], the hydrodynamic force is statically applied to the whole structure from the ground surface level to the specific tsunami height (h), and the tsunami flow velocity is evaluated as entirely uniform with the tsunami height. Accordingly, the hydrodynamic pressure distribution will be treated as a uniform load. Figure 4.1(c) illustrates the hydrodynamic force applied at the center of the tsunami height by assuming the maximum tsunami height (h_{max}). The hydrodynamic force intensity is increased by gradually increasing the tsunami flow velocity (u) in a nonlinear pushover analysis [4] until the defined limit state is reached.

4.2.2 Earthquake–tsunami interaction diagram method

We referred to the approach of Carey et al. [2] in this work. The interaction diagrams for the sequential earthquake–tsunami multihazards are created following the procedures presented below and in Figure 4.2.

4.2.2.1 Step 1: Define the structure performance.

The limit state is interpreted as the structure failure caused by any of the two (i.e., earthquake or the tsunami) or both. The limit state of a structure is defined here.

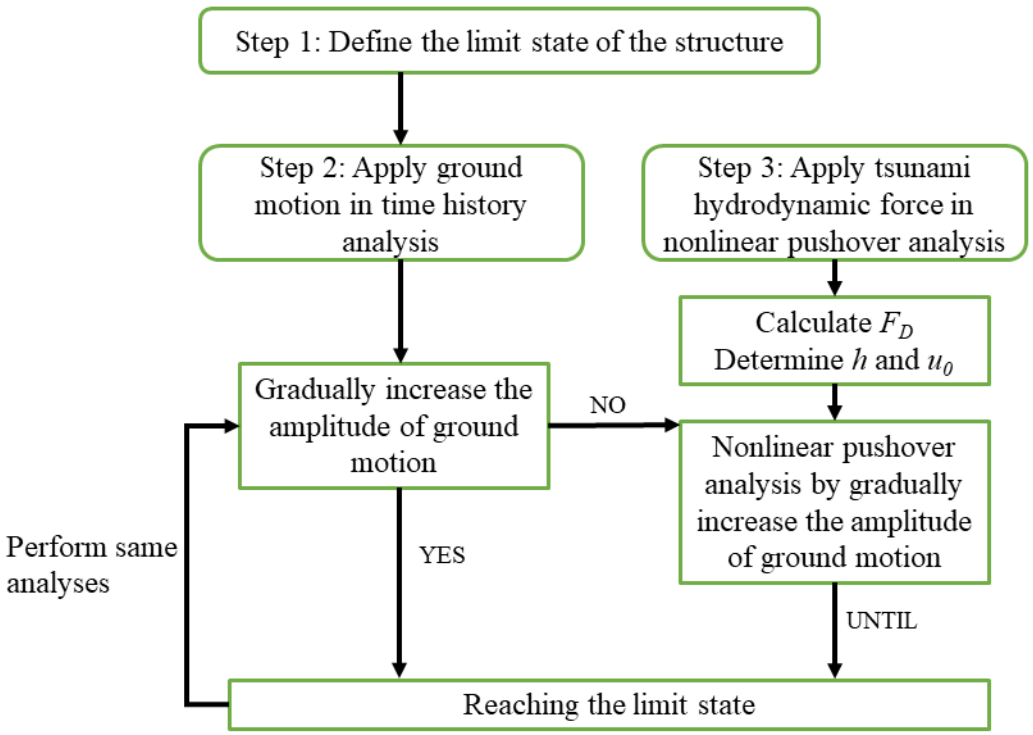

Figure 4.2 Flow chart of the generated the earthquake–tsunami interaction diagram

4.2.2.2 Step 2: Apply a ground motion as an earthquake loading.

An earthquake ground motion is applied at the ground surface of the structure. The ground motion amplitude is gradually increased until the ground motion reaches one of the prescribed limit states.

4.2.2.3 Step 3: Apply the tsunami hydrodynamic force as the tsunami loading.

A fixed inundation depth of tsunami (h) and an initial tsunami flow velocity (u_0) are determined. The hydrodynamic force (F_D) is calculated using Equation (4.1) (Section 4.5). After the second stage, the F_D is given as the input loading to the structure. The nonlinear static pushover analysis starts by increasing the tsunami flow velocity.

$$F_D = \frac{1}{2} C_D \rho B (hu^2) \tag{4.1}$$

4.3 Limit State

According to ASCE/SEI 7-10 [5], the limit state is the condition beyond which a structure or a portion of a structure is considered to no longer be suitable for its intended use and is judged unsafe. This definition corresponds to serviceability, which refers to the point at which a structure may still be standing, but can no longer perform its intended function or provide a satisfactory service level to its users. Referring to the work of Carey et al. [2], the limit state is denoted as the structure failure caused by either one or both of the hazards considering the effects of a combined earthquake and tsunami. Carey at el. [2], however, only prescribed the story drift ratio (i.e., inter-layer deformation angle) as the limit state. In Section 4.6.2, the earthquake–tsunami interaction diagram is further developed by simultaneously considering two different limit states as the objective of this chapter. Therefore, two prescribed limit states in this study are explained below.

4.3.1 Inter-layer deformation angle

The inter-layer drift deformation angle or story drift angle is the first prescribed limit state in this work because it may indicate a direct link to building damage. The inter-layer drift deformation angle is the ratio of the relative displacement of each floor to the height of each layer. Referring to the building structural design standards [6], the limit value of the inter-story drift angle (δ) is 1/200.

4.3.2 Ground contact ratio

The degree of the foundation uplift that can be indicated by the ground contact ratio is

prescribed as the second limit state because the amount of deformation in some structures (e.g., foundation structure) must be considered to verify structural safety [7]. Referring to the Nuclear Standard Committee of the JEA [8] and the description in Section 2.2.2, special consideration is needed to accurately investigate the foundation uplift phenomenon when the ground contact ratio is less than 50%. Therefore, the limit value of the ground contact ratio (η) is less than 50%.

4.4 Earthquake Loading

This study prepares the subduction-zone ground motions recorded during the 2011 Great Tohoku Earthquake (Mw 9.0), which occurred at 14:46 JST on March 11, 2011. In this chapter, 30 recorded ground motions from the Fukushima, Iwate, and Miyagi prefectures, which suffered the largest damages from the 2011 Tohoku Earthquake and Tsunami events, from the K-NET and the KiK-net stations were selected, as shown in Figure 4.3. Table 4.1 summarizes the 30 selected ground motion properties, where the PGA stands for peak ground acceleration; S_a is the spectral acceleration calculated by assuming 5% damping at the first period of the soil–structure interaction system; F_e is the predominant frequency of the ground motion; and f_0 is the fundamental natural soil frequency used to classify the soil characteristics. The soil classification differs from Section 2.6 due to the soil information.

As described in Section 4.2, the recorded ground motion amplitude is gradually increased until the defined limit states are attained to create a diagram representing the interaction between an earthquake and a tsunami.

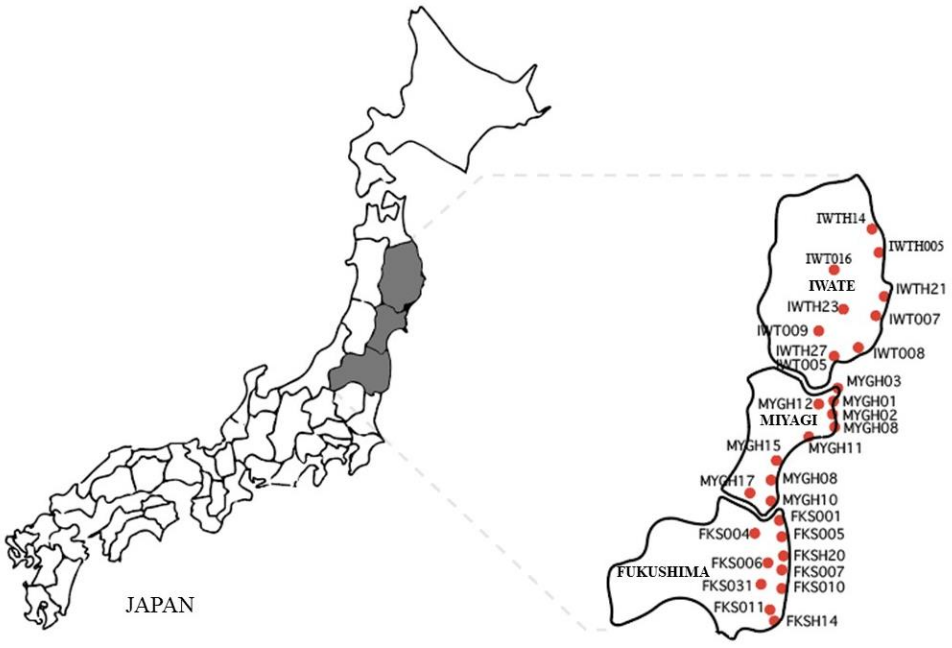

Figure 4.3 Stations in three prefectures in the Tohoku area site map

Table 4.1 Thirty ground motions recorded in three prefectures in the 2011 Tohoku Earthquake–Tsunami events

Prefecture	Station	PGA (cm/s^2)	S_a at T_1 (cm/s^2)	F_e (Hz)	f_0 (Hz)	Type
Fukushima	FKS001	552.720	851.620	2.417	3.810	III
Fukushima	FKS004	504.700	1312.220	4.993	5.935	II
Fukushima	FKS005	444.920	1494.500	3.442	8.172	II
Fukushima	FKS006	525.280	1254.400	2.344	4.334	II
Fukushima	FKS007	690.900	1256.360	4.761	8.257	II
Fukushima	FKS010	882.000	2720.480	2.739	6.521	II
Fukushima	FKS011	311.640	826.140	2.966	5.551	II
Fukushima	FKS031	407.680	1279.880	1.269	10.914	II
Fukushima	FKSH14	122.500	363.580	0.476	1.971	IV
Fukushima	FKSH20	356.720	185.220	2.576	2.590	III
Iwate	IWT005	163.660	353.780	1.159	7.252	II
Iwate	IWT007	696.780	1179.920	2.576	3.970	III
Iwate	IWT008	323.400	839.860	3.577	18.751	II
Iwate	IWT009	512.540	1692.460	6.323	8.143	II
Iwate	IWT016	236.180	590.940	7.397	5.097	II
Iwate	IWTH05	654.640	1144.640	9.119	4.660	II
Iwate	IWTH14	229.320	257.740	4.053	7.252	II
Iwate	IWTH21	413.560	1628.760	1.697	4.985	II
Iwate	IWTH23	148.960	268.520	1.685	7.691	II
Iwate	IWTH27	98.980	870.240	2.649	5.586	II
Miyagi	MYG001	426.300	1594.460	4.126	8.929	II
Miyagi	MYG002	657.580	2167.760	6.677	8.324	II
Miyagi	MYG008	294.000	837.900	1.550	6.353	II
Miyagi	MYG011	687.960	1374.940	5.774	15.684	II
Miyagi	MYG015	352.800	560.560	2.234	2.369	IV
Miyagi	MYG017	348.880	837.900	2.209	1.376	IV
Miyagi	MYGH03	133.280	187.180	2.002	7.783	II
Miyagi	MYGH08	255.780	731.080	1.782	1.695	IV
Miyagi	MYGH10	852.600	2463.720	7.177	2.896	III
Miyagi	MYGH12	459.620	849.660	14.705	6.233	II

*Site classification: Type II (medium), Type III (soft), and Type IV (very soft)

References: [9] and [10]

Kanai, K., Seismology in Engineering, Tokyo University, Japan, 1983.

Varecha V. P., Fadllan A., and Hartono, Soil Classification Using Horizontal to Vertical Spectrum Ratio Methods on Scilab in Sendangmulyo, Semarang, *Physics Education Research Journal*, Vol. 4, No.2, pp. 71-78, 2022.

4.5 Tsunami Loading

Although the buoyancy and debris impact forces in FEMA 2019 [11] are significant forces that needed consideration, Carey et al. [2] suggested that the hydrodynamic force (F_D) is the main factor for the overturned buildings during the 2011 Great East Japan Earthquake and Tsunami events [12,13]. This study focuses on F_D as the tsunami loading with reference to FEMA 2019 [11]. The hydrodynamic force is applied to the structure, as illustrated in Figure 4.1(c) and calculated using Equation (4.1), where ρ is the seawater density, including the sediment; C_D is the drag coefficient; B is the building width that the tsunami affects; h is the tsunami height; and u is the tsunami flow velocity. Table 4.2 presents the parameters for calculating the tsunami hydrodynamic force with reference to FEMA 2019 [11]. Following the suggestions of Carey et al. [2], the tsunami height (h) and initial tsunami velocity (u) are determined and fixed. The tsunami loading intensity (i.e., hydrodynamic force) is also increased by increasing the tsunami flow (u) in the nonlinear pushover analysis.

Although some investigation reports [1] presented that the interval between the 2011 Tohoku Earthquake and the arrival of the highest tsunami waves in the Iwate Prefecture is approximately 30 to 40 min, in this work, a tsunami force is applied a few minutes after the earthquake.

Table 4.2 Parameters for the calculating the tsunami hydrodynamic force

Parameters	Value
Sea water density, including sediment, ρ (t/m^3)	1.2
Drag coefficient, C_d	2
Building width that the tsunami affected, B (m)	10

4.6 Computation Results

In this chapter, the earthquake–tsunami interaction diagrams are further developed into two parts. Section 4.6.1 presents the earthquake–tsunami interaction diagrams considering the foundation uplift by determining only one limit state, that is, the ground contact ratio, but considering different levels (η < 75%, η < 65%, and η < 50%). Note that the structure is considered based on a linear assumption in Section 4.6.1. In Section 4.6.2, the earthquake–tsunami interaction diagrams are further developed by simultaneously considering two different limit states, namely the inter-layer deformation angle and the ground contact ratio. Reports on the structural damage by the 2011 Tohoku Earthquake and Tsunami event showed that the overturned buildings were mainly low-rise buildings sustained on a shallow foundation. Therefore, the three-story building on a mat foundation sustained on stiff soil described in Section 2.4.1 is the analytical model used in the current chapter. For simplicity, a horizontal–vertical interactive sway-rocking model is considered (Section 2.2.2) to calculate the structural responses considering the foundation uplift against earthquake and tsunami events.

4.6.1 Earthquake–tsunami interaction diagram considering the foundation uplift

Figures 4.4 and 4.5 display examples of two different mechanisms for the structure reaching the limit state for a comparatively small earthquake and a large earthquake, respectively, when the structure is subjected to the ground motion recorded at the IWTH23 station. Figure 4.4(a) presents the time history of the rotational displacement of the foundation for each of the three different stages (i.e., 0–300, 300–400, and 400–600 s). Figure 4.4(b) illustrates the corresponding ground contact ratio time histories. Figure 4.4 demonstrates that the ground motion is not large enough to reach the limit state during the earthquake; therefore, the prescribed limit state (η < 50%) is reached by tsunami loading. Figure 4.5 illustrates the time histories of the foundation deformation and the corresponding time histories of the foundation–ground contact ratio, which is intensive enough for reaching the limit state during an earthquake. The dashed line in the figure indicates the limit state.

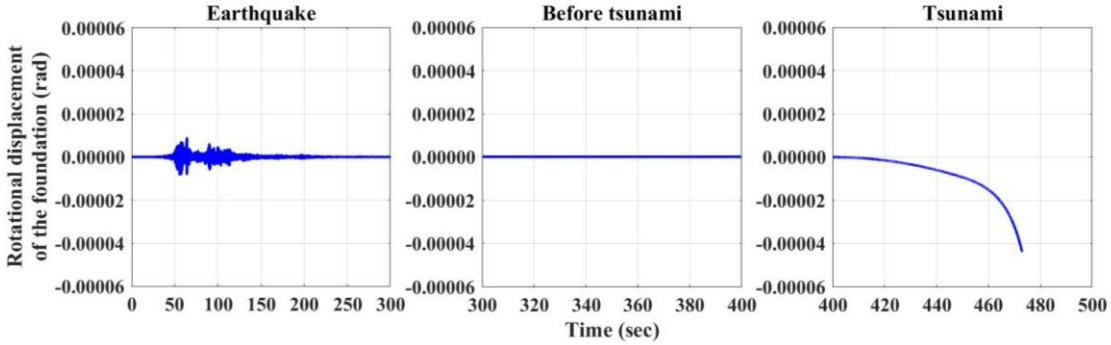

(a) Rotational displacement if the foundation

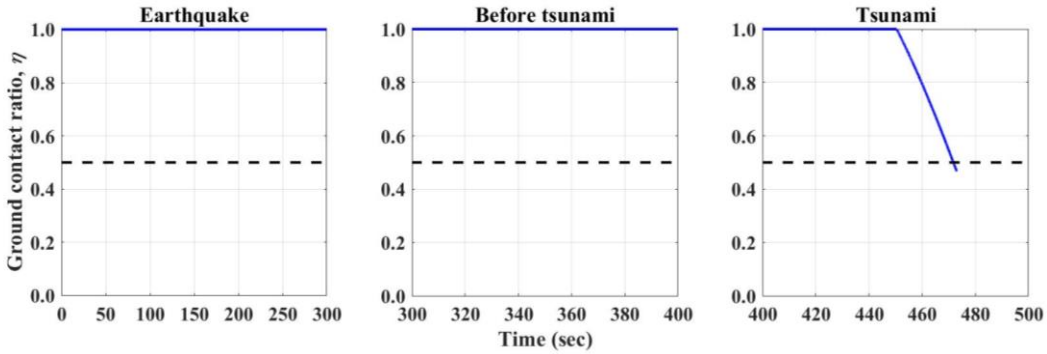

(b) Ground contact ratio

Figure 4.4 Response when the tsunami via the hydrodynamic force reached the prescribed limit state.

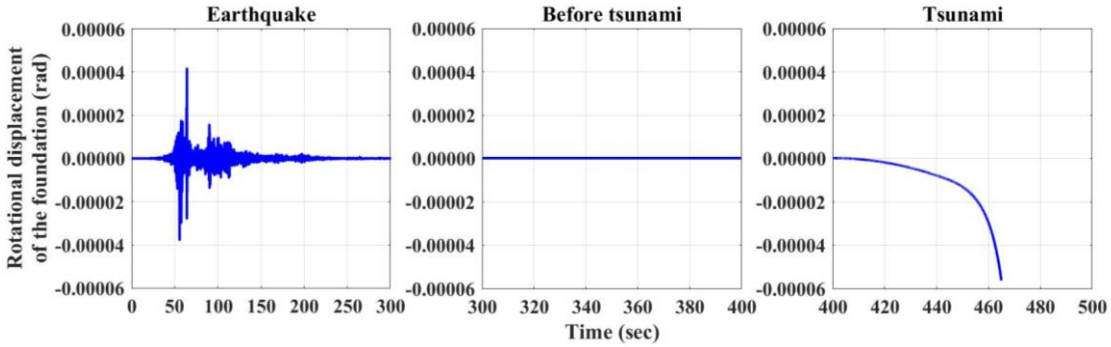

(a) Rotational displacement if the foundation

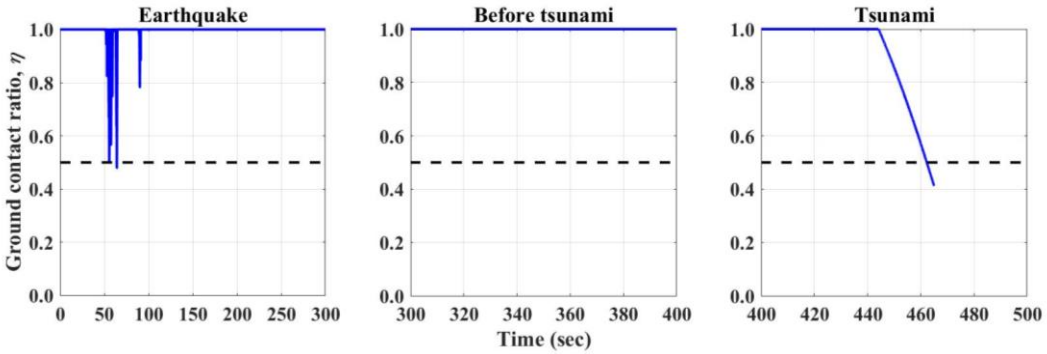

(b) Ground contact ratio

Figure 4.5 Response when the ground motion reached the prescribed limit state.

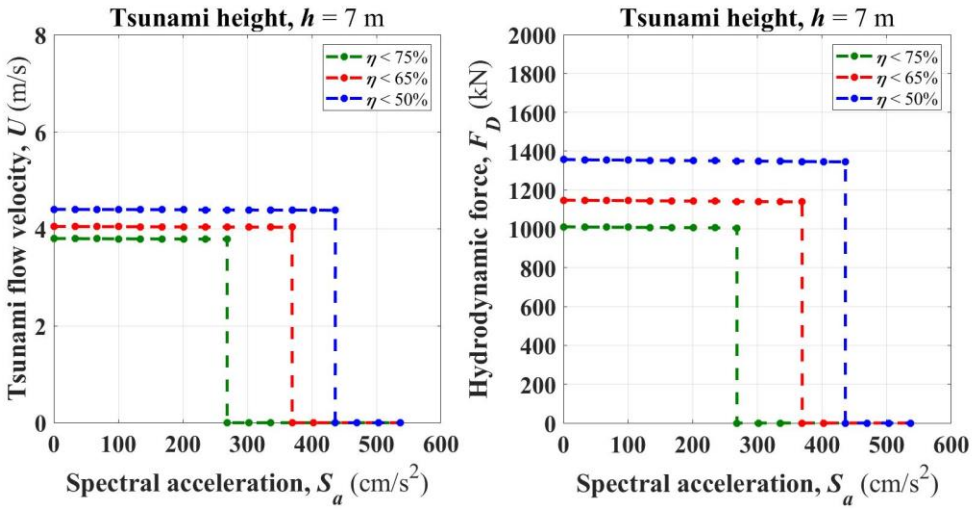

(a) Tsunami flow velocity and hydrodynamic force at a tsunami height of 7 m

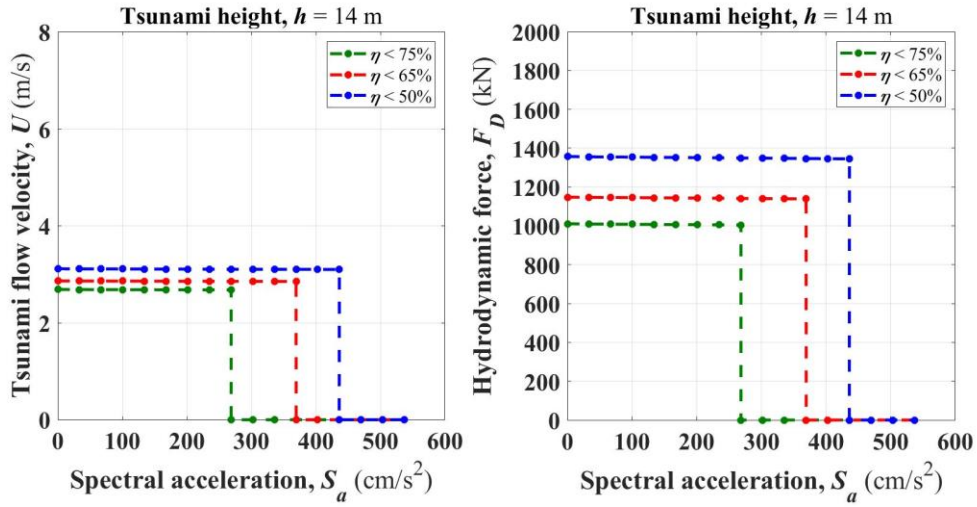

(b) Tsunami flow velocity and hydrodynamic force at a tsunami height of 14 m

Figure 4.6 Four examples of the earthquake–tsunami interaction diagrams when the structure is subjected to the recorded ground motion at the IWTH23 station.

Figure 4.6 shows four examples of the earthquake–tsunami interaction diagrams for two different tsunami heights and the recorded ground motion at the IWTH23 station. The ground motion intensity is depicted at the horizontal axis. The vertical axis denotes the required tsunami hydrodynamic force for reaching the limit state. Figures 4.6(a) and 4.6(b) depict the interaction diagrams of the tsunami velocity and the hydrodynamic force at tsunami heights of 7 and 14 m, respectively. In Figure 4.6, the diagrams indicate that, when the ground motion is low, the limit state is reached due to the tsunami force. Conversely, when the ground motion is large, the tsunami force becomes zero on the vertical axis because the limit state is reached by the ground motion prior to the tsunami arrival. The diagrams also depict that at tsunami heights

of 14 and 7 m, the tsunami flow velocities of the hydrodynamic force for reaching the prescribed limit state are between 2.8 and 4.5 m/s, respectively. The range of the tsunami flow velocities is close to that in the interaction diagrams established by Carey et al. [2], even though the analytical model is different, and an approximate value of the tsunami flow velocity from the tsunami in the 2011 Tohoku Earthquake–Tsunami events is used [14,15].

Figure 4.7 displays the overall interaction diagrams for the 30 ground motions in three prefectures with a tsunami height of 14 m and three limit states (ground contact ratio). Figure 4.7 illustrates that, when the intensity of the spectral acceleration (S_a) is more than 200 cm/s^2,

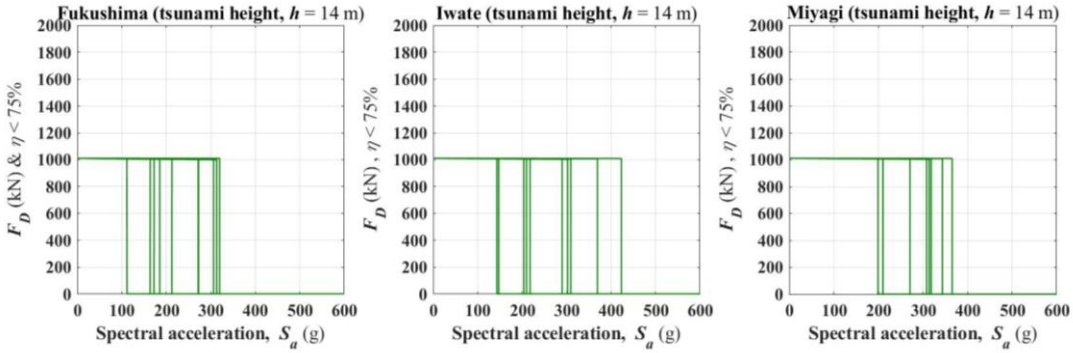

(a) Interaction diagram when the ground contact ratio is less than 75%.

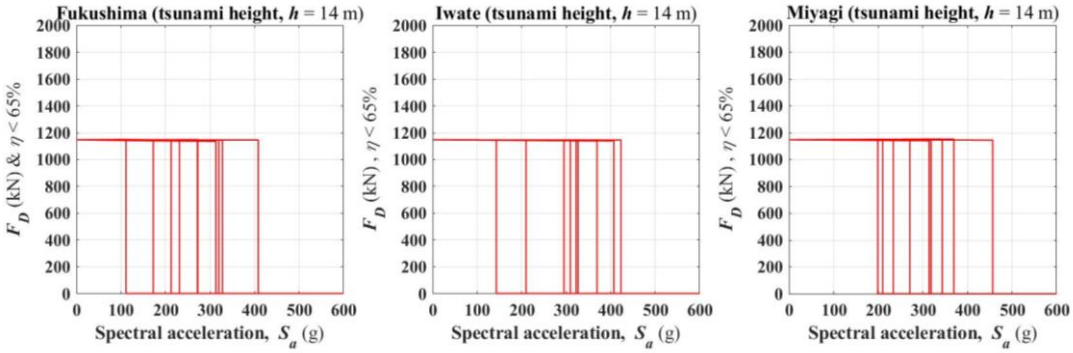

(b) Interaction diagram when the ground contact ratio is less than 65%.

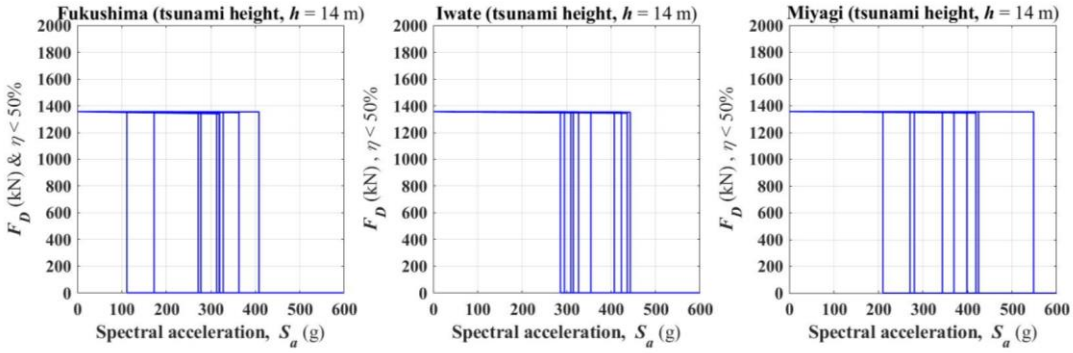

(c) Interaction diagram when the ground contact ratio is less than 50%.

Figure 4.7 Overall interaction diagrams for the Fukushima, Iwate, and Miyagi prefectures with the three prescribed limit states of η <75%, η < 65%, and η < 50%

the hydrodynamic force will not be required in leading this structure to reach the limit states in the three prefectures.

Figures 4.8 and 4.9 present the median and the average interaction diagrams for the three prefectures, respectively. The interaction diagrams illustrate almost constant values for a small S_a range. This means that the earthquakes have slight effects on the tsunami loading needed to reach the limit state when the spectral acceleration (S_a) is lower than 200 cm/s^2 in Fukushima and lower than 300 cm/s^2 in Iwate and Miyagi, as shown in Figure 4.8. Figure 4.9 indicates that at spectral accelerations over 200 cm/s^2, the structure resistance is rapidly reduced for all prefectures. The median and the average earthquake–tsunami interaction diagrams indicate the damage caused by the earthquake intensity, which then reduces the structural resistance to a subsequent tsunami. The earthquake intensity causes a damage that weakens the structural resistance, leaving it vulnerable to a potential tsunami. The earthquake–tsunami interaction diagram estimates the earthquake damage that reduces structural resistance to a subsequent tsunami. The diagrams show that an earthquake might be one factor for overturning buildings, as presented by the earthquake–tsunami interaction diagrams. The

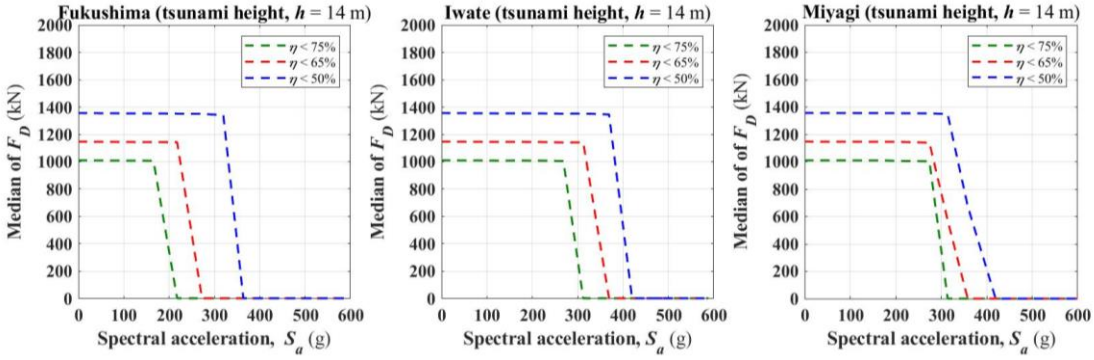

Figure 4.8 Median interaction diagrams for the Fukushima, Iwate, and Miyagi prefectures with the three prescribed limit states of $\eta < 75\%$, $\eta < 65\%$, and $\eta < 50\%$

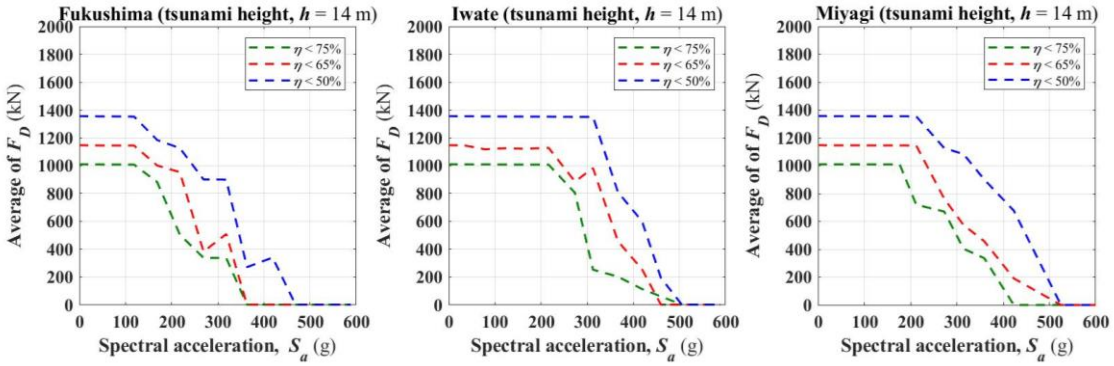

Figure 4.9 Average interaction diagrams for the Fukushima, Iwate, and Miyagi prefectures with the three prescribed limit states of $\eta < 75\%$, $\eta < 65\%$, and $\eta < 50\%$

earthquake characteristics affect the reduction of the structural resistance for tsunami resistance.

4.6.2 Earthquake–tsunami interaction diagram simultaneously considering two different limit states

Damage occurrence cannot be accurately estimated; therefore, this section simultaneously considers two different two different limit states, that is, the inter-layer deformation angle and the foundation uplift. Six ground motions with different frequency characteristics were selected from Table 4.3 to be applied as earthquake loading. Figures 4.10 to 4.15 show the acceleration time history and the power spectrum of the recorded ground motion, even though the properties of the six selected ground motions were already summarized in Table 4.3, to explicitly illustrate the difference in the frequency characteristic of the ground motions.

Table 4.3 Six ground motions recorded to generate the earthquake–tsunami interaction diagram by simultaneously considering two different limit states

Prefecture	Station	PGA (cm/s^2)	S_a at T_1 (cm/s^2)	F_e (Hz)
Fukushima	FKS001	552.720	851.620	2.417
Fukushima	FKS004	504.700	1312.220	4.993
Iwate	IWT005	163.660	353.780	1.159
Iwate	IWT012	454.574	1105.708	4.260
Miyagi	MYG001	426.300	1594.460	4.126
Miyagi	MYG008	294.000	837.900	1.550

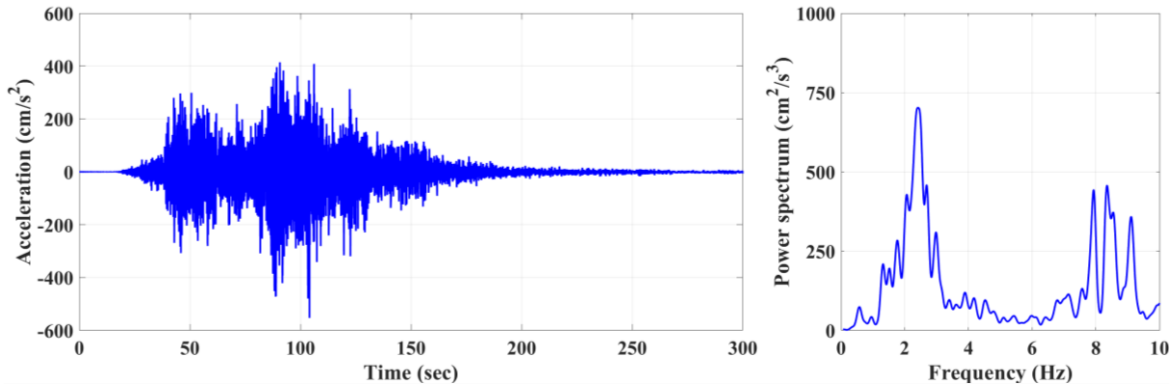

(a) Acceleration time history (b) Power spectrum

Figure 4.10 Ground motion recorded at the FKS001 station

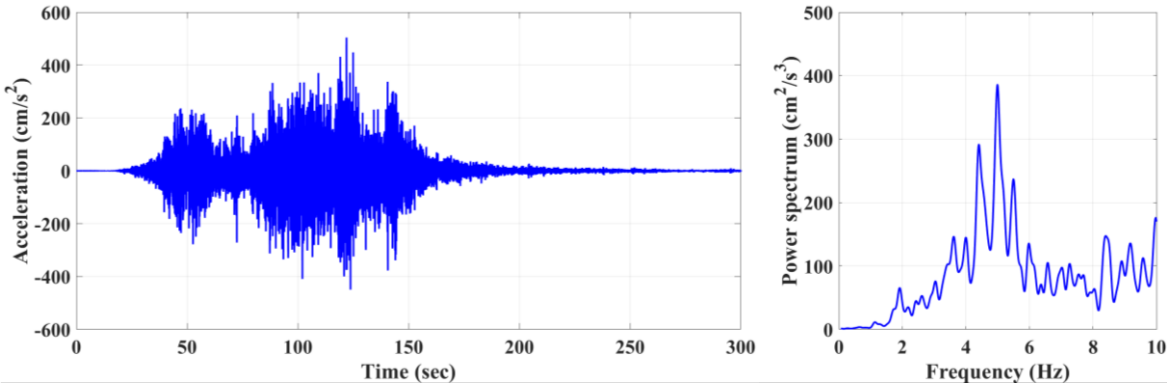

(a) Acceleration time history (b) Power spectrum

Figure 4.11 Ground motion recorded at the FKS004 station

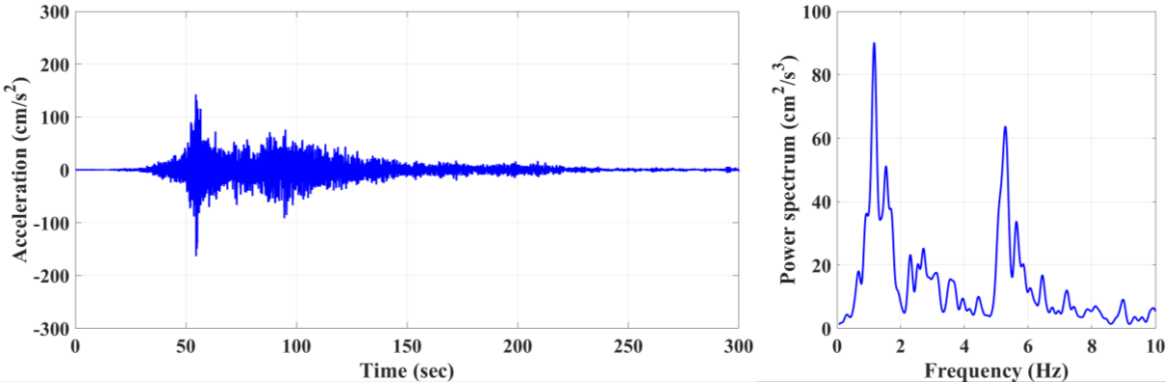

(a) Acceleration time history (b) Power spectrum

Figure 4.12 Ground motion recorded at the IWT005 station

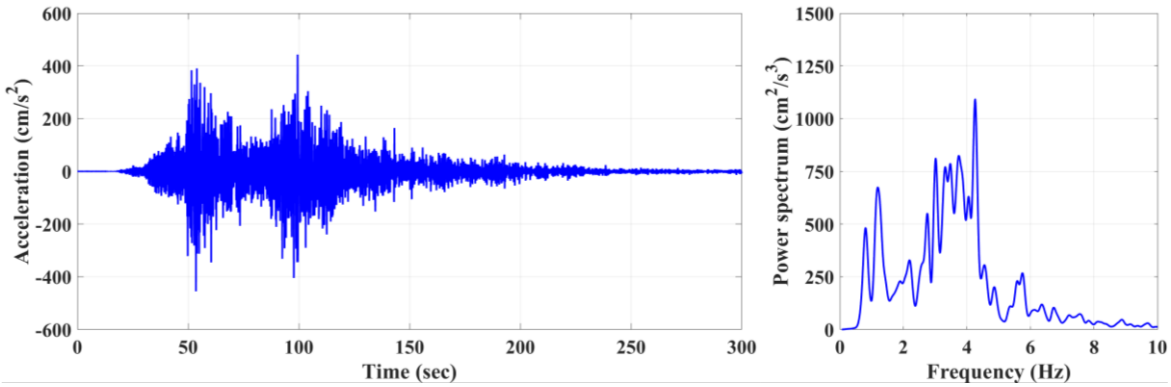

(a) Acceleration time history (b) Power spectrum

Figure 4.13 Ground motion recorded at the IWT012 station

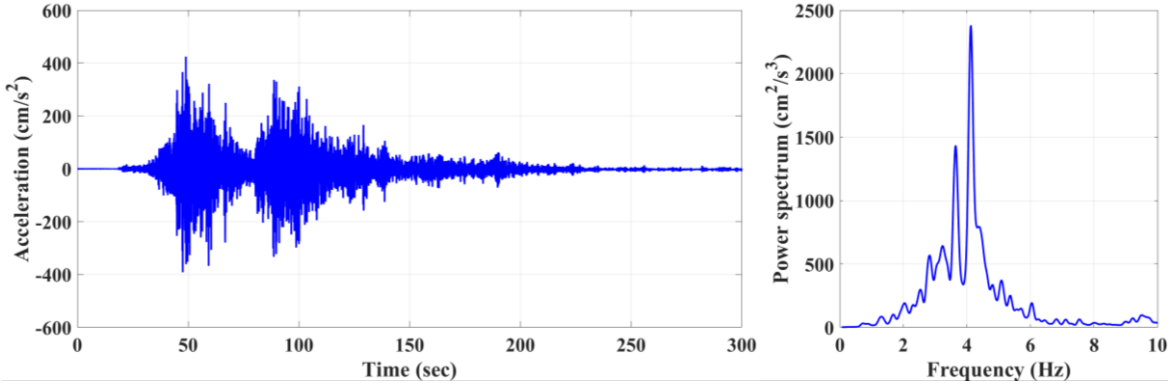

(a) Acceleration time history (b) Power spectrum

Figure 4.14 Ground motion recorded at the MYG001 station

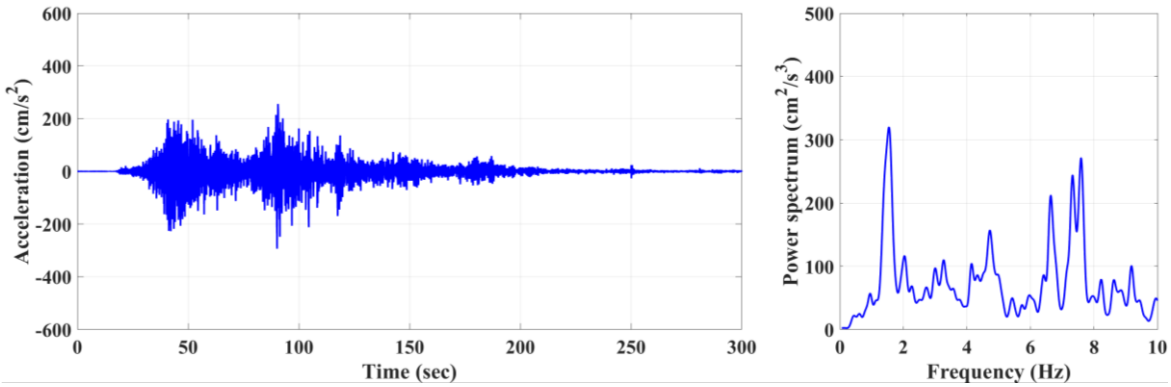

(a) Acceleration time history (b) Power spectrum

Figure 4.15 Ground motion recorded at the MYG018 station

Figures 4.16 and 4.17 show the two different mechanisms for the structure reaching the two limit states for a comparatively small ground motion and a large ground motion. The selected ground motions were prepared by changing the ground motion amplitude of the 2011 Tohoku Earthquake as in Section 4.6.1. When the structure is subjected to the recorded ground motion at the MYG008 station, the ground motion reaches the inter-layer deformation angle before the ground contact ratio as the limit state during the ground motion. Figure 4.16 displays an example of the inter-layer deformation angle at the top of the structure in the time history at three different stages (i.e., 0–300, 300–350, and 350–500 s). The dashed line represents the limit state. The inter-layer deformation angle does not reach the limit state by the ground motion. The first limit state (δ < 0.005) is reached by the following tsunami loading via the hydrodynamic force. Figure 4.16(b) presents the inter-layer deformation angle of the earthquake, which was large enough to reach the limit state.

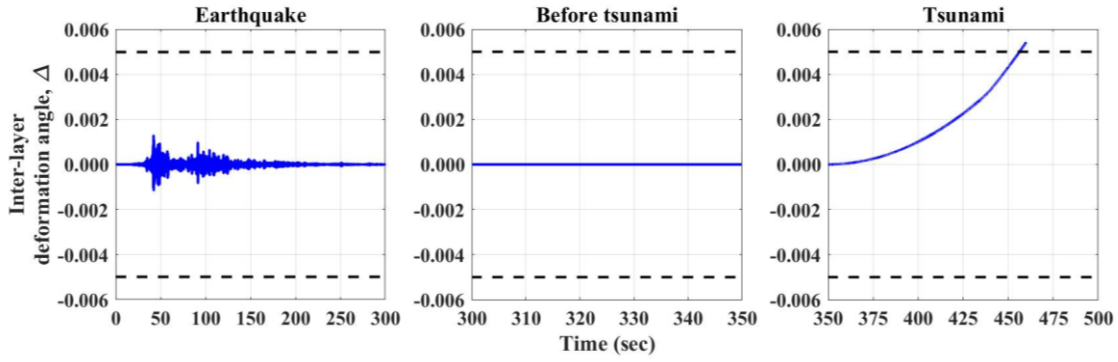

(a) When the tsunami via hydrodynamic reaches the prescribed limit state.

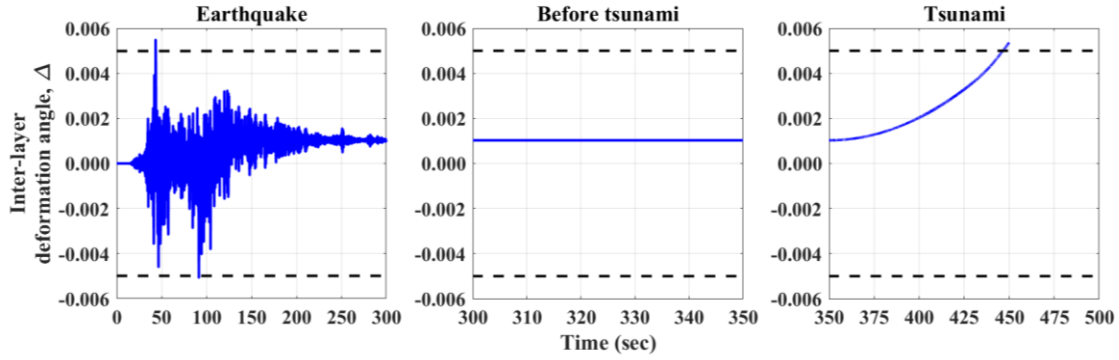

(b) When the earthquake ground motion reaches the prescribed limit state.

Figure 4.16 Inter-layer deformation when the structure is subjected to the recorded ground motion at station MYG008.

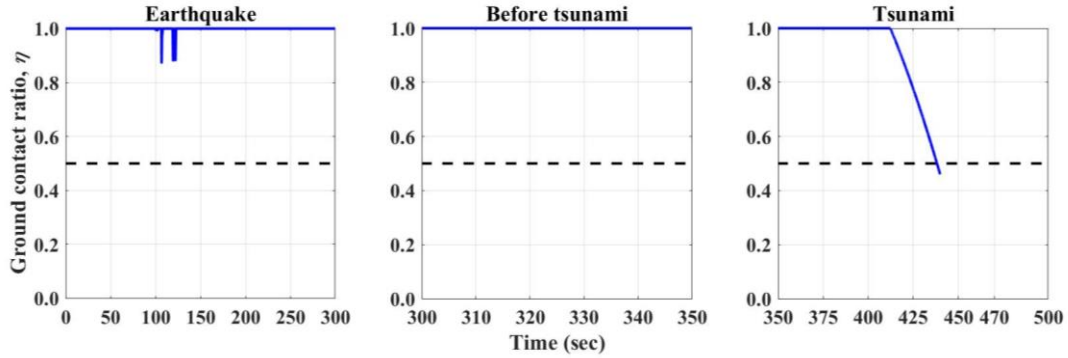

(a) When the tsunami via hydrodynamic reached the prescribed limit state.

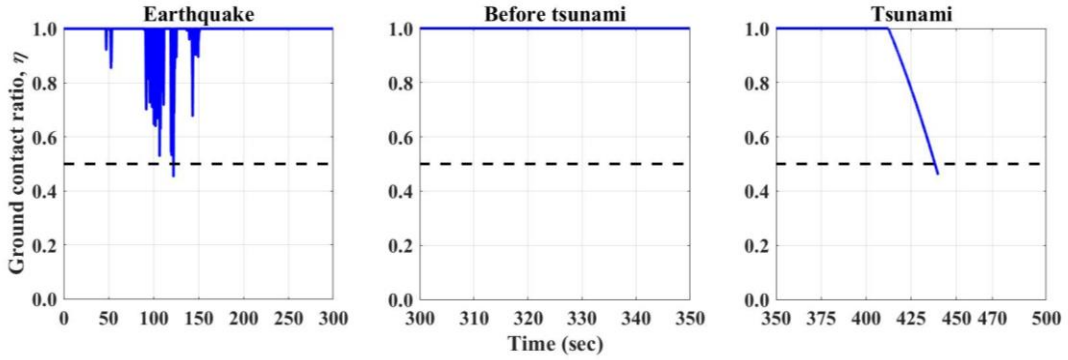

(b) When the earthquake ground motion reached the prescribed limit state.

Figure 4.17 Ground contact ratio when the structure is subjected to the recorded ground motion at the MYG001 station.

In contrast, when the structure is subjected to the recorded ground motion at the MYG001 station, the ground contact ratio reaches the limit state before the inter-layer deformation angle by the ground motion, as presented in Figure 4.17. At a small ground motion intensity, the ground contact ratio is large enough not to reach the limit state during the earthquake, as exemplified in Figure 4.17(a). Figure 4.17(b) illustrates an example case when the ground contact ratio is small enough for reaching the limit state during the earthquake.

Figure 4.18 presents the two resulting earthquake–tsunami interaction diagrams for the two different limit states and the six selected ground motions during the 2011 Tohoku Earthquake. Figure 4.18(a) shows the hydrodynamic force interaction when the earthquake loading reaches the story drift angle before the ground contact ratio. Figure 4.18(b) depicts the hydrodynamic force interaction when the ground contact ratio is reached before the inter-layer deformation angle during the earthquake ground motion. Interestingly, the value of the

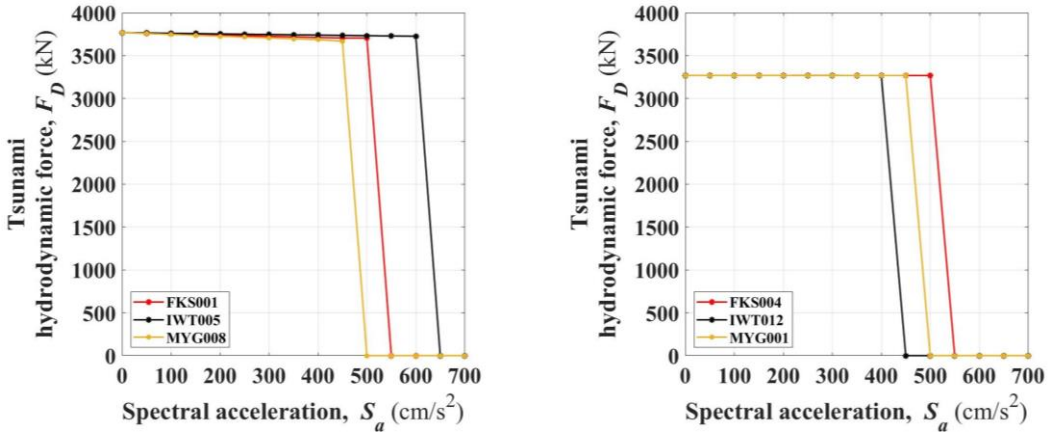

(a) Inter-layer deformation angle (b) Ground contact ratio

Figure 4.18 Earthquake–tsunami interaction diagrams

hydrodynamic tsunami force on the ordinate axis gradually decreases when the ground motion intensity increases on the vertical axis in Figure 4.18(a), while that on the ordinate axis is constant on the vertical axis in Figure 4.18(b). The earthquake–tsunami interaction diagrams will improve the accuracy when a nonlinear behavior occurs, although this section considered only the structural nonlinearity and not the soil nonlinearity because the horizontal–vertical interactive SR model is employed. In Figure 4.18, the structural system becomes close to the resonance state, and the ground motions reach the ground contact ratio as the limit state before the inter-layer deformation angle when the predominant frequency of the six selected ground motions is close to the natural frequency of the first mode of the soil and foundation system (e.g., recorded ground motions at the FKS004, IWT012, and MYG001 stations). In contrast, when the structure is subjected to ground motions (e.g., recorded ground motion at the FKS001, IWT005, and MYG008 stations), the inter-layer deformation angle is reached as the limit state before the ground contact ratio. This indicates two different cases: (1) the structure nonlinearity progresses and reaches the limit state of the structure due to the ground motion increases; and (2) the foundation limit state suddenly comes without structural damage.

4.7 Summary

This chapter extended the earthquake–tsunami interaction diagram proposed by Carey et al. [2] by considering the nonlinear soil–structure interactions with the foundation uplift and simultaneously considered two different limit states of structural damage (i.e., inter-layer drift deformation angle) and foundation uplift (i.e., ground contact ratio) considering that whether or not the building or the foundation reaches the critical state first will depend on the input

ground motion characteristics. A three-story building on a mat foundation sustained on stiff soil was prepared to develop the earthquake–tsunami interaction diagram considering the foundation uplift. Thirty recorded ground motions in the Fukushima, Iwate, and Miyagi prefectures during the 2011 Tohoku Earthquake (EW component) and the hydrodynamic force were applied as the earthquake and tsunami loadings, respectively. Six ground motions with different frequency characteristics from the 30 ground motions were selected to generate the diagrams by simultaneously considering two different limit states. The obtained results are as follows:

1. The structural resistance to the following tsunami is reduced by the residual effects of earthquakes.
2. The resistance remaining after the earthquake differs depending on the different degrees of the foundation uplift during an earthquake.
3. In addition to the hydrodynamic force, buoyancy force, and soil instability, the occurrence of a building overturn may also be caused by earthquakes and their specific characteristics, which can reduce the structural resistance needed to withstand a tsunami.
4. The limit states differ for each case; thus, the input ground motion characteristics will affect the dominant limit states.
5. The diagrams indicate that the damage caused by the ground motion will reduce the intensity of the needed tsunami loading via the hydrodynamic force (F_D) to reach the limit states.
6. Multiple limit states must be considered when preventing complex disasters caused by earthquakes and tsunamis.

Further research is necessary in understanding the complex interactions between earthquakes and tsunamis better and in developing prevention methods for earthquake–tsunami multihazards because some factors (e.g., soil properties, buoyancy, and debris impact forces) must still be taken into account to more accurately improve the earthquake–tsunami interaction diagrams for estimating the remaining strength of structures after earthquakes to withstand subsequent tsunamis.

References

[1] Mimura, N., Yasuhara, K., Kawagoe, S., Yokoki, H. and Kazama, S.: Damage from the great east Japan earthquake and tsunami — a quick report, *Mitigation and Adaptation Strategies for Global Change*, Vol. 16, No. 7, pp. 803-818, 2011.

[2] Carey, T. J., Mason, H. B., Barbosa, A. R. and Scott, M. H.: Multihazard earthquake and tsunami effects on soil-foundation-bridge systems, *Journal of Bridge Enginerring*, Vol. 24, No. 4, 2019.

[3] ASCE: Minimum design loads and associated criteria for buildings and other structures, *ASCE/SEI 7-16*, 2016.

[4] Vamvastsikos, D. and Cornell, C. A.: Incremental dynamic analysis, *Earthquake Engineering and Structure Dynamics*, Vol. 31, No. 3, pp. 491-514, 2002.

[5] ASCE: Minimum design loads and associated criteria for buildings and other structures, *ASCE/SEI 7-10*, 2010.

[6] Construction Publishing Center Co., Ltd.: *Building structural design standards and reference material 2018 Edition*, 2018. (in Japanese)

[7] Honjo, Y., Kikuchi, Y. and Shirato, M.: Development of the design codes grounded on the performance-based design concept in Japan, *Soils and Foundations*, Vol. 50, No. 6, pp. 983-1000, 2010.

[8] Nuclear standard committee of JEA: Technical regulations for seismic design of nuclear power plants, *Japan Electric Association*, JEAC 4601- 2008, pp. 181-186, 2009. (in Japanese)

[9] Kanai, K.: *Seismology in Engineering*, Tokyo University, Japan, 1983.

[10] Varecha V. P., Fadllan A., and Hartono, H.: Soil classification using horizontal to vertical spectrum ratio methods on Scilab in Sendangmulyo, Semarang, *Physics Education Research Journal*, Vol. 4, No. 2, pp. 71-78, 2022.

[11] FEMA: Guidelines for design of structures for vertical evacuation from tsunamis, *FEMA P-646 Third Edition*, 2019.

[12] Yeh, H., Sato, S. and Tajima, Y.: The 11 March 2011 East Japan earthquake and tsunami: tsunami effects on coastal infrastructure and buildings, *Pure and Applied Geophysics*, Vol. 170, No. 6-8, pp. 1019-1031, 2013.

[13] Latcharote, P., Suppasri, A., Yamashita, A., Adriano, B., Koshimura, S., Kai, Y. and Imamura, F.: Possible failure mechanism of buildings overturned during the 2011 Great East Japan Tsunami in the town of Onagawa, *Frontiers in Built Environment. Earthquake Engineering*, Vol. 3, 2017.

[14] Foytong, P., Ruangrasaamee, A., Shoji, G., Hiraki, Y. and Ezura, Y.: Analysis of tsunami

flow velocities during the March 2011 Tohoku, Japan, tsunami, *Earthquake Spectra*, Vol. 29, No. 1, pp. 161-181, 2013.
[15] Fritz, H. M., Phillips, D. A., Okayasu, A., Shimozono, T., Liu, H., Mohammed, F., Skanavis, V., Synolakis, C. E. and Takahashi, T.: The 2011 Japan tsunami current velocity measurements from survivor videos at Kesennuma Bay using LiDAR, *Geophysical Research Letters*, Vol. 39, No. 7, 2012.

5. CONCLUSIONS

According to the literature review, giant tsunamis generated by extremely intensive earthquakes cause numerous structural damages to coastal structures. Therefore, a method for evaluating and describing the effects of earthquake–tsunami multihazards is necessary for preventing coastal area damages. Many studies on earthquake–tsunami multihazard have tackled this problem, but only a few considered the nonlinear soil–structure interaction, especially the foundation uplift, which has significant effects on structural responses. In addition to reports on the structural damage caused by the 2011 Tohoku Earthquake and Tsunami events, the disaster overturned many buildings. This phenomenon must be prevented at all costs because it is directly linked to the loss of human life. This study aimed to further develop the earthquake–tsunami interaction diagram proposed by Carey et al. (2019) by considering the foundation uplift. However, before generating the diagrams, the effect of seismic isolation caused by the foundation uplift on building structures was first discussed to understand the physical foundation uplift behavior. The obtained results are summarized below by separating each chapter.

In Chapter 2, a comparative analysis was conducted on two numerical models considering the foundation uplift, that is, the horizontal–vertical interactive sway-rocking model and the macroelement model, to examine the influence of soil and geometrical nonlinearities on the foundation uplift behavior and structural responses. To achieve this objective, the study focused on low- and medium-rise buildings with shallow foundations and three different soil types. Two ground motion categories were prepared, namely simulating inland and subduction-zone earthquakes. Five ground motions, each with varying frequency characteristics and recorded from significant earthquakes, were selected for the time history analysis. The results presented that the structural responses of both numerical models were similar for the structures sustained on stiff soil and rock, even though the ground contact ratios for both models relatively differed, especially at the ground contact ratio of less than 40%. Furthermore, the plastic soil deformation might reduce the foundation uplift. The comparison results also indicated that the degree of foundation uplift depends on the structure and seismic input motion characteristics and the soil conditions.

In Chapter 3, the effect of the seismic isolation caused by the foundation uplift on the structural behavior was examined by using the energy concept. The analysis focused on both a low-rise building and a five-story building constructed on a mat foundation supported by stiff soil. For a clear discussion of the foundation uplift effect, this chapter compared the

performances of the structures under three different scenarios (i.e., one with a fixed-base foundation, one with a structure with the linear soil–structure interaction, and one with a structure considering the soil–structure interaction with the foundation uplift). The structures were subjected to fifteen distinct ground motions recorded during various earthquake events. The computation results showed that the foundation uplift was beneficial for the structure because the foundation uplift worked in cutting off the seismic motion, thereby resulting in less structural acceleration responses. However, the reduction effect of the foundation uplift will depend on the characteristics of structures and ground input motion. In addition, if the structure is subjected to a high-intensity and low-frequency ground motion, the foundation uplift may negatively affect the structural responses because an excessive foundation uplift may make the structure unstable, which must be avoided.

In Chapter 4, earthquake–tsunami interaction diagrams considering the foundation uplift were generated. This chapter also delved into a simultaneous consideration of two distinct limit states related to structural damage (i.e., inter-layer drift deformation angle) and foundation uplift (i.e., ground contact ratio). This approach was necessary because determining whether or not the building or the foundation reaches a critical state first hinges on the input ground motion characteristics. A three-story building with a mat foundation on stiff soil was prepared to generate the earthquake–tsunami interaction diagram considering the foundation uplift. Subsequently, 30 recorded ground motions from the Fukushima, Iwate, and Miyagi prefectures during the 2011 Tohoku Earthquake were applied as the earthquake loading, with the hydrodynamic force representing the tsunami loading. In addition to generating the diagrams by simultaneously considering the two different limit states, six ground motions with different frequency characteristics were selected. The earthquake–tsunami interaction diagrams illustrated that the damage resulting from the earthquake represented by the ground motion reduces the required tsunami intensity via the hydrodynamic force (F_D) to reach the corresponding limit states. It conclusion, the structural resistance to the following tsunami can be reduced by the remaining effects or damage caused by earthquakes. The diagrams also indicated the dependence of the dominant limit state on the ground input ground motion characteristics. Hence, the earthquake–tsunami interaction diagrams considering multiple limit states are necessary for an effectual multihazard prevention, particularly in complex disasters caused by both earthquakes and tsunamis.

ACKNOWLEDGMENT

I would like to express my sincere gratitude to my supervisor, Prof. Dr. Atsushi Mikami, for his invaluable guidance and support at every stage of the research process. I also sincerely appreciate my sub-supervisor, Prof. Dr. Motohiro Sugiyama, for always providing guidance and support whenever I need them. I have been supported by my supervisor and sub-supervisor since I was a master course student. Their benevolence has been instrumental in both my academic life and personal growth. I thank them deeply for the encouragement they have given me to complete this project.

I am also very grateful to my defense committee, which is composed of Prof. Dr. Yoshitaka Kajita from the Department of Civil Engineering, Prof. Dr. Ken Watanabe from the Department of Architecture, and Prof. Dr. Kenji Yamamoto from the Department of Architecture, for providing valuable comments to enhance this dissertation. I could not have enhanced this work without my defense committee who provided knowledge, expertise, and feedback.

I would like to express my gratitude as well to the Public Works Research Institute, Tsukuba, Japan and ARK Information Systems, Inc. for providing good analysis programs. Credit is also due to the National Research Institute for Earth Science and Disaster Prevention and Disaster Resilience, Midorikawa and Miura from Tokyo Institute of Technology and the Pacific Earthquake Engineering Research Center for their observation of the recorded ground motion data. I am also grateful to Dr. Kashima of the International Institute of Seismology and Earthquake Engineering (BRI) for providing the software View-Wave, which allowed me to calculate the power spectrum.

I wish to show further gratitude to the senior and junior students at Prof. Mikami's laboratory for helping not only with the simulation analysis, but also with many other aspects. Thank you, in particular, to Mr. Soichiro Akiyama and Mr. Kazuma Asanuma for their support with Japanese and for helping me acquire the simulation information.

My gratitude also goes to the other faculty and staff members of my department for their cooperation and assistance.

Finally, last but not the least, I am forever grateful to my family, especially to my parents, and friends for their encouragement and moral and emotional support during this process.